Bergische Universität Wuppertal

Investigation of the Mechanism Causing Baseline Shift in Single Stage Quadrupole Mass Spectrometers

Dissertation

zur Erlangung des akademischen Grades
Doktor der Naturwissenschaften (Dr. rer. nat.)

Vorgelegt von
Markus Langner

Bergische Universität Wuppertal
Fakultät 4 - Mathematik und Naturwissenschaften
Physikalische und Theoretische Chemie unter der
Anleitung von Prof. Dr. Thorsten Benter

September 2023

"You just begin. You do the math. You solve one problem and you solve the next one and then the next. And if you solve enough problems, you get to come home."
Andy Weir, The Martian

"Never accept the world as it appears to be. Dare to see it for what it could be."
Dr. Harold Winston

Für Sascha. Für Papa.

Danksagung

Alleine wäre die Fertigstellung dieser Arbeit zwar möglich, aber nicht so unterhaltsam gewesen. Die Arbeit und generell meine komplette Zeit in der Arbeitsgruppe der Physikalischen und Theoretischen Chemie in Wuppertal war die beste Zeit meines Lebens. Ich hab dort nicht nur Arbeitskollegen sondern Freunde gefunden und ich bin unendlich dankbar für jede einzelne Person dort.

Nichtsdestotrotz möchte ich einige Personen und Gruppen hervorheben.

Zunächst Joshi, der mich in zahllosen Stunden im Labor und im Büro und in Discord nicht nur fachlich sondern auch persönlich unterstützt hat. Ohne ihn wäre die Corona Zeit nicht so spurlos an mir vorbeigegangen und die Zeit im Labor wäre mit Sicherheit nicht so spaßig gewesen, hätte man nicht jeden Fehlversuch und jeden Erfolg direkt teilen können.

Generell die V.70 Ultras, Sanna, Lena und Joshi, waren jederzeit bereit für mehr oder minder thematisch wertvolle (aber nie sinnlose!) Diskussionen. Gleichzeitig konnte man im Büro auch mal die Fresse halten, wenn wirklich gearbeitet werden musste. Mit euch war es nie nur ein Job im Büro zu sitzen und ich hab euch tatsächlich vermisst, wenn ich eine Zeit lang nicht in der Uni war.

Der Rest des Zeiss Teams (der Teil, der mich noch durch die Dissertation begleitet hat (die neuen sind aber nicht weniger geil!)). Ich kann nicht oft genug betonen, wie unverschämt viel Glück wir mit dieser Gruppe hatten. All die Dienstreisen, all die meetings, all die Diskussionen und Konferenzen und es ist einfach statistisch unmöglich, dass es während der gesamten Zeit nicht ein mal zu Stress kam. Ihr seid einfach der Hammer!

Ganz besonderer Dank gilt Hendrik und Thorsten. Es ist nicht selbstverständlich Chefs wie euch zu haben. Eure Motivation für die Arbeit spiegelt sich in der kompletten Arbeitsgruppe wieder und ihr seht einfach selbst nicht, wie groß euer Verdienst an dem Konzept der PTC ist. Ich verdanke euch nicht nur die Promotionsstelle an sich sondern auch, dass ihr mir eine SHK Stelle angeboten habt und ich dadurch schon integriert wurde. Ihr werdet sagen, dass das nicht so ist, aber ich wäre nicht der, der ich jetzt bin, wärt ihr nicht die, die ihr seid. Danke für die Begleitung während meiner Dissertation, für die gute

Zeit auf Parties, im Labor, in Meetings, auf Konferenzen und einfach so im Café Brockmann.

Jedes einzelne Mitglied der PTC ist einfach geil drauf und die komplette Arbeitsgruppe ist etwas ganz besonderes, was mir auf buchstäblich jeder Konferenz bestätigt wurde. Die Stimmung ist unvergleichbar und ich wünsche mir den Rest meines Lebens Kollegen, die auch nur 20% so cool sind wie dieser geile Haufen hier!

Erklärung

"Ich versichere, die Arbeit selbständig verfasst zu haben, nur die in der Dissertation angegebenen Hilfsmittel benutzt und alle wörtlich oder inhaltlich übernommenen Stellen als solche gekennzeichnet zu haben, und dass die Dissertation in der gegenwärtigen oder einer anderen Fassung noch keiner anderen Fakultät, keiner Gesamthochschule und keiner anderen wissenschaftlichen Hochschule vorgelegen hat"

Abstract

In this work the processes causing a severe uplift (termed "shift" in the remainder of the thesis) of the baseline, observed in a single stage quadrupole device (Inficon QMG 422) at elevated ion source pressures, are investigated. This shift covers three orders of magnitude relative to the electronic noise baseline and significantly reduces sensitivity and limit of detection of the QMF. Proposed hypotheses causing this effect include:

- Ions breaking through the quadrupole
- Pre-amplifier electronics behaviour
- Photons (UV - VUV)
- Excited species, such as metastable neutrals
- Secondary ions generated outside the ion source

Ion breakthrough involves unfiltered ions reaching the end of the rod region despite being theoretically unstable. This could be caused by space charge effects owing to the elevated ion source pressure. This hypothesis was proven to be wrong upon blocking ions within the ion source by applying high potential walls, without any effect on the baseline. It was investigated if the *pre-amplifier* adapted the baseline to keep both the highest peak and the baseline within its dynamic range. However the baseline is affected immediately after turning on the filament before the pre-amplifier received data on the intensity of the highest peak and the baseline is elevated even if the mass spectrum is devoid of any signal. *Photons* of sufficient energy, produced by recombination reactions within the ion source, emitted by the hot filament or via bremsstrahlung as a result of filtered ions impinging on metal walls, can lead to the photoelectric effect on the detector surfaces. The filament itself does not emit any photons of sufficient energy and bremsstrahlung was ruled out in experiments varying the potential on the rods of the QMF. Without the specified high voltage on the rods the bremsstrahlung is not present but the baseline is not affected. Recombination reactions and photons produced as a byproduct seem improbable due to their low number and unlikely trajectory terminating at the conversion dynode of the secondary electron multipler (SEM). Additional photons with wavelengths >104 nm were disproven to have an effect by experiments with an LiF window in front of the SEM, which reduced the baseline to the electric noise. Calculations involving

the ionization cross section and the excitation cross section of argon showed that *excited species* are produced in the ionization source to a degree of one in every 28000th neutral particle. Estimating the flow through the entrance plate of the employed SPM ion source as well as DSMC simulations demonstrated the presence of sufficient excited species traversing the QMF to cause the baseline shift. However the excited species must exhibit lifetimes of several ms so only metastable atoms and molecules can intiate reactions downstream of the mass analyzer. The excited species themselves cannot be the main source for the baseline shift as it was established that potentials applied to the deflection plate, an electrode designed to deflect ions away from the analyzer region onto the conversion dynode, had a significant effect on the level of the baseline. This led to the proposal of *secondary ions* produced inside of the deflection unit to be the cause for the uplift of the baseline. Three possible mechanisms for secondary ion production were thus investigated:

- Photoionization
- Gas phase reactions
- Resonant ionization

Both photoionization and gas phase reactions were proven to be highly unlikely due to low pressure within the deflection unit (1×10^{-4} mbar) and the linked low collision rate. Additionally the probability for photons to penetrate into this area was simulated to be 4.5×10^{-4} % and the total amount of photons is rather low to begin with. A gas phase reaction can only lead to an ion if both particles are already in an excited state while the calculated most probable number of collisions a metastable particle experiences in the relevant geometry is 8.5×10^{-8}. These arguments alone leave resonant ionization as a realistic mechanism. It was hypothesized that the mere interaction between an excited atom or molecule and a given surface can lead to an ionizing reaction if the work function of the surface is larger than the effective ionization energy of the excited particle. A combination of Molflow and SIMION simulations as well as experiments involving the variation of applied potentials inside of the deflection unit and generated ions in this geometry are in excellent agreement, which is taken as strong evidence that this mechanism is indeed the root cause for the baseline shift.

The behavior of the baseline when using the faraday cup upon changing the deflection potential shows a plateau at deflection voltages >75 V and a steep decline at lower potentials. The simulations were utilized to reproduce ion trajectories to show that this behavior is expected due to the exact locations of the ionization, which were achieved by Molflow simulations. The result of these simulations in addition to experimental data, the mechanism of

Auger neutralization, Auger deexcitation and resonant ionization were used to determine that excited species as well as secondary ions are the cause for the baseline shift when using the faraday cup.

The SEM exhibits the largest baseline shift at low deflection potentials which was also the result of SIMION simulations. The trajectories of ions are significantly affected by the deflection plate, owing to its close proximity to the location of the ionization, which in turn reduces the amount of collected ions at the conversion dynode when high potentials are applied. The experimental and simulated data are in good agreement. It is thus concluded that the baseline shift is caused by secondary ions produced in a resonant ionization mechanism. However the comparison also indicates a secondary source for the shift of lower significance compared to secondary ions. This secondary source was deducted to either be direct interaction of excited species with the conversion dynode or photons with a wavelength smaller than 104 nm.

Contents

List of Figures

Abbreviations

∇	Nabla operator
α'	Integration constant in the Mathieu equation
α"	Integration constant in the Mathieu equation
β	Parameter in the Mathieu equation characterizing the nature of ion motion
ϵ_0	Vacuum Permittivity
η	Weighting factor describing the y dimensional component
γ	Weighting factor describing the z dimensional component
λ	Weighting factor describing the x dimensional component
μ	Parameter in the Mathieu equation characterizing the nature of ion motion
μ_e	Reduced mass of an electron
ω_0	Fundamental frequency of the ion motion
ω_n	Higher frequencies of ion motion
ϕ	Applied potential
τ_n	Periodicity of the ion frequency
ξ	Time expressed as $\frac{\omega t}{2}$
a	Parameter in the Mathieu equation representing the direct component of applied potential
AC	Alternate Current
AD	Auger Deexcitation
AN	Auger Neutralization
C_2n	Constant in the solution of the Mathieu equation
CID	Collision-Induced Dissociation
DC	Direct Current
E_I	Ionization Energy
E^*	Energy of an excited state
E_0	Position independent field strength
E_x	Field strength in the x dimension
E_y	Field strength in the y dimension
E_z	Field strength in the axial dimension
E_{bind}	Binding energy of electrons
$E_{electron}$	Energy state of a bound electron
E_{kin}	Kinetic energy
e	Electronic charge
EI	Electron ionization

f	Applied frequency in Hertz
h	Planck constant
IC	Internal conversion
ISC	Intersystem crossing
KE	Kinetic emission
L	Length of the rod system
LOD	Limit of detection
m	Mass
m_e	Mass of an electron
n	Principal quantum number
PE	Potential emission
q	Parameter in the Mathieu equation representing the alternating component of applied potential
Q_1	First QMF in a triple stage quadrupole instrument
Q_2	Second QMF in a triple stage quadrupole instrument
Q_3	Third QMF in a triple stage quadrupole instrument
QIT	Quadrupole Ion Trap
QMF	Quadrupole Mass Filter
r	Rod radius
r_0	Half distance between opposite rods
RGA	Residual Gas Analyzer
RI	Resonant Ionization
SEM	Secondary Electron Multiplier
SPARTA	Stochastic Parallel Rarefied-gas Time-accurate Analyzer
SPM	Sputter Process Monitor
t	Time
TPMC	Test Particle Monte Carlo
TSQ	Triple-Stage Quadrupole
U	Direct current
V	Alternating current
VHS	Variable Hard Sphere
VSS	Variable Soft Sphere
W	Work function
$\ddot{x}$	x dimensional displacement doubly differentiated according to the time
x	x dimensional displacement differentiated according to the time
$\ddot{y}$	y dimensional displacement doubly differentiated according to the time
y	y dimensional displacement differentiated according to the time
$\ddot{z}$	z dimensional displacement doubly differentiated according to the time

z Charge

1 Introduction

1.1 Short History of Quadrupole Mass Analyzers

1.1.1 The Beginning of Quadrupole Mass Filters

The history of the electrical quadrupole mass analyzers began in 1953 with the publication of Paul and Steinwedel, in which they describe a new mass spectrometer without the need for a magnet [1]. Hitherto, periodic magnetic quadrupolar fields had been used to focus protons in high-energy accelerators [2] but a prominent advantage of the electrical field is that it can be modified rather swiftly compared to magnetic fields. The first quadrupole mass filter (QMF) was assembled by Paul along with his colleagues at the university of Bonn and Paul was awarded the Nobel prize in Physics 1989 along with Norman Ramsay and Hans Gehmelt for their pioneering work [3] in the field. In the patent for the QMF, the three dimensional quadrupole ion trap is mentioned almost like a byproduct as "still another electrode arrangement".

The original patented QMF design consisted of four round metal rods in a square configuration. An RF potential is applied to these rods, with opposite rods being connected, while the different rod pairs can be additionally DC biased. As a convention the two rods in the x-direction are positively biased and the rods in the y-direction are negatively biased, the z-axis being the axis the ions travel along the quadrupolar field[3]. In absence of any DC potential, the QMF is in RF-only mode and acts as a high-pass filter, allowing all ions above a certain threshold in m/z to be transmitted from one pressure regime to another. This configuration is widely used as an ion guide or to filter out carrier gas with low m/z rather than a mass analyzer. It is worth mentioning that, mathematically, the metal rods should be hyperbolic to yield the most optimal quadrupolar field between the rods but the vast majority of QMF use round

rods due to lower constructive effort. An almost optimal quadrupolar field can be achieved with round rods, given the ratio of r, the radius of the rods, to r_0, the half distance between opposing rods, is at a very specific number[4]. A more in-depth analysis on the mathematics and the general principle of operation is found in chapter 1.2.1.1.

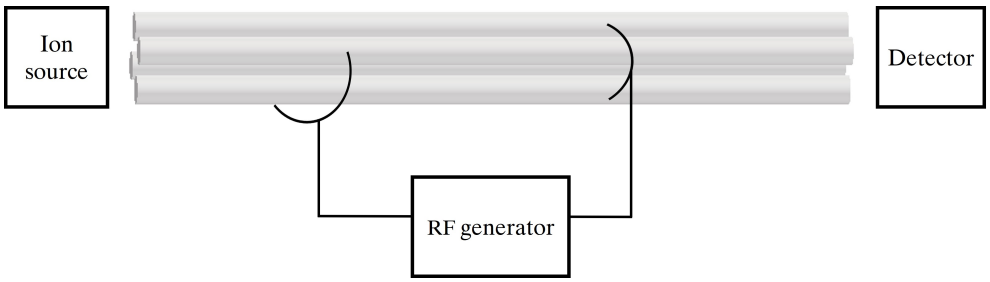

Figure 1.1: Depiction of the basic components of a QMF consisting of an ion source, an RF generator, a detector and the aforementioned rod system.

1.1.2 The introduction of pre- & post-filters

Commercial QMF were available in the early 1960s as residual gas analyzers (RGA) equipped with a faraday cup detector[3]. These early QMF experience trouble analyzing ions in the high m/z range which was attributed to fringe fields in the area between the ion source and the rod system and also between the rod system and the detector. As the ions are ejected from the ion source at constant kinetic energy heavier ions have a lower velocity compared to lighter ions, which translates to larger dwell times spent within the fringe fields and thus more of the heavy ions are lost due to the effects of fringing fields effects. This issue was resolved by installing a pre-filter consisting of an auxiliary rod system in the RF-only mode[5], a design later known as a Brubaker f. Later on it was found that the same filter should be installed as a post-filter downstream of the rod system as well to reduce the effects of fringe fields in that area of the device. In fact the DC part of the potential does not have to be eliminated entirely but it is possible to achieve the same outcome when the AC and DC components are reduced towards both ends of the analyzer in a stepwise ramp[6]. Both of

these proposals reduce the fringe fields at analyzer entrance and exit while at the same time leading to a more focused ion beam exiting the rod system, with regard to the x- and y-axes.
An alternative construction to achieve the elimination of the fringe fields is the "ELFS" technique[7] (Extranuclear Laboratories Field Seperation). A dielectric tube with semiconductive or high-resistive coating is installed directly in front of the rod system, which essentially shields the DC components of the fringe fields and their effect on the ion trajectories (figure 1.2). This serves as a much easier and more subtle solution compared to the aforementioned filter technique. Pre- & post-filters are standard nowadays for Quadrupole Mass Filters.

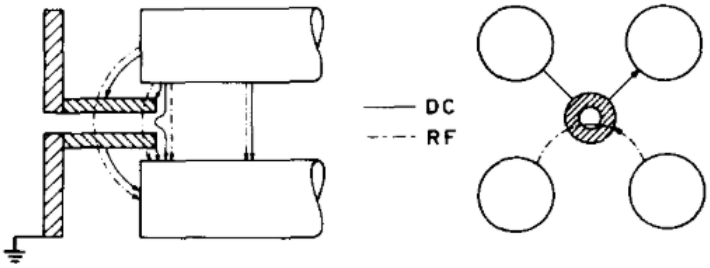

Figure 1.2: Illustration of the ELFS technique. The tube is visible on the left and the fringe fields are depicted as a solid and a dashed line[7].

1.1.3 First applications of Resonant Excitation

Ions travel through the metal rod system along the z-axis in a spiral-like manner from the ion source towards the detector. Ions with a stable trajectory, i.e. those with the desired m/z-ratio, traverse the entire length of the system while unstable ions are filtered out eventually. The frequency of the ion motion is thus dictated by the m/z-ratio, which in turn suggests that singular m/z-ratios can be resonantly excited by superimposing a second alternating current onto the existing DC and RF potentials already present. If the frequency of the auxiliary potential is carefully adjusted to match the fundamental frequency of the spiral motion of the undesired ion species, the amplitude of the motion increases progressively and the ion can be systematically filtered out without significantly influencing trajectories of other m/z values, since they are not in resonance with the auxiliary AC potential. Notably, this AC potential does not have to be quadrupolar

in nature but can be homogeneous to destabilize the ion in one dimension but the increase of the amplitude is less steep as compared to conventionally unstable ions which conveys that ions need to remain longer in the notch filter to be filtered out quantitatively.
This third mode of operation for QMF, the so-called notch mode, was presented in the original work from Paul and Zahn as a means for isotope enrichment studies involving Sodium and Rubidium[8]. The original setup was later enhanced by adding a second rod system that exclusively acts as the notch filter upstream of the conventional rod system[9]. Experiments with this setup indicated that the mass spectra taken were devoid of the undesired m/z-ratios while being unchanged in for other m/z values. It has to be noted though that the resonant excitation of specific m/z ratios does reduce the transmission of ions close to the undesired ion with regards to their m/z as well. Depending on the amount of ions to be excited a large fraction of the mass spectrum suffers in terms of intensity.

1.1.4 Tandem Mass Spectrometry involving several QMF

Later on a rather prominent use for quadrupole mass analyzers opened up, when several QMF were linked together in MS/MS (or MS^x) experiments. Specifically, in the majority of such systems, three QMF were used in succession, the first (Q1) and third (Q3) running in normal QMF mode and the second (Q2) in RF-only mode to perform as one triple-stage quadrupole (TSQ). The second rod system is mainly used for collision-induced dissociation (CID) of the ions that traversed the first filter. This way a sample can be reduced to one single m/z in the Q1 which can be dissociated in the second QMF. The produced fragment ions can ultimately be analyzed in the Q3 to generate a mass spectrum and allow for structural identification regarding the parent ion. The first instrument of that kind was employed in experiments for the determination of the photodissociation cross-sections of CH_3^+ and CBr_3^+[10] and only four years later it was found, that the same instrument could be utilized to generate fragment ions of desired discrete m/z ratios[11, 12].
The dissociation is achieved by adding a collision gas into the chamber of the Q2, raising the pressure and thus the amount of collisions among neutral gas particles and analyte ions. The exact parameters that influence collision rates, con-

tainment of parent and fragment ions and other aspects of the Q2 were examined theoretically and experimentally three years later[13]. Notably, the instrument used for these experiments was already equipped with pre- and post-filters but without apertures between the three QMF. The four points the authors addressed as key aspects of quantitative containment and transfer or parent/fragment ions were:

- The dependance of parent ion stability on q
- Susceptibility to loss of ions by gas scattering
- Loss of ions due to sudden changes in m
- Average path length of parent ions in the Q2

The authors concluded that triple quadrupole devices should additionally be equipped with ion apertures between the seperated QMF with an aperture size of $1.4\,r_0$. Furthermore it was recommended to apply *constant q daughter* operating mode, which means keeping the RF amplitude of the Q2 and the Q3 at a constant ratio throughout a scan. On a final note the Q3 should be operated at a constant AC/DC ratio to avoid m/z discrimination against higher mass ions.
In addition to the TSQ, QMF are well suited for coupling with other mass filters, such as magnetic (B) and electric (E) sectors. The various combinations were examined and evaluated in the literature[14]. The design of different combinations, such as a BEQQ instrument further advanced the knowledge of quadrupole mass filters.

1.1.5 Frequency Scanning

Conventionally, QMF operate with a fixed frequency and scan the amplitude of the AC and DC components to generate a mass spectrum. However it is possible to keep the AC and DC potentials fixed and sweep the frequency to yield the same result. This principle of operation has three distinct advantages[15]:

- Only one parameter is changed which results in smaller drifts
- The mass range can be extended without the need for extensive RF potentials

- The resolution is constant because the location in the stability diagram is fixed

It was stated that the resolution achieved with a QMF using said mode of operation is comparable to conventional devices[16]. Even though these advantages sound promising, different problems arise. First and foremost the electronics needed to precisely adjust the frequency of the applied potential to the rods is much more complex compared to those needed for a conventional QMF, which also equates to higher manufacturing cost. The attainable resolution is directly linked to the maximum RF potential, which puts even more demand on a high quality RF generator, when high resolution is desired.
Despite the advantages the frequency scanning never found its way into a commercial product and remained theoretical and experimental.

1.2 Components of a Mass Spectrometer

Mass spectrometers more or less consist of the same components independent of their specific use and nature. These components are: An inlet system, an ionization source, a mass analyzer and a detector system. Out of the myriad of possible combinations a subset is discussed more in detail in the following, namely the quadrupole mass analyzer, electron ionization and two detector systems: The faraday cup and the SEM.

1.2.1 The Mass Analyzer

The mass analyzer is located between the ionization source and the detector and is employed to separate previously formed ions with regard to their specific m/z value. There are several possible methods to achieve mass separation; in this work only the quadrupole mass analyzer is examined in detail.

1.2.1.1 Principle of operation of Quadrupoles

1.2.1.1.1 The applied potential The mechanical simplicity of a quadrupole mass analyzer stands in a strong contrast to the complexity of the theory behind the device. In principle, the mass analyzer filters ions of different m/z by applying DC superimposed RF potentials to metal rods which generates a quadrupolar electric field between the rods. This electric field allows the traversal through

the device on stable trajectories solely for ions of a specific m/z ratio while ions on other m/z ratios are filtered out. The quadrupolar field can be described with equation (1.1).

$$E = E_0(\lambda x + \eta y + \gamma z) \tag{1.1}$$

Where E_0 is a position independent factor and λ, η and γ are constant weighting factors for the displacement along the three Cartesian coordinates x, y and z. It is noteworthy, that the electric field is not coupled along the three axes, so it is possible to express them separately, which poses a significant simplification in further mathematical treatments. The electric force, imposed on an ion with charge e is described as eE and its absolute magnitude increases with its displacement from zero, at the center of the rod system.

Assuming no space charge within the quadrupolar field, the potential ϕ a charged particle experiences in the electric field has to fulfill Laplace's equation

$$\Delta\phi = 0 \tag{1.2}$$

Along with the correlation given in equation (1.3) it is apparent, that, to fulfill Laplace's equation, equation (1.4) has to be true as well.

$$E = -\nabla\phi \tag{1.3}$$

$$\lambda + \eta + \gamma = 0 \tag{1.4}$$

There are two special solutions of specific interest to satisfy equation (1.4)[1], which are

$$\lambda = -\eta; \quad \gamma = 0 \tag{1.5}$$

$$\lambda = \eta; \quad \gamma = -2\eta \tag{1.6}$$

The potential of the quadrupolar field on a charged particle is calculated, using equation(1.3) and equation(1.1). ϕ_B represents the possiblity to set a bias DC

[1]There are several more solutions to solve this equation but these two are o practical importance

component on the quadrupole rods in order to control the kinetic energy of the ions inside of the rod region. For the sake of simplicity it will be ignored in the rest of the work however.

$$\phi = -\frac{1}{2}E_0(\lambda x^2 + \eta y^2 + \gamma z^2) + \phi_B \tag{1.7}$$

Combining equations (1.5) and (1.7) the first solution for a possible electric field that fulfills Laplace's equation and has practical use is found.

$$\phi = -\frac{1}{2}E_0\lambda(x^2 - y^2) \tag{1.8}$$

It is apparent, that the function describes a paraboloid as illustrated in figure 1.3 for the x-y-plane while being infinitively extended in z-direction ($\gamma = 0$).

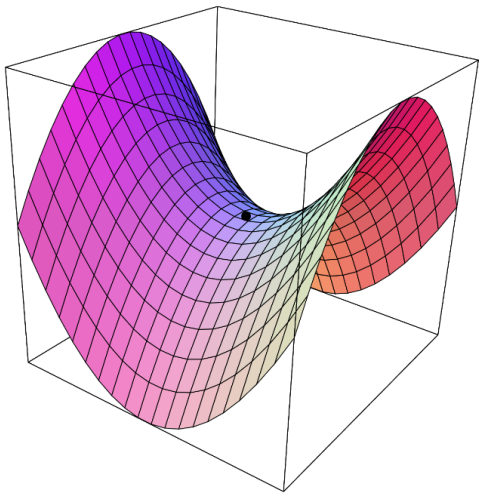

Figure 1.3: Graphical visualization of the equipotential lines as taken from the solution (see (1.5)) for the Laplace equation plotted over the x-y-plane. The shown lines display constant x and y values respectively on the potential surface.

The electrode arrangement needed to generate this potential is displayed in figure 1.4. The electrodes need to form equipotential surfaces of the intended field. According to equation (1.8) this requires $x^2 - y^2$ to be constant which defines the hyperbolic surfaces (equivalent of $x^2 + y^2$ being constant defines a cylindrical tube)

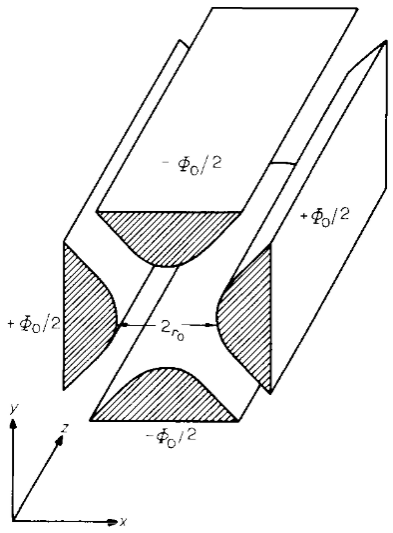

Figure 1.4: Electrode arrangement to generate the quadrupolar potential [4].

Considering the second possible solution, given in (1.6), the potential is calculated as

$$\phi = -\frac{1}{2}E_0\lambda(x^2 + y^2 - 2z^2) \tag{1.9}$$

Without futher analysis here, this is the solution that leads to the 3D quadrupole ion trap.

At this point the potential surface is described mathematically. Also the electrode arrangement needed to employ the aforementioned potential and thus construct a QMF are described. Equations (1.10), (1.11) and (1.12) correlate the acceleration of ions in the quadrupolar field in each given direction with the components of the electric field strength.

$$m \cdot \ddot{x} = e \cdot E_x \tag{1.10}$$

$$m \cdot \ddot{y} = e \cdot E_y \tag{1.11}$$

$$m \cdot \ddot{z} = 0 \tag{1.12}$$

Note that the acceleration along the z-axis is zero, hence the quadrupolar field does not accelerate ions axially through the rod system. The velocity of ions in that direction entirely stems from the ion source region, e.g., the difference of the potentials applied to a pusher and/or extractor electrode to the average

DC potential of the quadrupole rod system. At this point it is necessary to assign specific values to the weighting factors λ and η. The electrodes form equipotential surfaces of the desired electric field. To fulfill equation (1.8) at the apex of the electrodes (where it is x = 0 and y = r0 or y = 0 and x = r0 respectively) with potentials ϕ_0 and $-\phi_0$ applied to the electrodes respectivly, it is reasonable to choose the weighting factors lambda and eta as [4]

$$\lambda = -\frac{1}{r_0^2} \tag{1.13}$$

$$\eta = \frac{1}{r_0^2} \tag{1.14}$$

Combining equations (1.3) and (1.8) with (1.10) and (1.11) while applying (1.13) and (1.14) the general equations of motion along the x- and y-directions are obtained with equations (1.15) and (1.16). For a potential ϕ_0 being constant with respect to the time the negative sign in equation (1.15) implies that a displacement in the x direction results in an acceleration in the opposite direction and thus effectively focusing the ion onto the center of the rod system, causing an oscillation. Accordingly the positive sign in equation (1.16) implies that ions that are not perfectly located on the z-axis experience an ever increasing acceleration away from the center, resulting in a exponential defocusing. On the other hand, if ϕ_0 is described by a periodic function of time, every ion was constantly changing acceleration towards and away from the z-axis (axial center line of the quadrupole). The response of the ions depend on the strength of the field, its frequency and on the inertia of the ions. Provided the periodicity of the potential is short enough to ensure ions are not lost on contact with the metal rods during their defocusing phase and long enough so that ions can follow along despite their inertia, the ions can be focused and transferred to the detector successfully.

$$\ddot{x} = -\frac{e}{mr_0^2}\ \phi_0\ x \tag{1.15}$$

$$\ddot{y} = \frac{e}{mr_0^2}\ \phi_0\ y \tag{1.16}$$

Contrary, for higher amplitude of the applied alternating potential or for lighter ions with smaller m/z value (mass to charge ratio) the secular frequency of the ion is higher. For very light ions, for which the secular frequency comes close to half of the frequency of the applied alternating potential, the

trajectories become more complex and the above mentioned assumption of the micro-motion does not hold true anymore since the ions pick up significantly energy from the driving field. For an ion with a secular frequency of half of the driving frequency, a parametric resonance with the driving field occures, which ejectes the ions very rapidly. For ions which would have an even higher secular frequency, the oscillation amplitude increases exponentially, ejecting the ions out of the transfer region. Therefore no ions with smaller m/z value than the m/z value resulting in a secular frequency of half of the driving frequency are transmitted through the quadrupole device. This m/z value is called low-mass cutoff. With respect to this low-mass cutoff the device operates as a high-pass filter with respect to the m/z value.

Theoretically all ions with larger m/z-value are focussed and transmitted through the quadrupole device. However, very heavy ions (with large m/z value) experience only a very soft focussing force from the alternating field, as mentioned above. It therefore takes many cycles of the alternating field to bend the trajectories of ions with a large m/z towards the center of the device. The amplitude of their trajectories can therefore be large and they can be lost by a collision with the electrodes, even though following a theoretically stable trajectory. Furthermore those ions are very sensitive to all kinds of disturbances, which can cause their loss. Therefore practically the transfer of very large ions is poor, but there is no sharp edge on the high-mass side, as it is on the low-mass side.

Finally the application of a periodic alternating potential superimposed by a constant potential is considered. In this case, ions are constantly defocused in the y direction as described previously. This defocusing force competes with the on average focusing impact of the alternating field. Lighter ions, which follow the alternating component more easily and therefore see a stronger focusing effect, still stay focused and stay on a stable trajectory, while heavy ions cannot withstand the defocusing effect of the constant field and are filtered out in y-direction. The y direction represents a low-pass filter; heavy ions are filtered out in this direction.
The x direction acts as a high-pass filter, as decribed previously. Heavy ions are in total focused towards the z-axis, but light ions are filtered out because they

follow along the alternating component more promptly.

The most common realization for ϕ_0 as a potential consisting of an alternating and a constant component is described by the expression $U - V \cdot \cos(\omega t)$, U being the direct component, V the alternating component, t the time and ω the angular frequency. It is possible and it has also been used to employ a rectangular function instead of a sinusoidal one but the aforementioned function is the vastly more common one.

1.2.1.1.2 The equations of motion and the stability diagram The variable ϕ_0 can now be replaced with the sinusoidal potential to receive more authentic equations of motion

$$\ddot{x} = -\frac{e}{mr_0^2}(U - V \cdot cos(\omega t))x \tag{1.17}$$

$$\ddot{y} = \frac{e}{mr_0^2}(U - V \cdot cos(\omega t))y \tag{1.18}$$

When the time t is expressed as ξ where $\xi = \frac{\omega t}{2}$, the equations of motion can be written as

$$\frac{\partial^2 x}{\partial \xi^2} = -\frac{4e}{m\omega^2 r_0^2} \cdot (U - V \cdot cos(2\xi))x \tag{1.19}$$

$$\frac{\partial^2 y}{\partial \xi^2} = \frac{4e}{m\omega^2 r_0^2} \cdot (U - V \cdot cos(2\xi))y \tag{1.20}$$

In order to achieve the goal of one equation for both xz- and yz-planes it is necessary to define

$$a_u = a_x = -a_y = \frac{4eU}{m\omega^2 r_0^2} \tag{1.21}$$

$$q_u = q_x = -q_y = \frac{2eV}{m\omega^2 r_0^2} \tag{1.22}$$

Which then leads to the equation, in which u represents either x or y

$$\frac{\partial^2 u}{\partial \xi^2} + (a_u - 2q_u \cdot cos(2\xi))u = 0 \tag{1.23}$$

Equation (1.23) now is in the same form as the Mathieu equation[17] in its canonical form (see equation (1.24)). The Mathieu equation in itself is a special case of the Hill equation (see equation (1.25)).

$$y'' + (\lambda + \gamma \cdot cos(x))y(x) = 0 \tag{1.24}$$

$$y''(x) + q(x)y(x) = 0 \tag{1.25}$$

Without further mathematical treatment, the solutions for the Mathieu equation, the general solution in the area of interest, can be expressed as[18]

$$u = \alpha' e^{\mu\xi} \sum_{n=-\infty}^{\infty} C_{2n} e^{2in\xi} + \alpha'' e^{-\mu\xi} \sum_{n=-\infty}^{\infty} C_{2n} e^{-2in\xi} \tag{1.26}$$

α' and α'' being integration constants depending on initial conditions while C_{2n} and μ do not depend on the initial conditions but rather on the values for a and q. Consequently, the character of the ion motion does not depend on the initial conditions, as neither α' nor α'' appear in the periodic term of the equation. The only influence on the character of the ion motion is μ or, in other terms, a and q. So the initial RF phase the ions experience as they approach the QMF does not influence the nature of the trajectory in any way, even though it does affect for example the amplitude of the oscillation.
Now it is possible to categorize the solutions further into realistically useful ones in this case and not useful ones depending on the value for μ as $\xi \to \infty$. u either progressively increases further and further as $\xi \to \infty$ or u remains finite even in the extreme cases. The latter case represents solutions which relate to ions being transmitted through a QMF, the former to ions being excluded by the QMF. Moreover the influence of μ can be described as one of four cases:

- μ is real and non-zero.
- μ is a complex number.
- $\mu = i\beta$ is imaginary and β is not a whole number. This case displays the periodic stable solutions.
- $\mu = im$ is imaginary and m is an integer. This solution is periodic but unstable.

According to these possibilities the parameters a and q, which are the variables to determine the characteristics of the ion motion, can be displayed in a diagram, visualizing stable and unstable regions. Figure 1.5 shows the stability diagram, representing the x-axis. The shaded areas display stable regions in the x direction while the ion trajectory is unstable in the non-shaded areas. Only the first three stable regions are shown and also the limits of the stable regions are labeled as a_m for the even solutions and b_m for the odd ones. The importance of the stability diagram cannot be overstated: With this diagram it is possible to determine if a given ion will have a stable trajectory through the QMF or not. The values for a and q represent the alternating and direct components of the applied potential which means that the exact values for these components can also be evaluated directly from the stability diagram. The stability diagram does not take into account the finite dimension of a QMF. As a result mathematically unstable ions may end up being transmitted through a QMF instrument due to its finite length and mathematically stable ions might be lost, because they hit the electrodes before their trajectory is bent back towards the center.

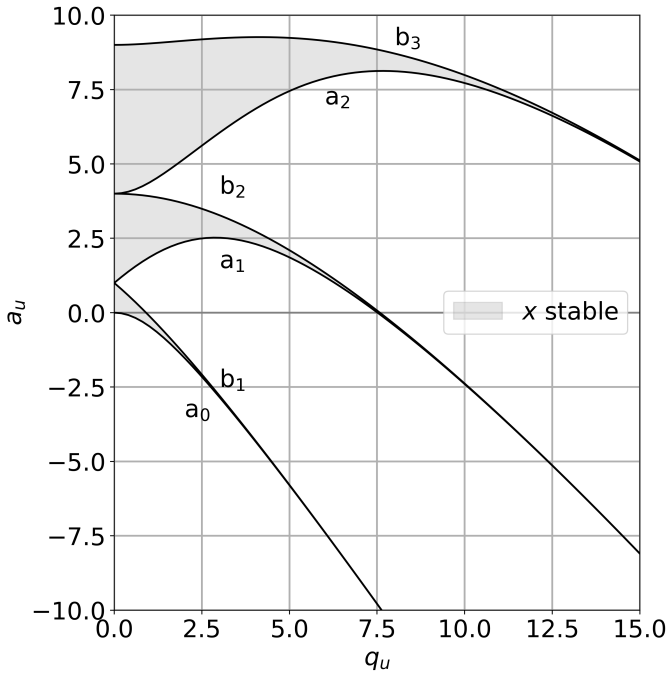

Figure 1.5: The 1D stability diagram. The shaded areas show a-q values for stable motion in the x dimension

It is evident from the equations of motion, that the stable regions are symmetrical along the a-axis. If both the stable regions in the x-axis and the y-axis are plotted in the same graph, it is possible to discern the overlapping regions. These regions now exhibit the values for a and q where ions are not only stable in one but in both dimensions along the rod system (see figure 1.6). There are several intersections between both lines that could potentially be used as the basis for a mass filter but almost exclusively all QMF operate in the first area of stability, at q ≈ 0.7 and a ≈ 0.2[19]. Low a and q values represent low U and V which in turn leads to lower technical demands for power supplies and RF generators.

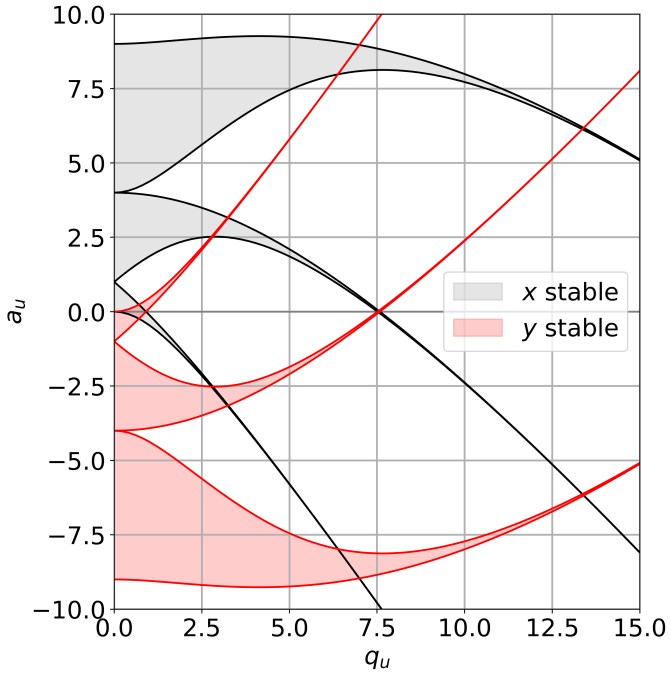

Figure 1.6: The 2D stability diagram. Grey shaded areas show a-q values for stable motion in the x direction while red shaded areas show a-q values for stable motion in the y direction

There has been some discussion about the utilization of the third stability zone[2], at q ≈ 2.8 - 3.2 and a ≈ 2.5 - 3.1[20, 21] and it is noteworthy that this zone does pose significant advantages and may be useful for niche applications. Neverthe-

[2]In some publications this area has been called stability zone 2 but for the sake of clarity in this work it will be denoted as stability zone 3

less, the first zone still remains the most suitable for almost all tasks. Without forestalling too many of the later topics, the advantages of the third stability zone are to be discussed briefly.
QMF exhibit significant problems in detecting very small m/z (more about this topic in chapter 1.3) but operating in the third stability zone mostly erases this issue. Also the peak shape is more symmetrical in this zone [22]. Furthermore the number of RF-cycles an ion has to spend in the device to achieve the same resolution as with a conventional QMF is reduced[23]. The shape of the stability zone (see figure 1.7) provides two narrow tips, in the lower left (q ≈ 2.81, a ≈ 2.52) and in the upper right corner (q ≈ 3.23, a ≈ 3.16) of the stable region, respectively, which allows for high resolution mass spectrometry[24].

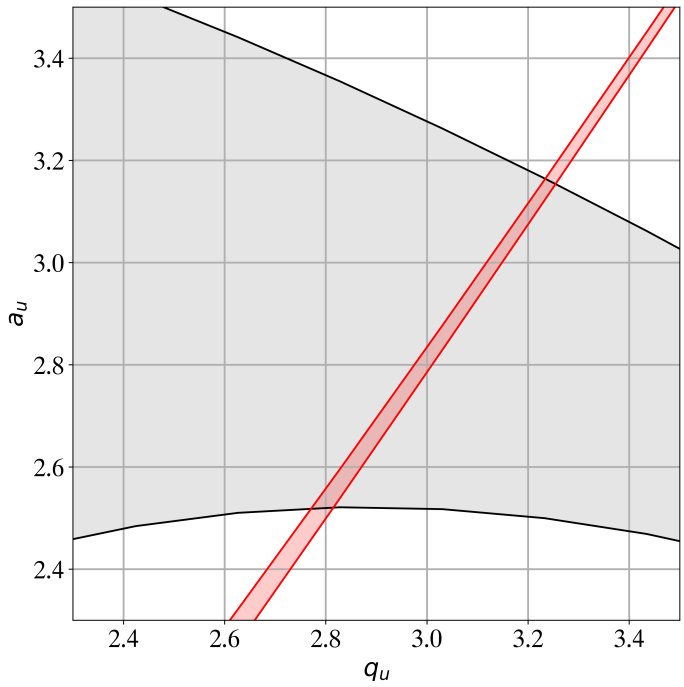

Figure 1.7: The third stability zone in the stability diagram

In addition, and likely the most favorable advantage, is the higher resolution achievable by the third stability zone[20]. All these advantages raise the question why the first stability zone is almost exclusively preferred over the third in commercial instruments. The response to that is the significantly reduced ion transmission in this region (and thus loss of sensitivity) which is compensated

only by i) higher pressure in the ion source generating larger amounts of ions and/or ii) higher analyte concentration. Overall the first stability zone thus shows higher performance compared to any other in the majority of cases.

The first region of stability (see figure 1.8, the area is shaded in grey for simplicity albeit it is a stable area for both x- and y-dimension) is shaped in a manner close to a pyramid with one curved side towards smaller a and q values. The slope starts at a=0, q=0 and the right end of this zone is located at a=0 and q=0.908. The tip, which is of highest interest, is located at q=0.705996 and a=0.237. As previously mentioned and also apparent from equations (1.21) and (1.22), which ultimately define the stability diagram, for a given ω, U, V and r_0 every ion with the same m/z ratio shares the same operating point in the stability diagram.

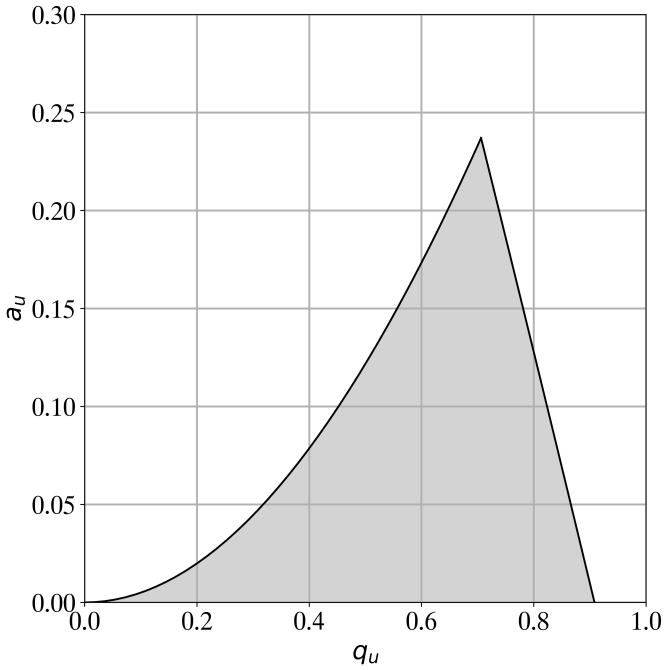

Figure 1.8: A more detailed view on the stability diagram showing the first zone of stability

Furthermore for given fixed operating conditions, the operating points for all m/z-ratiso lie on a straight line through the origin of the diagram with a slope $\frac{a}{q} = \frac{2U}{V}$ of, which is termed the operating line or mass scan line, which defines a

multitude of factors. Every ion with an operating point within the intersections of the mass scan line with the stability zone will follow a stable trajectory, while every ion described by an operating point outside of the stable zone will be filtered out. Increasing U and V while keeping the ratio of U to V constant, moves the operating points of all m/z values on that operating line from the lower left side further up and to the right, bringing one m/z-value range at a time into the region of stability. The slope of the mass scan line then defines the length of the mass scan line intersecting the zone of stability (see figure 1.9). The shorter the interval between two border points the higher the mass resolution, since the range of stable m/z-ratios is proportional to the interval length. However a smaller interval length introduces the downside of reduced transmission through the QMF, as discussed above.

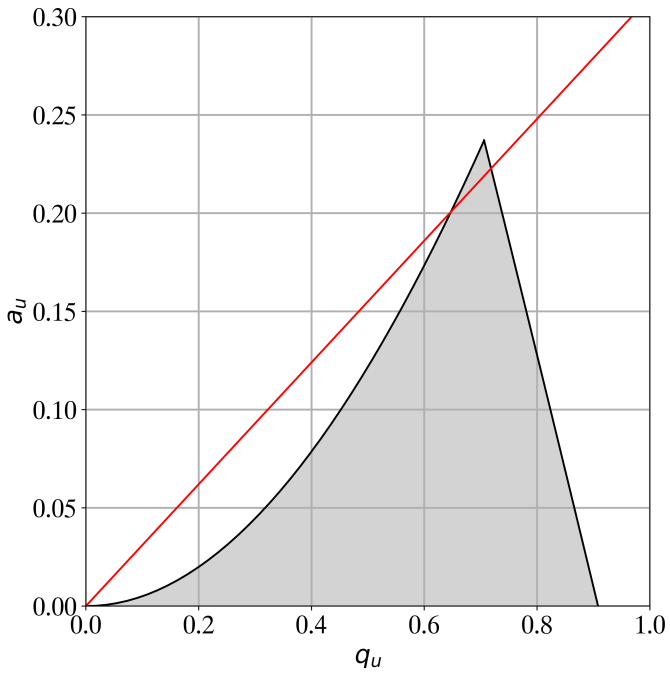

Figure 1.9: The first stability zone with an exemplary mass scan line

In view of the four possible cases that pose solutions for the Mathieu equations, more precisely the values for μ that represent a realistic solution, the one with $\mu = i\beta$ results in periodically stable motion. It was also mentioned that the exact value of μ, and in turn the value for β depend on the values for a and q

respectively. Thus it is possible to draw the β values into the stability diagram, differentiating between β_x and β_y values depending on their motion along the x- or y-axis. The β values dictate the nature of the ion motion; note that this does not mean ions with the same β values will follow the exact same ion trajectory but their motion will be of the same nature (see figure 1.10). The exact trajectories also depend on the initial RF-phase as ions first experience its influence, the displacement and the velocity in the x- and y- dimensions and the angle at which the ions enter the quadrupolar field.

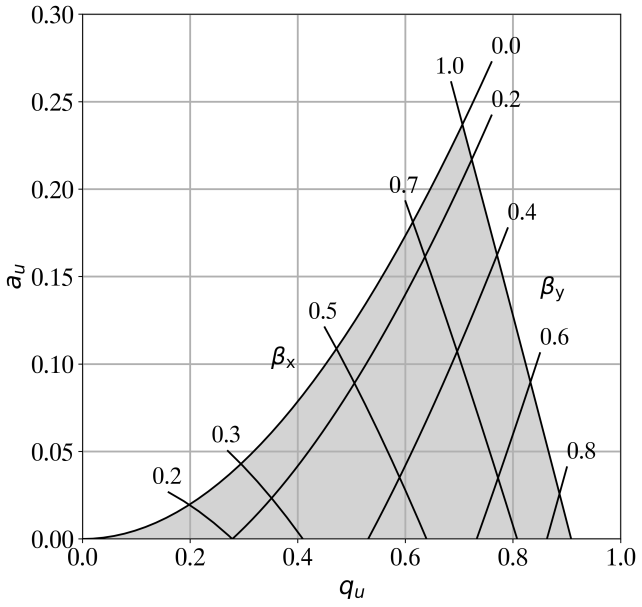

Figure 1.10: The first stability zone including iso-β lines

The fundamental frequency of the ion motion ω_0 is calculated with equation (1.27), while higher frequencies ω_1 and ω_2 are addressed with equations (1.28).

$$\omega_0 = \frac{\omega\beta}{2} \tag{1.27}$$

$$\omega_1 = (1 - \frac{\beta}{2})\omega \; ; \; \omega_2 = (\frac{1+\beta}{2})\omega \tag{1.28}$$

Introducing the two limits of the first stability region, β= 0 and β=1, into the equations for the fundamental and the first higher frequency, the period of the

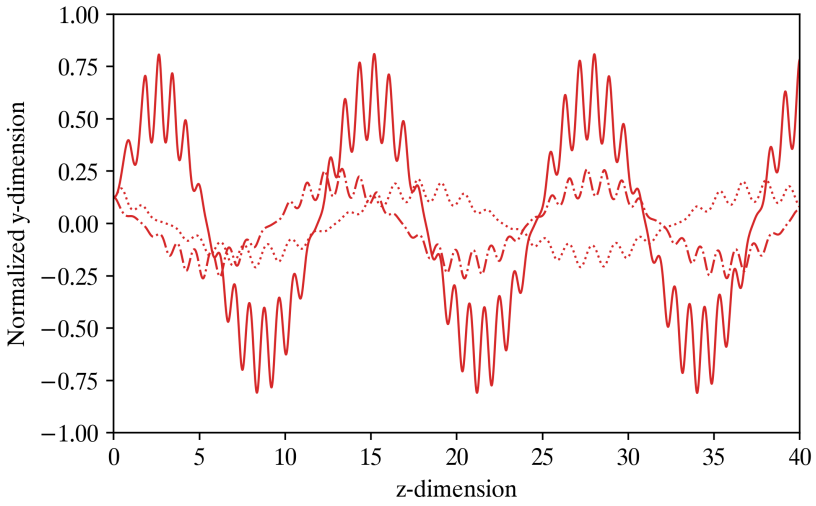

Figure 1.11: Trajectory comparison between ions with the same β values at three different initial RF phases

oscillation is calculated with $\tau_n = \frac{2\pi}{\omega_n}$.

$$\beta = 0 \ : \ \omega_0 = 0 \ ; \ \omega_1 = \omega \tag{1.29}$$

$$\beta = 1 \ : \ \omega_0 = \frac{\omega}{2} \ ; \ \omega_1 = \frac{\omega}{2} \tag{1.30}$$

These equations allow the calculation of specific frequencies of the ion motion throughout the quadrupolar field, for given β values. This provides insight into the amount of fundamental cycles the ion experiences during its dwell time in the QMF.

1.2.1.2 Resolution and ion acceptance

1.2.1.2.1 Resolution and mass scan lines The attainable resolution a QMF can achieve is generally dependent on the selected mass scan line and its intersections with the stable regions of the stability diagram. There is a mutual relationship between the peak height (or transmission rate) and the resolution[4]. Figure 1.12 shows the stability diagram, zoomed in on the tip of the first stable region, combined with the mass scan lines and the resulting resolution[3].

[3]These values were calculated assuming no fringe fields and perfectly axial ion entry

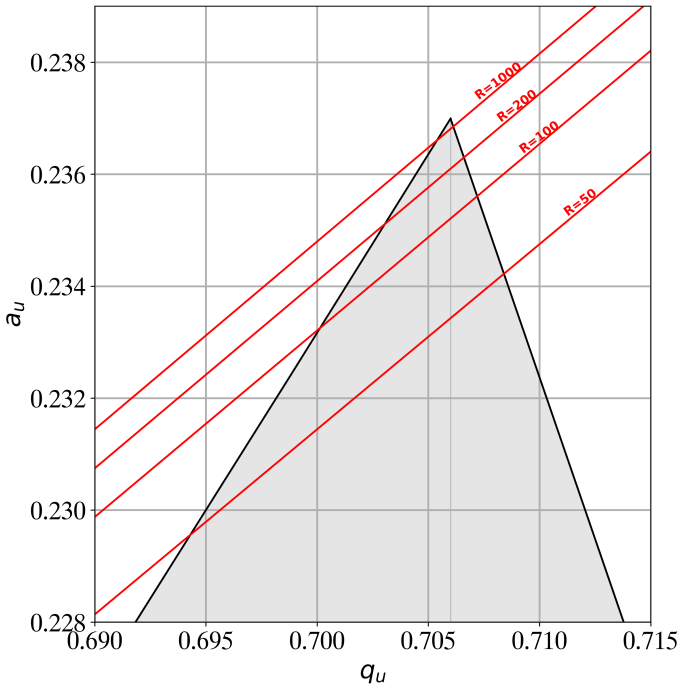

Figure 1.12: Visualization of several resolutions and the respective mass scan lines

The distance between the two intersections represents the amount of stable m/z ratios that can pass the device unfiltered and therefore the peak width will be the smallest, if only the very tip of the stability diagram is intersected by the mass scan line. However if that is the case, only a marginal amount of ions actually passes the filter, which results in decreased peak heights in the entire mass spectrum. The slope of the mass scan line is calculated using equation (1.31). The equation uses constants of the stability diagram and the a value that corresponds to q=0.705996 (the tip of the stable area) to give the resolution.

$$R = \frac{0.178}{0.23699 - a_{0.705996}} \tag{1.31}$$

It is clearly visible that the asymmetry of the stable region results in a disparity between the areas that are left and right of the tip. Owing to the imposed restriction for the mass scan line to intersect the origin of the coordinate system, the left side is larger than the right side. This results in a shift of the center of the filter window to the left, which is to higher masses, when the scan line is

lowered to decrease the resolution. To compensate for this behavier and to keep the filter window centered to the intended m/z, the amplitude of the alternating component of the applied potential needs to be adjusted while changing the resolution.

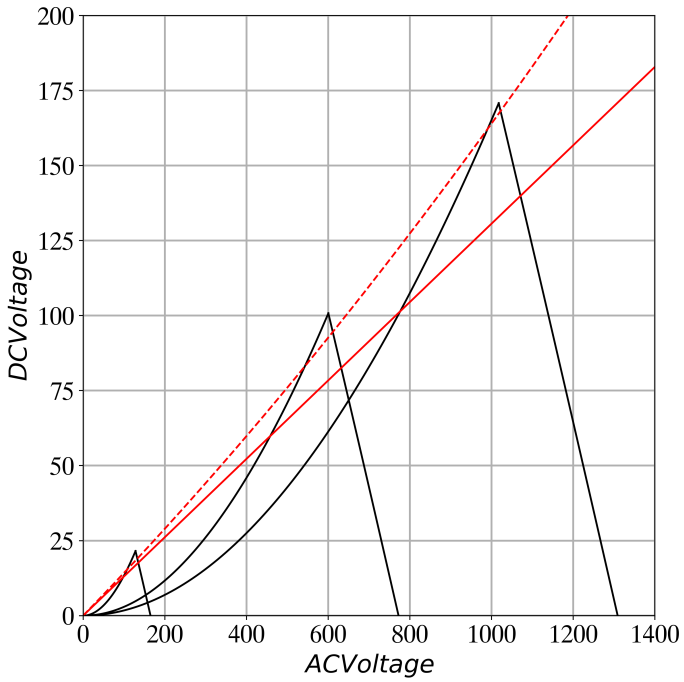

Figure 1.13: Stability diagram in terms of applied AC and DC voltages for ions with m/z28, m/z131 and m/z222. The straight red line represents a linear mass scan line and the dashed line represents a curved mass scan line where the slope increases as the scan progresses.

Another way to illustrate the influence of the stability zone on ions is a plot of U over V instead of a over q, as shown in figure 1.13. In this display, the stability zones for different m/z values separate from each other: The stability regions scale proportionally to the m/z-value. For simplicity, figure 1.13 does only show the lines of the stability border for the selected m/z values. While in the stability diagram as shown in figures 1.9 and 1.12, for a scan line with constant a/q ratio and therefore constant resolution R, the transmitted width or length on the scan line in units of q is constant for all m/z, in figure 1.13 it is apparent that the area between the intersections of the mass scan line and the stable zone is larger for heavier ions compared to smaller ions and this directly translates to broader

peaks at higher m/z. The dotted line shows a scan line with a rising slope over the course of the scan to amend the peak broadening. A device operated in this constant width mode shifts the scan line in order to achieve a constant width of peaks throughout the specified range of the mass spectrometer to obtain higher resolutions for ions of higher m/z. But, as mentioned earlier, an increase in resolution is accompanied by a decrease in sensitivity because of imperfections, injection conditions of the ions and physical limitations of the device.

Figure 1.14 shows the influence of a non-linear mass scan line on a mass spectrum consisting of Argon, Xenon and Radon with identical number densities. The peaks are narrower with the non-linear mass scan line, resulting in a higher achievable resolution. As a side effect the intensity of the peaks is reduced, owing to the fact that more ions of the respected m/z are lost in the QMF due to unfavourable initial conditions. It is thus possible to achieve the same peak width over the whole m/z range of the device at the cost of reduced peak heights.

This can be of particular interest if there are several large peaks close to each other at high m/z so that the reduction of intensities does not play a major role but the increased resolution is needed. It has to be stated though, that higher peaks suffer more decrease of intensities and that renders a comparison between intensities of low m/z and high m/z difficult without prior calibration in the mass range of interest.

The previous equations and theoretical rational all assumed an infinite instrument length which is, naturally, not realistic. With this in mind, one must distinguish between short- and long-range stability because ions can theoretically be filtered out at some point along the travel path but the instrument is simply not long enough. Ultimately, the metric to define if an ion spends enough time in the quadrupolar field to be filtered out is the amount of RF cycles n the ion experiences within that timeframe, and therefore, on the frequency of the AC component. More specifically, the resolution is proportional to n^2 (see equation (1.32)[24]) wherein n can be described with equation (1.33)[4].

$$R = \frac{n^2}{Constant} \tag{1.32}$$

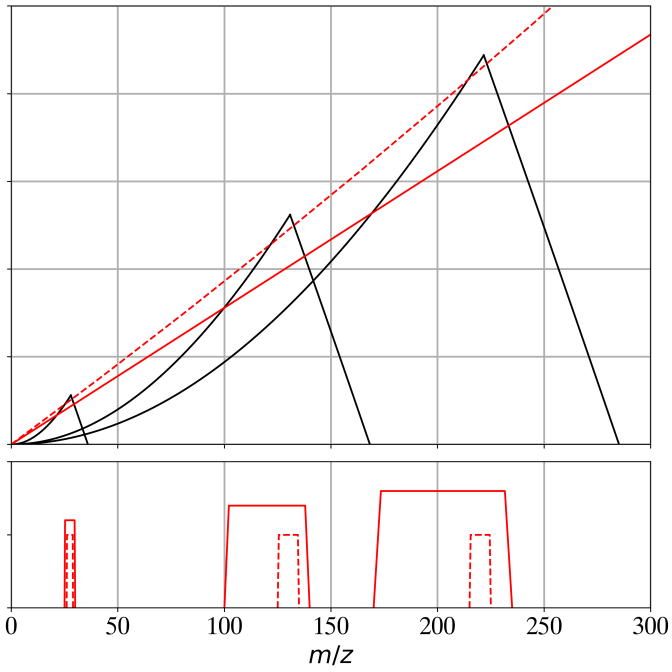

Figure 1.14: Depiction of the influence of a non-linear mass scan line (dashed line) compared to a conventional mass scan line (straight line) on a mass spectrum consisting of m/z40, m/z131 and m/z222.

$$n = fL\sqrt{\frac{m}{2eE_z}} \tag{1.33}$$

This equation illustrates the higher achievable mass resolution at higher m/z values, if all ions pass the quadrupole with the same axial kinetic energy E_z. This supports the higher resolution required to achieve the same filter width for higher m/z as discussed. This is already rooted in the working principles of quadrupole mass analyzers, since ions with a higher m/z are slower and thus spend more time in the quadrupolar field when starting with the same energy. However the mentioned concepts allow an even more enhanced resolution for a mass range that is often required in analytical applications[25].

1.2.1.2.2 Ion Acceptance The initial conditions of an ion entering the quadrupolar field (position, total kinetic energy, velocity vector) are crucial for successfully traversing the filter, even if mathematically stable trajectory conditions are assumed. For an optimal trajectory through the QMF, an ion should enter the rod system directly in the center with no velocity component in the x,y dimensions ($\dot{x}$=0 and $\dot{y}$=0). If ions differ from these initial conditions they might be neutralized on the rods before they can achieve their stable frequency and thus reach the end of the quadrupole. Naturally, an ion with a high displacement and low velocity might still be accepted and the same is true for ions with a high velocity and low displacement. It is also conceivable that an ion with a high displacement in the +x direction and a high velocity in the -x direction could be transferred with a stable trajectory. Figure 1.15 shows accepted ions, those that successfully reached the end of the quadrupole, near the top of the first zone of stability depending on their initial properties regarding x, $\dot{x}$, y and $\dot{y}$ values. These values were normalized to r_0 values, which means an ion with an x value of 1 is placed directly at the right side next to the rod system while an initial value of -1 indicates an ion at the left edge of the rod system. Velocities are normalized to the dimension $\frac{r_0}{\mu sec}$.

For the 0π graph it is discernible, that the QMF only accepts ions with a rather small displacement but a significant initial velocity. This trend is the same for the y-direction albeit mirrored, because the potential applied to the rods is naturally the opposite.

Shifting the initial phase of the alternating potential on the rods by 1π the picture of the accepted ions also shifts by the same value. The phase space in the x-dimension now resembles the previous y-dimension and vice versa owing to the shift in the electric field.

Between these two setups there is a transition state during which the potential on the rods is in the middle between the two extreme points (0π and 1π) and the depiction of accepted ions also shows a transition state between the two states they were at the extreme points of the electric field. During the transition state the phase space of the ions is bowtie shaped in the x-dimension and almost spherical in the y-dimension. Since ions can be located anywhere

in the phase space it is clearly visible that, even for mathematically stable ions, only a small amount can successfully enter the quadrupole and reach the end of the device without being filtered out. These diagrams indicate the importance of a matching aperture between the ion source and the entrance of the quadrupole to ensure that displacement and velocity of the ions along the x- and y-dimensions are close to 0 to maximize the amount of ions that enter the analyzer region within the desired region of the phase-space. It is not readily visible in these pictures but the total amount of accepted ions is also highest in the 0.5π initial phase.

In contrary to figure 1.15, figure 1.16 shows ions that were successfully transmitted through the quadrupole region and their respective locations in the phase space 2.5 mm after they left the rod region. It has to be noted though, that the device used for the simulations does not operate with a suited aperture to limit the influence of fringe fields created by the rods themselves or to narrow the ion beam dimension. It is discernible from the major differences between figure 1.15 and figure 1.16 that ions have to enter the quadrupole region with a somewhat limited spread in the phase-space whereas they exit the quadrupole with a wider spread along the velocity axis. In the phase-space of ions entering the device the x- and y-phase-spaces share some similarities, especially in the 0π and 1π simulations they represent almost mirrored images. The ions exiting the rod region show almost no similarities anymore but they do indicate the differences between the pairs of rods and their respective applied potential. The phase-space of the x-dimension shows a very focused ion beam after the quadrupole, not even stretching out to the limits of r0. This is due to the fact that these rods function as the low-pass filter, meaning they carry a positive mean potential focusing ions onto the center of the device while smaller ions experience an ever growing amplitude enforced by the superimposed RF. This results in a small x-displacement of stable ions throughout the device length. The y-dimension on the other hand defocuses ions with a negative net potential while stable ions can keep a stable trajectory due to the influence of the RF on their trajectory. This general disparity is depicted in these simulations, which also show that a focusing aperture in the region behind the rods is primarily needed for the y-dimension.

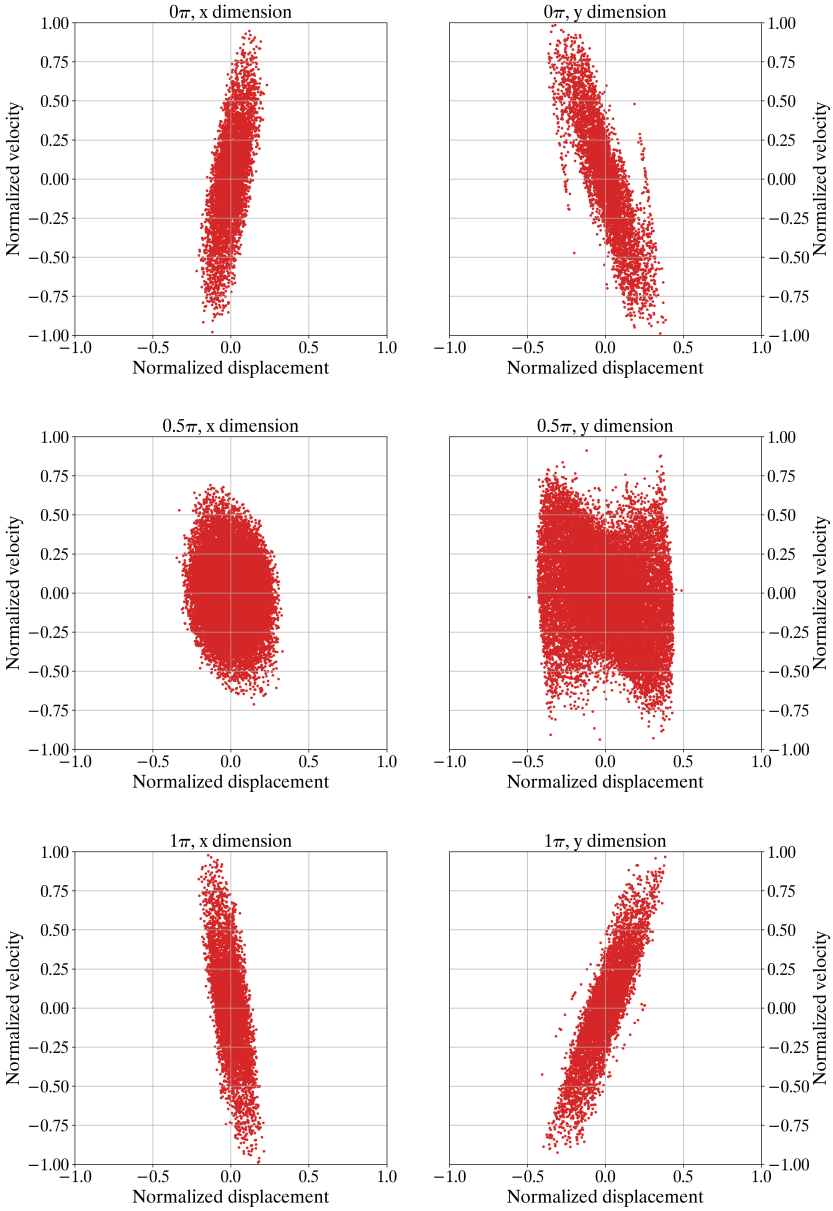

Figure 1.15: Normalized phase space of accepted ions with β_x= 0.8958 and β_y = 0.0733. *Top*: 0π initial phase of the electric fields. *Middle*: 0.5π initial phase of the electric fields. *Bottom*: 1π initial phase of the electric fields

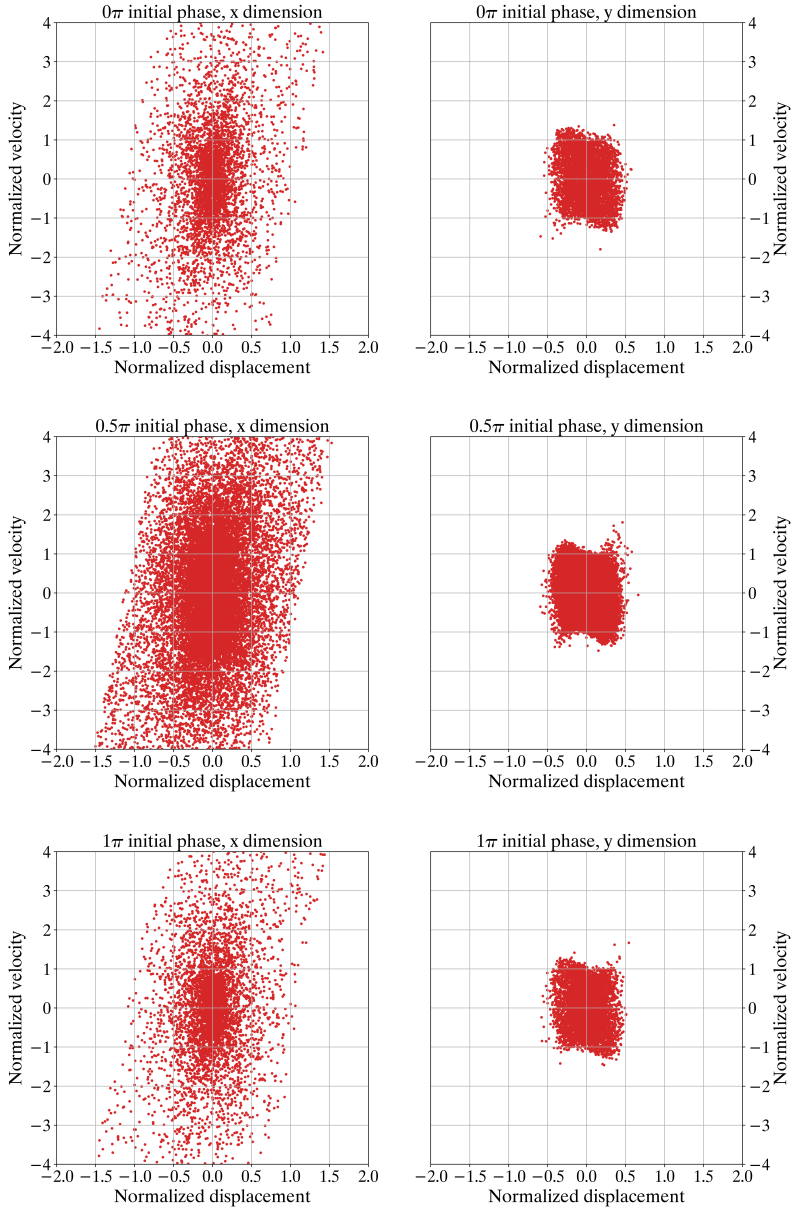

Figure 1.16: Normalized phase space of ions with β_x= 0.8958 and β_y = 0.0733 2.5mm after leaving the rod region. *Top*: 0π initial phase of the electric field *Middle*: 0.5π initial phase of the electric fields. *Bottom*: 1π initial phase of the electric fields

1.2.2 Detector systems

The detector system is a crucial part of any mass spectrometer device, however, the mechanisms and intricacies of different detector types are often overlooked and labeled as not as important compared to other parts such as the ionization source and the mass analyzer. The techniques used to detect ions and amplify the ion impact to a measurable electrical signal has gone through major advancements in the history of mass spectrometry[26]. In order to have a look at detection mechanisms of different detector types it is necessary to first consider possible reactions on the surface, which could potentially lead to a signal. In addition to an ion striking the surface and subsequently leading to a signal in the mass spectrum, there exists a myriad of possible reactions on the metal surface when not only ions but excited atoms/molecules and photons are taken into account as well. Generally, every electron generated on thw initial electrode (conversion dynode) will lead to a positive signal in the mass spectrum so these interactions are indistinguishable. To release an electron from a metal surface the minimum energy needed is the work function W of the metal[27]. The work function is defined for a clean surface which is not realistic in most situations unless the surface was specifically cleaned for the experiments. Surfaces are, in most cases, covered by adsorbed gases leading to changes in the surface interactions of particles. The different reaction mechanisms taking place on the surfaces of the detectors will be contemplated more in depth in section 1.5.

1.2.2.1 Faraday Cup

The faraday cup is the simplest detector in terms of mechanical and electrical complexity. It consists of a metallic cup-shaped structure axially of the ion beam exiting the mass analyzer. On the surface the mechanism of detection can be regarded as an ion striking the metal surface which induces an electrical current due to an electron being transferred from the metal lattice. The ion is neutralized in the process and thus the signal stemming from a specific ion is directly linked to the amount of electrons released upon impact. Most mass spectrometers employ more advanced detector systems, which utilize some means of amplification to increase the signal and only rely on faraday cups for supplementary experiments or as a second detector to fall back to.

1.2.2.2 Secondary Electron Multiplier (SEM)

In order to reach higher sensitivity compared to a faraday cup the amount of electrons released upon ion impact has to be increased. The SEM achieves higher currents by introducing two different techniques: The kinetic energy of the ion is increased by applying an accelerating voltage in the order of several kilovolts and the released electron is "multiplied" on several dynodes in an avalanche mechanism.
The increase in kinetic energy of the ion directly translates into a higher amount of electrons released on impact. A thermic ion may not be energetic enough to surmount the work function of the metal and thus no secondary electrons are released. A negative high voltage on the first dynode of the detector increases the kinetic energy of cations in order to make sure the work function of the metal is miniscule in comparison. The kinetic energy distribution of incoming cations is also insignificant with regard to secondary electron release efficiency, since the attractive potential on the conversion dynode leads to much higher kinetic ion energies. The total amount of secondary electrons is increased with higher incident energy, which increases the sensitivity of the detector as a function of the applied voltage[28].
To further increase the signal, the initial secondary electrons are accelerated as well and strike another dynode, which continues in an cascade electrode arrangement (avalanche process). On impact, the electron interacts with the electrons in the dynode and releases more electrons. There are between 12-18 discrete dynodes in a common SEM[28] leading to a total gain of about 10^6 to 10^9 depending on the exact material and potentials applied[29, 30].
The large multiplication factor of an SEM makes it vulnerable to other mechanism inducing a signal such as photons or excited species striking the first dynode. To avoid this, the SEM has to be located off-axis of the ion source in order to reduce the amount of false positive signals in the mass spectrum.
Since the first dynode of a secondary electron multiplier converts cations to electrons in positive mode or anions to cations in negative mode it plays a distinctively different role compared to the rest of the dynodes and thus can be held at a different potential and can be locally separated from the rest of the SEM if the geometrical constraints of the mass spectrometer allow such a setup. Another advantage of such an arrangement is that high voltages can be applied

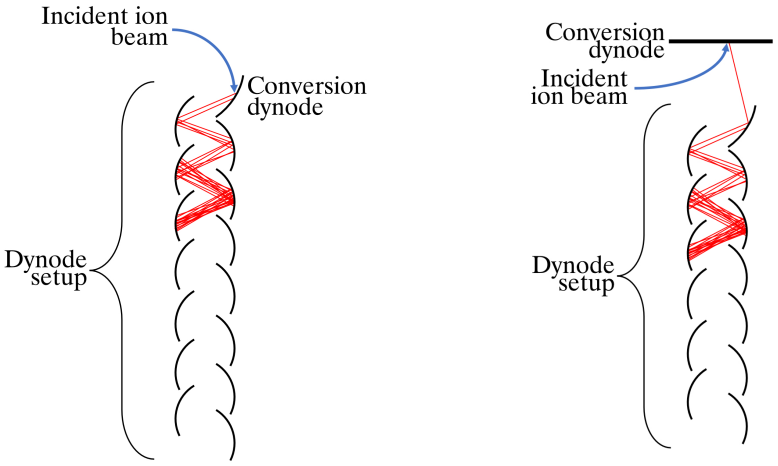

Figure 1.17: Different SEM setups depicting the ion beam (blue) and electron trajectories (red). Left: Conversion dynode incorporated in the dynode cascade. Right: Conversion dynode external of the dynode cascade.

to capture ions in cases where the ions have significant kinetic energies. The potential of the conversion dynode would be separated from the potential cascade of the dynode system as an entirely different, adjustable, potential which provides more flexibility. The possible reaction mechanisms on the surface of a dynode or the conversion dynode including photons, electrons, ions and excited species are analyzed in-depth in section 1.5.

1.2.3 Electron Ionization

1.2.3.1 General concepts

Since its first applicaton for gas analysis in 1929[31], electron ionization is still widely used in many devices. The mechanisms at work for this ionization method are complex by their quantum mechanical nature, however, a deep understanding of the underlying reactions is not necessarily needed to successfully incorporate this technique into a mass spectrometer. Electron ionization features distinct advantages and disadvantages compared to other techniques that have cemented their position in the field of mass analysis. Some of these mentioned advantages are listed below.

- No prior knowledge about the analyte needed
- Not limited to specific chemical properties
- unique compound or compound class fragmentation patterns allow the assembly of libraries

Non-selective ionization allows analysis of samples without knowledge of its composition at all, which renders EI useful for those cases. As long as the sample is in gaseous form it can be ionized using EI without adjusting ion source settings. A fragmentation pattern unique for every molecule opens the door for easy database assembly and thus library searches to improve analyte identification. EI can be used for a wide variety of analytes and is not limited by the necessity for specific chemical groups. These advantages illustrate why EI is employed in many mass spectrometer devices, even though it also has distinctive disadvantages as listed below.

- Ionization is not selective
- Ample fragmentation of large analytes
- Only viable in specific pressure ranges

Selective ionization for specific analytes clears up the mass spectra from carrier gas or matrix molecules since these are not ionized in most cases. Mass spectra acquired with electron ionization can be largely congested when fragile molecules are analyzed or a lot of different compounds are present in a sample.

This renders library assisted identification of individual species difficult if not impossible in some cases. Also the electron source cathode (filament) is susceptible to higher pressures as it will heavily degrade or even burn out if the pressure is too high. Additionally, the lifetime of a cathode is finite and regular replacement is needed in any cases.
The interactions between electrons and molecules, due to their principal quantum chemical nature, are a complex topic. The fact that these interactions can lead to many different products, some of which show up in the mass spectrum and some do not, renders the understanding of the underlying mechanisms a complex task. Especially the non-ionic products are invisible to the mass spectrometer unless specifically looked for.

1.2.3.2 Reaction mechanisms

A subset of the directly ionizing reactions in an electron ionization source are depicted in reactions R 1.1, R 1.2 and R 1.3[28].

$$M + e^- \longrightarrow M^{\bullet+} + 2\,e^- \qquad \text{(R 1.1)}$$

$$M + e^- \longrightarrow M^{2+} + 3\,e^- \qquad \text{(R 1.2)}$$

$$M + e^- \longrightarrow M^{.3+} + 4\,e^- \qquad \text{(R 1.3)}$$

The general mechanism involves an emitted electron from an electron source and the analyte molecule M. Interactions between the analyte and the electron can lead to a multitude of reactions but the directly ionizing steps lead to the ejection of an electron from the analyte molecule, generating a cation while the initial electron is slowed down due to energy conservation. It is notable that there is an unpaired electron present in cations with an odd amount of positive charges, which results in a radical cation or an open-shell ion while ions consisting of solely paired electrons do not exhibit radical character and are sometimes called closed-shell ions[28].
In addition to the reactions directly leading to ionized analytes, there is a myriad of possible mechanisms at work resulting in a complex system. Reactions R 1.4 to R 1.14 display the most common reaction routes for a three atomic molecule ABC[28, 32]. Reactions R 1.4 and R 1.5 highlight the possibility of reaching an

excited state of the molecule, which can have lifetimes of several seconds to minutes before it is de-excited in a corresponding reaction[33] or be of autoionizing nature and lose an electron to form a cation.
Dissociation reactions, such as R 1.6 to R 1.9 and R 1.11 to R 1.14 are crucial for the electron ionization process as they give rise to the fragmentation patterns governing the mass spectra obtained with EI. Electron capture reactions, depicted in reaction R 1.10, allow the usage of an EI source to detect anions with a mass spectrometer[34]. However the probability of electron capture is rather low when the ion source is not operated in a specific mode with much lower electron energies[35].

$$ABC + e^- \longrightarrow ABC^* + e^- \quad \text{(R 1.4)}$$

$$ABC + e^- \longrightarrow ABC^* + e^- \longrightarrow ABC^+ + 2\,e^- \quad \text{(R 1.5)}$$

$$ABC + e^- \longrightarrow AB^+ + C^\bullet + 2\,e^- \quad \text{(R 1.6)}$$

$$ABC + e^- \longrightarrow A^+ + BC^\bullet + 2\,e^- \quad \text{(R 1.7)}$$

$$ABC + e^- \longrightarrow AC^+ + B^\bullet + 2\,e^- \quad \text{(R 1.8)}$$

$$ABC + e^- \longrightarrow B^+ + AC^\bullet + 2\,e^- \quad \text{(R 1.9)}$$

$$ABC + e^- \longrightarrow ABC^- \quad \text{(R 1.10)}$$

$$ABC + e^- \longrightarrow AB^- + C^\bullet \quad \text{(R 1.11)}$$

$$ABC + e^- \longrightarrow A^- + BC^\bullet \quad \text{(R 1.12)}$$

$$ABC + e^- \longrightarrow AB^- + C^+ + e^- \quad \text{(R 1.13)}$$

$$ABC + e^- \longrightarrow A^+ + BC^- + e^- \quad \text{(R 1.14)}$$

This list of reactions is not complete but the major reactions are taken into account. The probability for each of them to occur is mainly dependent on the individual analyte[34] and the kinetic energy of the electrons[28] .

1.2.3.3 Ionization efficiency

An incoming electron cannot ionize a given analyte if its kinetic energy does not at least match the ionization energy of the analyte. It remains theoretical though, that an electron with the exact IE of an analyte can be utilized for ionization. The interaction is very seldom 100% efficient so the electron needs excess energy in order to transfer enough energy onto the analyte. To determine the likelihood of an interaction leading to an ionizing reaction, the ionization cross section is used. The dimension of the cross section is a area, because it reflects the area an analyte is spanning that an electron has to pass through to lead to an interaction[28]. The cross section is unique for every analyte but it is also based on the electron energy. Extensive research has been conducted[36, 37] to build a database of cross sections in order to easily compare ionization efficiencies of different analytes. An additional reason to study ionization cross sections is the fact that the same concentration of several analytes in the EI source may lead to signals with largely different intensities due to the different efficiencies in the ionization process. Figure 1.18 shows the experimental ionization cross sections for several atoms and molecules. The efficiency curve rises sharply from small incident electron energies, starting from the ionization energy of the analyte, to a maximum at the value of approximately 70eV (illustrated by the dashed black line) from which it slowly declines. Naturally the curves begin at the respective ionization energy of the atom/molecule. It is apparent that 70 eV electron energy is an efficient way of ionizing across a wide variety of analytes and for organic molecules, which make up a big fraction of relevant analytes (depicted in this graph as CH_4 and C_2H_4), 70 eV marks the maximum of the cross section.
The general shape of the graph is linked to the de Broglie wavelength of the incident electron which can be calculated using equation (1.34)[39].

$$\lambda = \frac{h}{m_e \cdot v} = \frac{h}{\sqrt{2 \cdot m \cdot E_{kin}}} \quad (1.34)$$

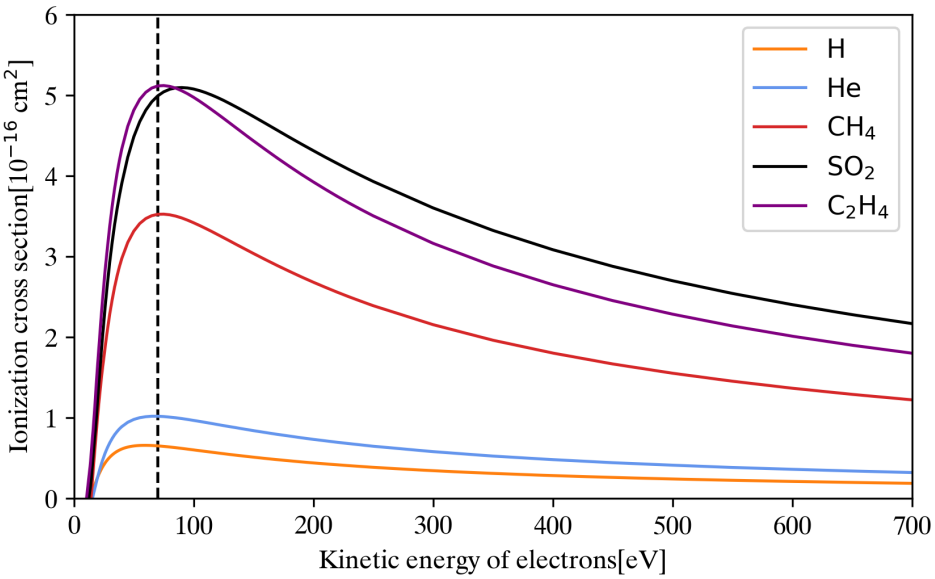

Figure 1.18: Ionization cross sections for selected atoms and molecules[38]

Assuming an incident energy of 70 eV the de Broglie wavelength of the electron is calculated as 1.46 Åand a typical C-C bond length is in the range of 1.426 Å to 1.462 Å[40]. The interaction of the incident electron with the bonding electrons increases as the wavelengths of the electron and the bond approach each other[41]. This phenomenon explains the maximum of the cross section at this kinetic energy of the electron for organic molecules being ionized via a dissociative reaction mechanism, as a C-C bond is broken in the process and at least one fragment ion is formed.

This approach is in good accordance with data for molecules while a more sophisticated concept is needed to explain the same observations for atoms, as there are no bonds present. It can be argued that the electron is in resonance with the electrons of the atom when the de Broglie wavelength of the incoming electron matches the size of the atom itself but it fails if the exact numbers are compared: The maximum of the ionization cross section for helium is located at approximately 115 eV[38] and that energy correlates to an electron of 1.14 Å. The diameter of a helium atom is approximately 0.62 Å[42] so the discrepancy of the diameter and the wavelength is significant.

In order to describe the course of the ionization cross section from another per-

spective the polarizability of the analyte is promising. It has been established that the polarizability exhibits a strong correlation to the ionization cross section[43] for atoms and molecules. The general approach is that the polarizability volume is the dominating factor an incoming electron experiences as it interacts with the atom or molecue. This interaction not only takes place between the incident electron and the outer shell electrons but with the total number of electrons present in the analyte atom or molecule[44]. Utilizing this approach the peak efficiency of the ionization is achieved as the de Broglie wavelength of the ionizing electron reaches the dimension of the polarizability volume of the analyte. Mathematically it is possible to derive an equation for the electron energy leading to the maximum intensity for atoms and molecules using the polarizability α, the ionization energy I_E, the electric charge of the electron z and the vacuum permittivity ϵ_0 as shown in equation (1.35)[44].

$$\sigma_{max} = \frac{z}{4\epsilon_0}\sqrt{\frac{\alpha}{I_E}} \tag{1.35}$$

Seeing from this equation, the maximum of the curve is proportional to natural constants and $\sqrt{\frac{\alpha}{I_E}}$ but it is pointed out that it is not a means to calculate the whole ionization cross section curve because for such a calculation a deep knowledge of every underlying quantum state would be needed, which is not feasible at this point. Nevertheless this approach allows the calculation of the maximum of the ionization cross section which in itself is a great tool for efficiency optimizations and further calculations.

The total rate of a reaction in a electron ionization source R can be calculated utilizing a rather simple correlation between the particle density in the source $\frac{N}{V}$, the emission current I, the cross section of the desired reaction σ and the effective length of the ionization source Δx with equation (1.36).

$$R = I \cdot \frac{N}{V} \cdot \sigma \cdot \Delta x \tag{1.36}$$

This is obviously just an approximation since defining an exact number for these parameters is difficult and on the mathematical side there are some approximations such as ideal gas conditions.

1.2.3.4 Excited non ionic species in Electron Ionization Sources

As apparent from reaction R 1.4, possible reaction mechanisms exist that result in the generation of an excited atom or molecule. The efficiency for such a reaction differs vastly for every substance since the excited states are unique as apparent from, for example, a Grotrian diagram. However it is possible to compare the efficiency of the excitation to the ionization in case the ionization cross section and the excitation cross section are both known. Unfortunately the complexity of interactions between electron and analyte further broaden the needed knowledge for such a comparison as not only the direct cross sections for the excitation and the ionization are needed. Several additional reaction pathways might be possible, which result in an ionic or a metastable state, e.g., reactions leading to autoionizing states[32] or excited instable states relaxing into metastable states via allowed quantum jumps[45]. These reactions increase the yield of ions and metastables respectively, compared to the direct ionization or excitation reactions. In order to calculate the total amount of ions and metastables the sum of these reactions and therefore the sum of these cross sections have to be taken into account.

The efficiency of the excitation processes can be described in the same fashion as the ionization process, using the excitation cross section instead of the ionization cross section as input for equation (1.36). The values for the excitation cross section are surprisingly large and can in some cases be similar to the ionization cross section so that the ratio of ions to metastables can be in the range of 0.1 to 10[46, 45]. These metastable atoms or molecules are a well-known by-product of electron ionization[47] however the effects they impose on other parts of the device are suppressed and the reactions are generally ignored unless specific experiments are to be conducted focussing on the metastables species themselves.

The time it takes for a particle to travel from a vacuum ionization the ionization source to the detector is usually in the microsecond range. Lifetimes of excited states that are not metastable and thus can undergo allowed quantum jumps to lower states can, generally, fall in the range of several nanoseconds[48, 49, 50]. Taking into account that the lifetime is not a sharp limit but rather the

time constant in the exponential curve describing the decay of the excited state (see section 1.4.3) it is evident that even after the time between ionization and detection a fraction of the excited states is still present. The amount of excited species after the given time naturally is small for some states and negligible for others but should still be taken into consideration.

1.3 Mass Discrimination

To this point in the discussion, ions of all m/z values are transferred from the ion source to the detector without any discrimination, but this is practically hardly feasible. Increasingly less successful or more successful detection of ions depending on their mass to charge ratio could lead to misinterpretations regarding the chemical composition of the analyte mixture. There are several stages in a mass spectrometer that could potentially be the culprits for discrimination targeting a specific m/z range[51]. This is not addressing different ionization cross sections for different neutral species, because they are not specifically discriminating towards the *mass* of the atom or molecule but are unique for every compound. The ion source itself cannot realistically, via its applied potentials on several electrodes, lead to a less efficient guidance for lighter or heavier ions. Applied potentials lead to a uniform kinetic energy distribution among the ions and also focus the ion beam, so that mass discrimination is not expected. For further discussion, it is assumed that ions exit the ion source with a uniform kinetic energy distribution and consequently that means that lighter ions have a higher velocity in the z-dimension compared to heavier ions.

According to equation (1.12) the the quadrupole does not accelerate or decelerate ions axially once they entered its electrical fields, so the kinetic energy is solely defined by potentials in the ion source and the gradient between the ion source and the DC bias of the rod system. As described in equation (1.33), the number of RF cycles an ion dwells in the QMF is directly dependent on the velocity in the z-direction and equation (1.32) shows that the amount of RF cycles dictates the attainable resolution. Hence it appears to be reasonable to transfer the ions as slow as possible from the ion source into the rod system to achieve the highest possible resolution. However this idea disregards the presence of fringe fields at the entrance and exit of the device, which influence

the trajectory of the ions and displaces them in an unpredictable direction. Thus the time an ion spends under the influence of these fringe fields is generally to be minimized. It was already discussed in section 1.1.2 that heavy ions experience a stronger influence from the fringe fields compared to lighter ions and that this effect can be reduced by introducing pre- and post-filters or by employing the ELFS technique as described in section 1.1.2. Another method to decrease the impact of the fringe fields is to accelerate the ions as they exit the ion source and decelerate them again as they enter the rod system. This is achieved by applying a low potential on the exit aperture of the ion source and a higher potential as bias of the rods to ensure the kinetic energy distribution of the ions is as desired.

Another potentially mass discriminating phenomenon that negatively affects quadrupole mass filters is the so-called "zero blast"[52]. At the beginning of a scan including low masses, the applied potentials are also small to keep low m/z in the stable zone of the device and allow them to reach the detector. However quantitatively filter out higher m/z ions, those low potentials may not suffice which, as a consequence, can lead to stable trajectories for a multitude of different m/z. These trajectories are not mathematically stable of course but may still reach the end of the rod system due to the limited length of the device. Subsequently a large signal is visible in the mass spectrum at very low m/z owing to the ions that reached the detector despite not actually consisting of the respective m/z value.
The magnitude of this "zero blast" effect depends mainly on the size of the device, namely the length of the rod system, the rod radius and the interrod radius, as in a more sizeable rod system the applied potentials have to be higher as well, cf. equations (1.21) and (1.22). This has posed some challenges for very small devices to baseline-separate the zero blast signal from a hydrogen signal at m/z=1[53] but in general this effect is only relevant for niche cases, while commercial quadrupole mass filters do not show a zero blast to a significant extend.

Additionally another section of a mass spectrometer apart of the ion source and the analyzer, could potentially give rise to problems regarding mass discrimination: The detector setup. A detector commonly used in mass spectrometers is the secondary electron multiplier. The conversion dynode of

the SEM has to be situated off-axis from the ion source, as to prevent photons and neutrals from inducing unwanted signals[54]. To achieve off-axis detection it is necessary that ions, after leaving the quadrupolar field, are guided towards the detector. Heavy ions need larger forces to change their direction compared to light ions. Assuming the field bending the ion trajectories is not adjusted over the course of a mass scan, heavy ions could be less effectively transported towards the detector[55]. The SEM itself does show a dependence of electron yield on the incoming ions but that is superimposed by the quantum mechanical properties of the ion instead of the mass. As a result heavier ions generally lead to a lower number of electrons but could in some cases can also lead to a higher yield. There is an expected amount of mass discrimination for this detector type[56, 57] however calibration prior to an analytical experiment generally renders this problem negligible.

1.4 Excited Electronic States of Atoms and Molecules

Since electron ionization sources produce large quantities of non ionic excited species, an analysis of said electronic states in order to understand their impact on the performance of the mass spectrometer device ismandatory. The complexity of this topic is amplified by the presence of more than one species, which suggests the differentiation between atoms and molecules. However a comprehensive and detailed study of this topic is beyond the scope of this work and thus only relevant parts of the theory which add to the understanding of this work are presented in the following sections.

1.4.1 Atoms

The energy required to transfer an electron to an excited energy level is dictated directly by the energy discrepancy of the lower and the higher level. The energy states themselves can be calculated directly using equation (1.37) using the principal quantum number n, the reduced mass of the electorn μ_e and constants e, π, ϵ_0 and $\hbar$[58].

$$E_n = -\frac{\mu_e e^4}{2(4\pi\epsilon_0\,\hbar)^2}\frac{1}{n^2} \tag{1.37}$$

It is apparent that the energy of a given state only depends on the mass of the atom and the mentioned quantum number. The mass does not change between

quantum states but the principal quantum number does so it is the leading factor in identifying the energy needed to jump from one state to another. The distance between the ground state (n=1) and the next one (n=2) has to be transfered precisely in order to successfully transport the electron into the first excited state. The source for that energy is either absorption of a photon of the exact wavelength[59], electron bombardment[60], a charge transfer reaction[61], stemming from an electric discharge[62] or thermal energy[63][4].
Since the only contributing factor to the energy of an electronic state is the principal quantum number, the amount of excited states is limited and the energy discrepancies between those levels are precise and discrete. Unless there is another way of disposing of excess energy, like another particle that can take up the energy as kinetic energy, the reaction onto the excited state cannot occur.
Once an electron is in the excited state there are possible pathways for the atom to dispose of the energy of the excess energy and return to the ground state that can be grouped up in two categories: Radiative and non-radiative transitions.

For a non-radiative transition to occur the energy necessarily needs to be transferred to another particle, as the atom does not possess any other means of disposing the excess energy. It has to be noted that in low pressure regimes the lifetime of most excited states is not long enough for collisions to happen so the non-radiative decay plays a more pronounced role for metastable states under conditions where collisions appear frequently. These transitions can take place when an excited species collides with another particle or a surface, to which the energy is dissipated and the excited atom returns to a lower energy state. There exists a multitude of possible reaction routes specific to the involved species[64, 65], which will not be discussed in detail as their number would exceed the scope of this work. However emphasis should be put on homoatomic energy transfer reactions (reaction R 1.15) since it acts as neither a sink nor a source for excited species and indicates that not every reaction results in the de-excitation of the excited particle[49].

$$A^* + A \longrightarrow A + A^* \qquad \text{(R 1.15)}$$

[4] Only applicable to species with a metastable state very close in energy to the ground state

Another reaction that plays a noticeable role in mass spectrometry is the reaction underlying penning ionization[66] This reaction can occur if the energy of the excited state is larger than the ionization energy of the collision partner so that ionization of the neutral species is possible (see reaction R 1.16).

$$A^* + M \longrightarrow A + M^+ \qquad \text{(R 1.16)}$$

The non-radiative decay of excited states can proceed via several reactions as well, while the most significant processes are fluorescence and phosphorescence. These two concepts signify a very similar mechanism: A photon of the exact wavelength is emitted and the electron returns to a lower energy state in the atom. However the main difference is the time between the excitation and the emission of the photon. Fluorescence is on the timescale of nanoseconds while phosphorescence can take several seconds to hours, depending on the states involved[67]. This difference stems from the spectral selection rules that dictates the probability of a given transition. A photon is defined by its spin angular momentum of s=1 and consequently the angular momentum of an electron has to change by this value to obey angular momentum conservation. As a direct consequence a transition from an s-orbital to an s-orbital is not allowed owing to this spectral selection rule. In order to obey this rule the azimuthal quantum number l would need to change by l±1 which translates to a change in orbitals[68].
Short lived states are generally depopulated by fluorescence mechanisms in triplet-singlet conversions which follow the spectral selection rule mentioned while metastable states usually break this rule which lowers the probability of the de-excitation step to proceed drastically and thus increases the lifetime of said state. The lifetime of metastable states can reach several seconds[69] or even minutes[33].

1.4.2 Molecules

Contrary to atoms, molecules can store energy in vibronic and rotatory states, which complicates matters. The added states allow excited electrons other possibilities of de-excitation. These mainly contribute to the non-radiative transitions as radiative decay still requires a photon to be emitted and similar mechanism are at work.
Two such additional mechanisms are internal conversion (IC) and intersystem

crossing (ISC). Both of these mechanisms involve the non-radiative transitions between two different electronic states and are possible owing to the added number of states an electron can occupy in a molecule. Due to the additional rotatory and vibronic energy levels an intersection of two potential energy curves is possible, which allows an electron to change from one to another on such an intersection. The difference between these two concepts is that during an internal conversion the multiplicity of the system does not change while it does change if ISC occurs[70]. The radiative decay routes still follow the same mechanisms, albeit with more convoluted spectral selection rules, but since IC ans ISC allow a transition between possible electronic states it is harder to pinpoint how a given system will react due to the manifold of possibilities and the density of vibronic and rotatory states which give rise to a series of complex interactions.

1.4.3 De-excitation kinetics of excited species

For a given excited atom the lifetime τ is influenced by several factors. If the pressure is sufficiently high the atom experiences collisions with other gas-phase particles which may lead to energy transfer reactions and subsequently to relaxation of the excited state. The same argument applies for collisions with a surface, if a collision with a surface is likely to occur.
However both of these relaxation channels are only viable sinks for the excited species if a collision occurs during the radiative lifetime of the excited state. The chance for a collision induced relaxation to occur, which can only shorten the lifetime of the excited state, is naturally influenced by the pressure[71], the type of collision gas[49], the excited state in question and the time it takes for the ejection of a photon to occur[33].

The radiative lifetime of most excited states is so short that collisions only play a significant role if the pressure is elevated. However the lifetime is not a sharp limit of how long a given state can live but the time after which the concentration c_0 depletes to $c_0 \cdot \frac{1}{e}$. The decay follows a first order kinetics which is characterized by an exponential function approaching 0 as seen in figure 1.19

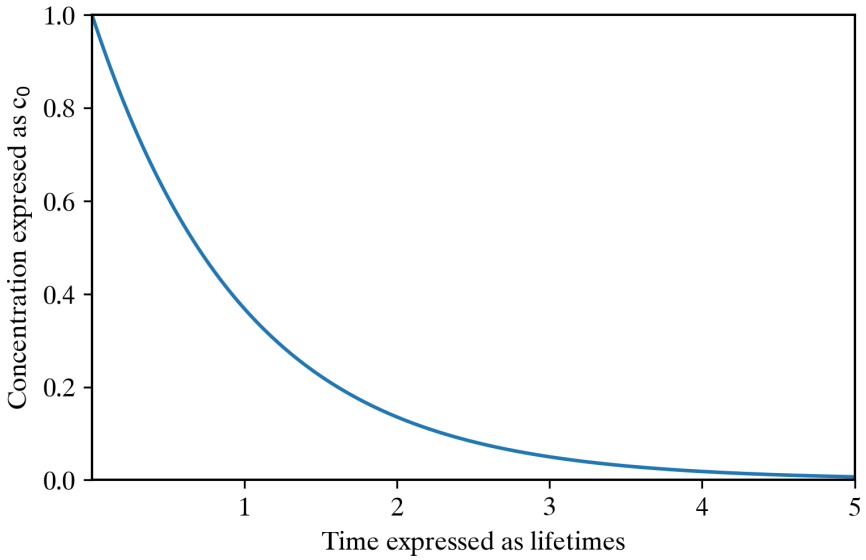

Figure 1.19: Exponential illustration of first order decay

As apparent from the mathematics behind exponential decay the remaining concentration after five lifetimes is still at $0.0067\,c_0$. This means that traces of the excited atoms can still be present after several lifetimes and depending on the exact amount of created excited atoms these traces can still be detected.

1.5 Surface reactions of selected particles

The interactions between a metal surface and a particle naturally differ drastically depending on the character of the incident particle and the surface. In the following section the reactions of photons, electrons, ions and excited species on metal surfaces will be taken into consideration.

1.5.1 Photon - metal interaction

The major reaction taking place on a metal surface when hit by a photon of sufficient energy is the photoelectric effect[72]. The energy of the photon leads to emission of an electron. The energy of the photon dictates the speed of the electron, as any excess energy above the work function is directly converted into kinetic energy of the electron, as per equation (1.38).

$$h\nu = W + E_{kin} \tag{1.38}$$

The efficiency of this reaction is independent on the incident angle of the photon which means the energy can still be transferred into the metal even if the detector is not perpendicularly oriented to the photon beam[73]. The energy of the emitted electron is independent on the intensity of the light beam[5] however if every photon is capable of leading to a emitted electron the total amount of electrons is governed by the intensity. An oxidation layer on the surface reduces the efficiency drastically and so do layers of other substances hindering the photon from interacting with electrons inside the lattice of the metal itself[73]. The general mechanism, in very short terms, can be divided into three steps: Excitation of the electron in the lattice by interactions with the photon, transport of the electron to the surface and escape from the electron into the vacuum[75]. During the second step of the mechanism the electron can lose its gained energy by electron-electron scattering on its way to the surface which implies that electrons can only leave the metal if it has not been released in deeper regions of the metal lattice.

[5] Unless intensities get high enough for multi photon absorption to take place[74]

1.5.2 Electron - metal interaction

Quiet similar to photons, the emission of electrons from a metal by electron impingement is directly dependent on the energy of the incoming electron. In contrast to the interaction between photons and metals though, the yield of secondary electrons does show a maximum when plotted against incident electron energy[76]. The most eficient energy considering the secondary electron yield is unique for every metal, which implies a mechanism inside the lattice of the metal taking place which naturally differ from metal to metal and the fact that higher incident electron energy does not always result in higher yield indicates that there are at least 2 trends going into opposite directions. The mechanism is similar to the described three-step mechanism in the previous section. At higher kinetic energies electrons penetrate further into the metal lattice and interact with electrons leading to a higher secondary electron yield. At some point however secondary electrons are excited too deep within the lattice so that they can't escape into the vacuum before losing their energy on the way, which leads to a decrease in secondary electron yield after the impinging electron energy reached the maximum[76]. Keeping this mechanism in mind it is apparent that the effect of the angle of incident is no major contributing factor to the secondary electron yield. At sharper angles the electrons are emitted from closer to the surface and the probability of reaching the vacuum is increased[77] .

1.5.3 Ion - metal interaction

The emission of electrons from metal surfaces induced by ion impingement can be divided into two mechanisms: Potential emission (PE) and kinetic emission (KE). In a PE mechanism the potential energy of the ion is sufficiently high to surpass two times the work function to lead to the ejection of an electron from the metal lattice which renders this reaction the most dominant for slow and highly charged/excited ions[78]. For higher ion velocities the kinetic emission reaction starts to contribute to the total electron ejection until it takes over the major part as velocity further increases.

To distinguish these mechanisms the distance to the surface is taken into account. PE mechanisms involve the tunneling of an electron into the metal which can happen before the ion is penetrating the lattice; however KE reactions

occur after the ion has hit the surface. As PE reactions occur the charge of the ion can be lost in an Auger process and the impinging particle is merely a neutral species, which leads to the ejection of electrons owing to its kinetic energy as well. As a direct consequence the mechanism of neutral particles has to be taken into account to receive a realistic electron emission rate for ions.[78] The electron yield from a given metal surface naturally indicates a significant dependency on the incident ion velocity. However it does not follow a purely linear function and at higher velocities even starts to decline again[79]. This may be due to the ion penetrating too far into the metal which reduces the chance for the electron to reach the vacuum.

1.5.4 Excited species - metal interaction

1.5.4.1 General thoughts

The interaction between an excited atom or molecule and a metal surface is of great importance for the topic of the present work, it is thus discussed more thoroughly. First of all the probability for the deexcitation on the surface should be considered to establish a baseline chance of a reaction taking place: The energy of the excited species needs to be transferred into the metal it is synonymous with a deexcitation. Naturally the probability of an interaction is, among other parameters, dependent on the metal and the exact excited level. For the sake of simplicity the $1s_3$ and $1s_5$ metastable levels of Argon will be used as an example for the rest of this chapter unless stated otherwise. For these metastable energy levels the deexcitation probability on stainless-steel surfaces is measured to be 0.88±11 and 0.84±11 respectively[80]. The deexcitation process can occur via two different mechanism: Auger neutralization (AN) or Auger deexcitation (AD).

1.5.4.1.1 Auger Neutralization and Auger Deexcitation Auger neutralization (AN) can be further subdivided into two separate mechanisms. First, resonant ionization (RI) takes place during which the excited electron tunnels into an unoccupied state of the metal, effectively ionizing the metastable species to a cation. This is directly followed by Auger neutralization as one electron from an occupied state of the metal fills the now vacant ground state and neutralizes the

charge while another electron from an occupied state is ejected into the vacuum to maintain energy conservation[81].

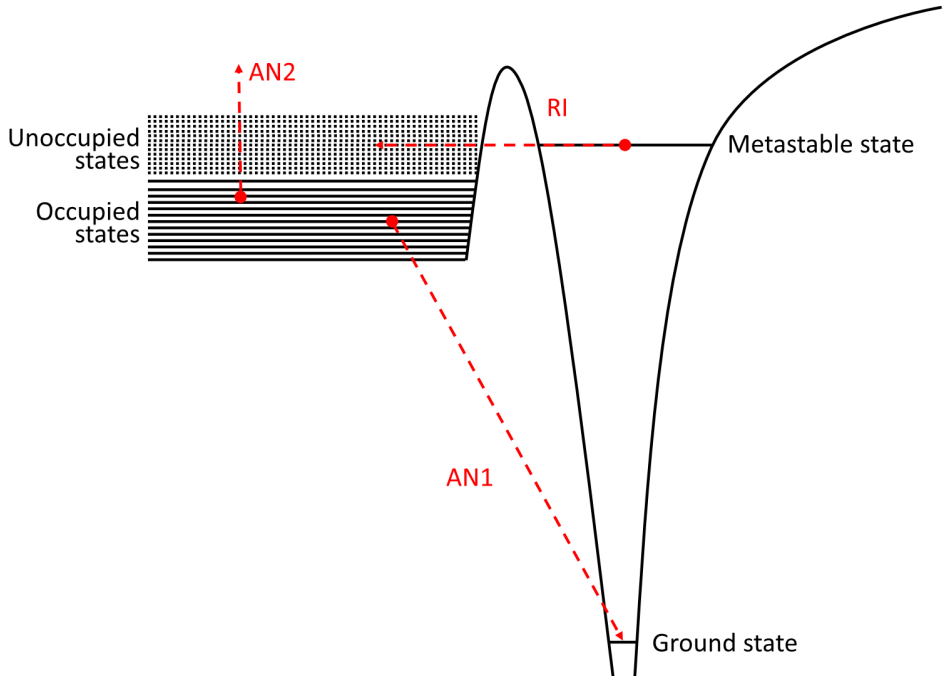

Figure 1.20: Depiction of the resonant ionization mechanism followed by Auger neutralization.

In order for this mechanism to take place the energy discrepancy between the Fermi level of the metal and the excitation energy of the excited species need to be taken into account. Considering resonant ionization as the first step of Auger neutralization, the work function of the metal has to be larger than the effective ionization energy of the metastable state $E^*_{I,eff}$, which is the difference between the ionization energy of the atom and the energy of the excited state E^* at the surface[82].

$$W > E^*_{I,eff} \tag{1.39}$$

After the metastable species is ionized, the neutralization process takes place during which 2 electrons are ejected from the metal. Considering the energy that is involved in these processes the total kinetic energy of the electron can be calculated by equation (1.40) using the mean binding energy of the two electrons

E_{bind} together with the work function W and the effective ionization energy $E_{I,eff}$ of the ground state.[82]

$$E_{kin} = E_{I,eff} - 2(E_{bind} + W) \tag{1.40}$$

From this equation it is possible to deduct the minimum energy needed for this mechanism to occur via equation (1.41).

$$E_{I,eff} = 2(E_{bind} + W) \tag{1.41}$$

It was mentioned that the electrons leaving the metal can originate from any occupied state within the metal, which in turn leads to an evasive parameter since the exact levels that these electrons leave from can vary depending on many factors and is the main culprit for the fact that the kinetic energy of the electrons yields a spectrum instead of few constant values[83].

In contrary to Auger neutralization, Auger deexcitation (AD) is a one-step mechanism: An electron from an occupied state of the metal tunnels into the ground state of the atom and in a concerted step the excited electron is ejected into the vacuum[81].
The energy condition for this mechanism can be calculated using the effective ionization energy of the metastable state $E^*_{I,eff}$, the work function W and the initial energy of the electron in the metal $E_{electron}$.

$$E^*_{I,eff} > W + E_{electron} \tag{1.42}$$

As apparent from equation (1.42) there is yet again a factor that is undetermined, which leads to a broad electron energy spectrum: The energy of the electron in the metal.

Comparing equations (1.39) and (1.42) it is evident that the conditions for these two mechanisms are directly opposed. Essentially the relation between the work function and the ionization energy of the metastable state dictates which mechanism can realistically take place even though they appear to be interchangeable. The previous considerations of the equations describing the interactions are not complete and there are some more in-depth concepts that highlight the complexity of Auger processes. Realistic concepts such as

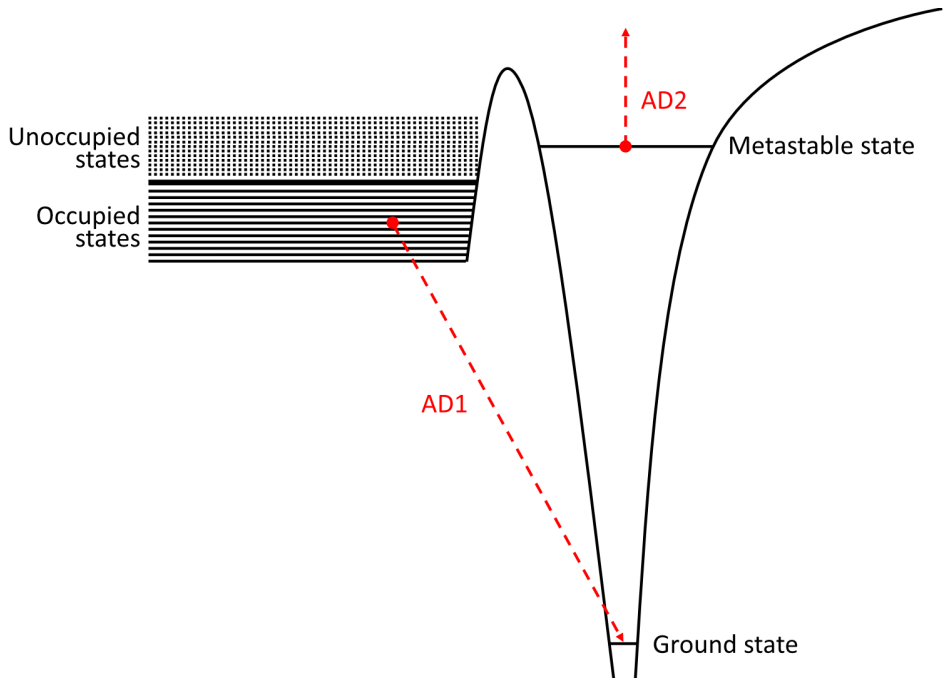

Figure 1.21: Depiction of the mechanism of Auger deexcitation of metastable states.

adsorbed gases on the surface, impurities in the metal and imperfections of the metal lattice can drastically influence the work function and the energy levels of the metal which naturally can lead to a change in the overall mechanism.

1.5.4.2 Distance to the surface

It was already mentioned that the parameter $E_{I,eff}$ is the effective ionization energy near the surface. Since this is a crucial factor in the mechanism it demands more attention. As a molecule or atom in the gas phase approaches a surface, the orbitals start to interact with each other. A repulsion of the outer electrons influences the quantum mechanical states of said electrons which in turn lowers the ionization energy of the gas phase species[82]. In this case the occupied state rises in energy as the electron experiences the outer force, the ionization energy is effectively lowered because the energy gap between the occupied state and the ionized state becomes smaller. The link between the ionization energy and the distance to the surface directly translates into a link between the mechanism and the distance to the surface. Excited states that used to be too high to undergo one

of the described mechanisms may be below the threshold as the ionization energy is lowered. As a direct consequence the distance to the surface needs to be considered when contemplating the possible mechanisms of a given metastable state. Additionally the potential curves of the metal and the particle need to overlap to give rise to an interaction so for some of the reactions the distance to the surface has to be very small. Since different reactions follow different mechanisms the demands for the specific reaction can differ greatly. Focusing on the interaction between an excited neutral species and a metal surface the three mentioned mechanisms RI, AN and AD take place at specific distances to a surface[84]. As the excited species approaches the surface the first thing to happen is the electric fields of respective valence electrons experience each other, which allows for resonant reactions, namely RI, to occur. The Auger interactions require a closer approach to the surface because the potential curves of the particle and the surface need to interact with each other, while for resonant interactions only the curves of the excited species and the ionic species need to overlap.

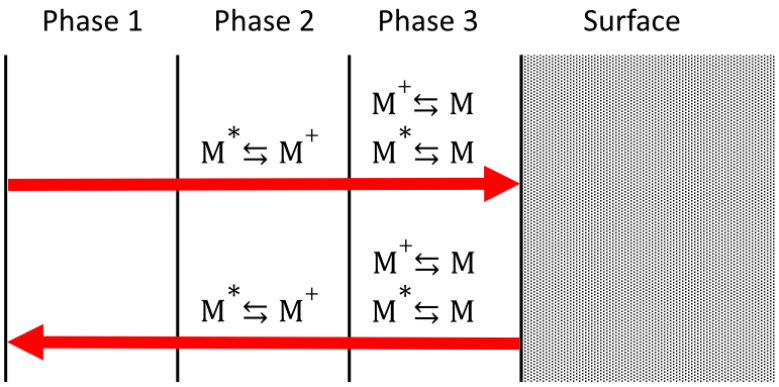

Figure 1.22: Several phases an excited species experiences on its way towards to and away from a metal surface.

With these conditions in mind it is possible to separate the distance between the particle and the surface into several regions in which different interactions can occur (figure 1.22). In phase 1 the system does not satisfy equation (1.39) so no interaction can occur. As the excited particle reaches phase 2, the ionic and the metastable potential curves intersect and the possibility for RI arises. The opposite reaction is just as possible, if the species approaching the surfaces was

an ion in the first place. Depending on the parameters of equation (1.39) there are some combinations for which the conditions for RI do not demand proximity to a surface because the energy of the excited state is close enough to the energy of the ion so phase 1 does not exist for such cases. In phase 3 the potential curves of the metal and the excited particle or ion allow Auger interactions to take place. On the outbound path from the metal surface these phases are gone though once more so there is another possibility for these reactions to occur[84].

2 Experimental section

2.1 Hi-Quad

Almost all experiments were conducted within a QMG 422 residual gas analyzer system (Inficon, Bad Ragaz, Switzerland).
The basis of the system is the Sputter Process Monitor (SPM) 700 which is compromised of the mass spectrometer with all the necessary parts: An ionization source, an analyzer and a detector unit.
The system relies on electron ionization in a closed SPM ionization source (Pfeiffer Vacuum GmbH, Aßlar, Germany) with an operating pressure of 3×10^{-2} mbar. The ionization source possesses four discrete electrodes which can be maintained at any given voltage in the range of -150 V to 150 V. The ionization chamber is a cylindrical entry into the ion source with a separated curved filament on each side. The whole cylinder is biased to the specified *Ion Reference* voltage as all remaining voltages directly refer to this potential instead of ground. The flow restriction in to the remaining lens system and the analyzer region is the extraction electrode with an inner diameter of 1 mm held at the *Extraction* voltage. Downstream of the extraction electrode there is an einzellens consisting of a cylindrical aperture held at the *Focus* potential. The ionization source ends with the entrance plate leading into the analyzer region held at ground potential. Figure 2.1 depicts the ion source (washers and screws not shown). Table 2.1 summarizes the specified settings of the ion source. *Emission* sets the emission current flowing from the filament towards the ionization chamber and can be set between approximately 0.01 mA and 2 mA. The value *Protection* limits the primary current through the filament itself to heat up the wire material and cause electrons to leave the filament. If the primary current through the filament exceeds the specified value the filament will shut down to protect the wire from burn-out. The filament material was commercially available tungsten welded onto a filament holder in a commercially available set. *Field Axis* is the

bias on the rod system in order to ensure the kinetic energy of the ions is at a desired level when they enter the analyzer region.

Table 2.1: Standard values of ion source settings

Ion Reference	150 V
Extraction	-80 V
Focus	-7 V
Field Axis	-10 V
Emission	1 mA
Protection	4 A

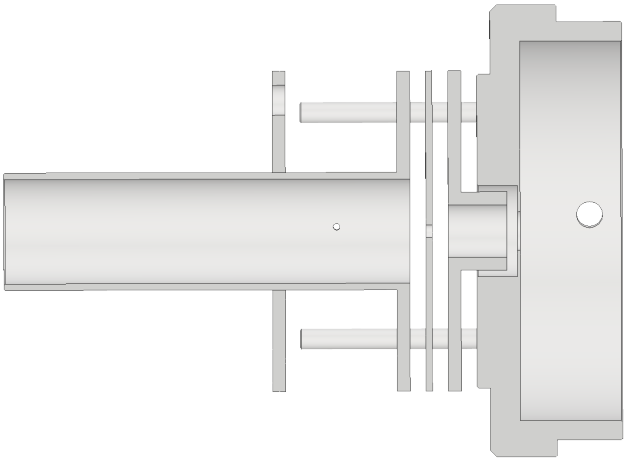

Figure 2.1: Representation of the SPM electron ionization source

As the ions traverse the entrance plate they enter the analyzer region. A quadrupole assembly is used as a mass analyzer (QMA 430, Pfeiffer Vacuum GmbH, Aßlar, Germany), consisting of four stainless steel rods of 200 mm length, a diameter of 8 mm and an interrod radius of 3.54 mm. The rod system is enclosed in a stainless steel casing with an inner diameter of 32 mm. At the end of the quadrupole a faraday cup detector is mounted for ion detection. In case the off-axis SEM (SEM 217, Pfeiffer Vacuum GmbH, Aßlar, Germany) is used for detection, a custom built deflection unit guides the ions towards the SEM conversion dynode until the attraction of the applied voltage to the conversion dynode is strong enough to collect the ions on its own. The SEM dynode

stack consists of 16 discrete dynodes and both detectors can perform in the specified measurement ranges of 1×10^{-12} A to 1×10^{-5} A. Figure 2.2 illustrates the device including the faraday cup, the rod system and the deflection plate as a half section for improved visibility of the inner components.

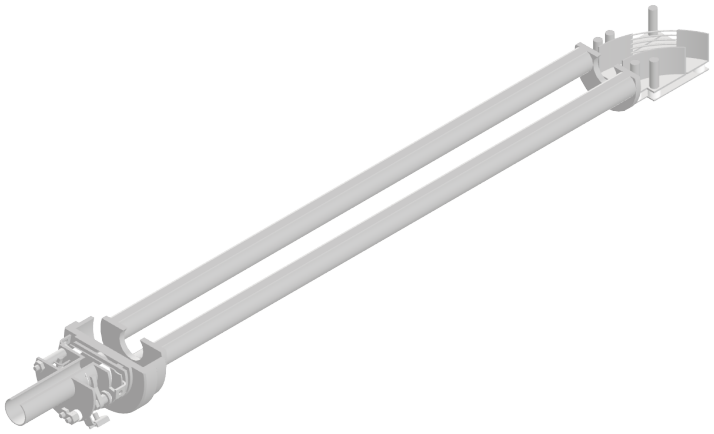

Figure 2.2: Representation of the SPM 700 mass spectrometer including the electron ionization source, the rody system and the deflection unit plus faraday cup

The deflection unit is shown in figure 2.3 with its major two components: The deflection plate as the inner electrode and the faraday cup as the grid and every surface behind the grid, which are not shown for better visibility. Notably the visible grid in figure 2.3 is already part of the faraday detection unit so ions striking the grid will be detected as well as ions hitting a the faraday cup downstream of the grid. The potential of the deflection plate is set relative to the ion reference potential as well and the specified value is -320V.
The RF and DC voltages for the quadrupole rods are provided by a QMH 400-5 RF generator (Pfeiffer Vacuum GmbH, Aßlar, Germany) which supports mass spectral acquisition in the range of $1\,\frac{m}{z}$ to $300\,\frac{m}{z}$. Additionally the QMH 400-5 is processing the signals from both detectors after pre-amplification (EP 422 preamplifiers, Pfeiffer Vacuum GmbH, Aßlar, Germany). The Ep422 has a low specified noise of 2×10^{-13} A. The voltage on the quadrupole rods increases gradually as the scan continues to achieve a mass spectrum. At the beginning of a mass scan starting at $\frac{m}{z} = 0$ the DC potential is 0.5 V and the RF potential

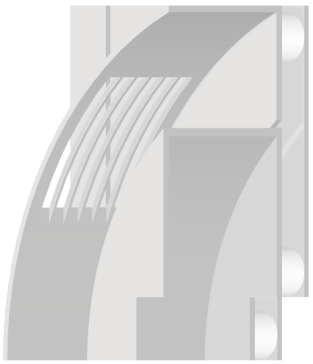

Figure 2.3: Close up of the deflection unit. The inner curved electrode acts as the deflection plate and the grid is the entrance into the faraday cup

is 1.5 V zero to peak. The theoretical limit of the RF generator is 512 $\frac{m}{z}$ which equates to 394 V DC potential and 2350 V zero to peak RF potential. The specifications limit the mass range to $\frac{m}{z}$ = 300 ending the reliable mass scan range at 213 V DC potential and 1378 V zero to peak RF potential.

2.2 SIMION

The SIMION simulation program package (Scientific Instrument Services, Inc., Ringoes, NJ, www.simion.com)[85] utilizes the finite differences method to solve trajectories of charged particles under the influence of electric and magnetic fields. Prior to the simulation the basic geometry is converted into a potential array after the dependency of the used discrete electrodes on each other have been solved by the software. It is possible to assign a specific potential on each surface that was separately converted so the superimposition of several electric fields originating from the different electrodes has to be taken into account. The geometry for the creation of the potential arrays can be imported from a CAD generated .stl file utilizing an internal converter.
The calculation of trajectories is done via the Runge-Kutta method. The interface of the software is written in on Lua[86] which allows the implementation of Lua code to create numerous simulation applications for example variable elec-

tric fields over the course of the simulation. The usage of Lua code also allows importing libraries to include external functionalities for use in SIMION, such as gas collision models.

2.3 SPARTA

The Stochastic Parallel Rarefied-gas Time-accurate Analyzer (SPARTA)[87, 88] is a simulation program based on the Direct Simulation Monte Carlo (DSMC) method. This method allows calculations of trajectories of uncharged gas particles including collisions and surface reactions. The method was developed by Bird[89] and is used in cases that require deiscrete particle interactions to be taken into account and that do not obey assumptions made for continuum flow. For a simulation the program calculates the trajectory of a given particle based on the initial coordinates and the kinetic energy in a three dimensional, two dimensional or two dimensional axi-symmetric space. Based on this input the position of a particle after a certain timestep is specified and the particle moves to the new location. The simulation box is overlayed by a 2D or 3D grid influencing the statistics of particle collisions and allowing distribution onto different CPU cores to reduce calculation time. SPARTA utilizes a statistical model to discern if collisions happen among a given number of particles in a single grid cell and applies a variable hard sphere (VHS)[90] or variable soft sphere (VSS)[91] model for those collisions. SPARTA is designed to calculate high particle numbers on multiple CPU cores at the same time. The allocation of the cores to specific grid cells can be done in several fashions depending on the exact simulation to achieve the highest performance. The geometry for the simulation can be created manually via a set of points and lines in collaboration with a Python script called Pizza.py or transformed from a given CAD .stl file using a Python based converter from .stl in a geometry file readable by SPARTA. It is possible to save data for the particle density in each grid cell or the number of times a specific reaction or a surface collision takes place on each timestep or averaged over a set amount of timesteps for post simulation analysis.

2.4 Molflow

Molflow[92] is a raytracing program designed to calculate trajectories in complex geometries at high vacuum conditions. The underlying algorithm is the test particle Monte Carlo method (TPMC) so one particle represents a larger amount of particles which allows for robust statistics based on few calculated trajectories. As the interaction between particles is not calculated the space between surfaces does not play a major role, which is why the geometry is divided into facets on the surface and not into 3D cells. This reduces computing time drastically and allows for easier parallelization since there is little data communicated between different CPU cores. Particles can be created on each surface facet with a specified desorption rate which is based on calculations assuming ideal gas conditions. Facets can be set to be completely opaque, completely transparent or any value in between those extreme cases to allow transparent pass with a certain probability through a facet. The total count of hits is equivalent to transparent passes on a surface and subsequently enables the calculation of certain quantities such as pressure, impingement rate, particle density, velocity and angular distribution of hits. These variables can then be displayed with a built-in graphical interface on the facet for visualization purposes or on a separate plot.

3 Results and Discussion

3.1 The Baseline Shift

3.1.1 General Description

In corresponce to specific device parameters such as: Ion source pressure, deflection voltage and SEM voltage, the baseline of the RGA instrument rises from the electronic noise of 7×10^{-14} A to, depending on exact conditions, 1×10^{-10} A as illustrated in figure 3.1. This experiment was conducted with hydrogen as carrier gas. In the first segment from 0 s to 10 s the SEM and the filament are turned off so the electronic noise of the device is shown to be at the mentioned level. As the SEM is turned on with a value of -2500 V conversion dynode potential the noise rises to 2×10^{-13} A and the dark count rate of the SEM is visible from the increased amount of spikes in the segment from 10 s to 20 s. When the filament is switched on after 20 s the baseline immediately jumps to 1×10^{-10} A and there are small peaks visible on top of the baseline.

A basic explanation for the demonstrated phenomenon is that there have to be processes involving the filament that directly translates to a detectable current in the SEM without being mass filtered by the installed quadrupole. This mechanism severely hinders the performance of the device by reducing the dynamic range from a maximum of eight orders of magnitude (the detector saturates at 1×10^{-5} A and the electric noise is about 1×10^{-13} A) to about five orders of magnitude. Additionally the shift renders small peaks hard to detect if their intensity is below 1×10^{-10} A. The main goal of this work was to identify the potential causes for this baseline shift and propose concepts to eliminate or at least alleviate the negative consequences of this behavior.

Figure 3.2 demonstrates the effect the baseline shift has on a recorded mass spectrum. It is clearly discernible that the height of those peaks, that are orders of magnitude taller than the baseline (e.g. the hydrogen peak, the water peak,

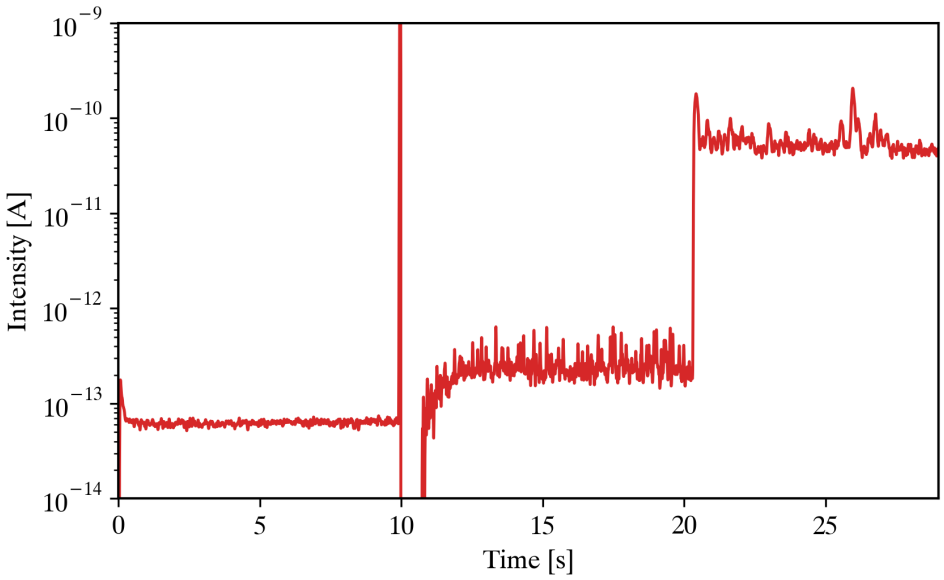

Figure 3.1: Illustration of the baseline shift. In the range from 0 s to 10 s the filament and the SEM are turned off, subsequently the SEM is turned to -2500 V but the filament is still off. After 20 seconds the filament and the SEM are both turned on.

the nitrogen peak) does not significantly change but peaks that are below the elevated baseline level display a notably smaller signal to noise ratio up to the point at which they are not detectable at all. In numerous analytical applications the small peaks are of utmost interest and their signal to noise ratio is generally desired to be as high as possible. The highest peaks usually are suppressed as to reduce the amount of stress on the detector to increase detector lifetimes which implies that the influence of the baseline on the tallest peaks is not as important in many cases.

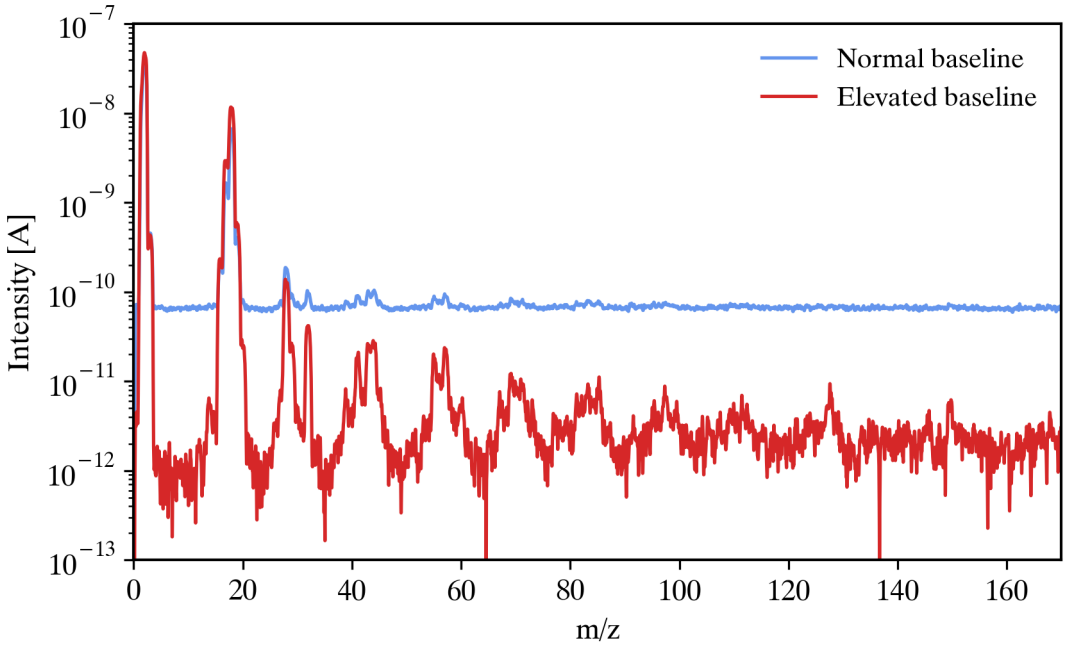

Figure 3.2: Depiction of the influence of the baseline shift on an underlying mass spectrum

Based on this problem there were several hypotheses proposed to explain the phenomenon which significantly influenced the research for this work. These hypotheses are briefly discussed and every corresponding set of experiments for validation or falsification introduces more knowledge to refine subsequent hypothesis-driven investigation.

3.1.2 Ion breakthrough

The initially proposed hypothesis was that generated ions are simply "breaking through" the rod system and reaching the detector unfiltered thus arriving at every m/z and forming a steady baseline over the entire course of a mass scan. The main reason for this hypothesis is the fact that the pressure in the ion source has to be sufficiently high for the phenomenon to occur (more on this issue in section 3.1.5.5). In experiments where the baseline shift was observed for the first time, the pressure inside the ion source was as high as 1×10^{-2} mbar with a pressure in the analyzer region of about 3×10^{-5} mbar. The SPM ion source is

designed for such high pressures such that the filaments can handle elevated inlet pressures of this magnitude. The amount of ions ejected from the ion source is directly proportional to the pressure in the ion source so higher source pressures can have side effects based on the amplified amount of ions. It was speculated that at such high pressures the generated ions can effectively shield each other from the quadrupolar field in the analyzer region via space charge effects. This would subsequently lead to a reduced effect of the electric field emanating from the rod system itself on ions in the radial center of the rod system as the ions solely experience the positive electric field emitted from the cations around it. Therefore the magnitude of the baseline shift is directly influenced by the amount of ions formed in the ion source and transferred into the analyzer region. Also ion source parameters would exert a noteworthy impact on the baseline as they directly influence the amount of ions entering the rod system.

3.1.3 Photons

There are four sources for photons in the utilized QMF: The filament itself, recombination reactions and bremsstrahlung.
The filament is naturally emitting photons (black body radiation). The specific location of the filament outside of the ionization area without a direct line of sight to the detector or even the analyzer region renders this source for photons impossible or at the very least implausible to be the main cause for the shift of the baseline.

Recombination reactions, following reaction R 3.17, can occur in the ion source if the pressure is sufficiently high for collisions between cation and electron to be likely, as in the utilized SPM ion source[93].

$$A^+ + e^- \longrightarrow A + h\nu \qquad \text{(R 3.17)}$$

The rates for these reactions are directly proportional to the concentrations of A^+ and e^- and since the emission current of the filament influences both these parameters it affects the reaction rate significantly. Additionally a higher concentration of A leads to more A^+ so the pressure inside of the ion source should show an effect on top of that. Naturally the rate is not identical for all ions and the kinetic energy of the electron does play role as well.

The majority of ions entering the rod system is filtered out on the rods as the scan progresses. According to the mechanisms mentioned in section 1.5.3 the ion impingement on the metal surface can lead to the ejection of an electron. Since the ions are all positively charged these reactions will take place on rods with a negative potential within that timeframe while the neighboring rods have a positive potential. If an electron is ejected from the negatively charged rod it will experience an acceleration towards the oppositely charged rods with an accelerating force of two times the RF potential the rods carry within this timeframe. The electric field accelerating the generated electron, in most instances, does not exhibit the peak to peak voltage of the RF but rather a continuum between a net 0 difference between the rods and the maximum. However for an analysis of a plausible scenario and to evaluate the minimum wavelength in an edge case scenario the peak to peak voltage will be considered. As the electron experiences the accelerating force and the velocity of the electron is increased it generates a continuum of bremsstrahlung photons with a maximum depending on the initial and end conditions of the electron. This mechanism produces photons inside the analyzer region, which is closer to the detector and thus the trajectories of the photons exhibit a higher tendency to reach the detector compared to photons generated in the ion source. The photons originating from this mechanism should display a dependency on the actual mass scan, because the higher the RF voltage the higher the maximum energy of the electrons and the lower the wavelength of the emitted photons. This is unless at the minimum RF possible the wavelength is already low enough to cause the photoelectric effect at the detector, in which case the effect of the RF on the rate of reactions on the detector would vanish completely.

It is known that excited neutral species are a common product of electron ionization sources. As mentioned in 1.4 these excited states can undero radiative relaxation into the ground state as they emit a photon of the exact energy discrepancy between the excited state and the ground state. The energy of these photons is sufficient to overcome the work function of most metals for excited states of the observed gases[94, 95, 96]. It is possible that an excited species with a high enough energy decays in a radiative relaxation process and emits a photon with a trajectory towards the detector. Since excited neutral

species are not influenced by the electric field of the QMF these decay reactions can happen at any point between the ion source and the detector, depending on the lifetime of the energy state.

These photons can then trigger a response from the detector according to the mechanisms explained in 1.5.1.

3.1.4 Dynamic range of the pre-amplifier

Every amplifier can only handle signals that are within its dynamic range. It is a possibility that, as the most intense peaks increase with the source pressure, the amplifier/acquisition electronics shifts the baseline up in order to keep both the minimum signals and the maximum peaks in its dynamic range. This would explain why the phenomenon only occurs at elevated inlet pressures. This hypothesis demands however that the shift is on a scan-to-scan basis and is dynamically applied depending on the information from the previous scan since the intensity of the highest peak is not known beforehand. A second possibility is that the device performs a quick preliminary scan before the real scan and identifies the range of the highest signal in order to adjust the baseline to keep the whole spectrum in the dynamic range.

In order to test the likelihood of these hypotheses a first set of experiments was conducted to investigate the position of the baseline as selected parameters were changed one by one. These parameters include the bias of the rods, the extraction voltage, the focus lens potential, the deflection plate potential, the emission current, the ion source pressure, the type of gas and the potential on the SEM conversion dynode. All these experiments were done employing the settings shown in table 2.1 unless stated otherwise.

3.1.5 Variation of internal parameters

3.1.5.1 Deflection plate potential variation

As a first parameter to consider the potential applied to the deflection plate turned out to be of utmost importance and every other experiment had to be carried out with the appropriately adjusted potential applied to the deflection

plate to show the desired dependencies. The experiments were carried out with hydrogen as carrier gas at 1×10^{-5} mbar pressure in the analyzer region and with the specified ion source parameters from table 2.1. It was mentioned earlier that the deflection potential is referenced to the "ion reference potential" as an ion source parameter. However it was important to circumvent the limitations of the software in order to adjust the potentials outside the specified range. To achieve this goal the deflection potential was adjusted with an external power supply so the indicated deflection potentials are referenced to ground and not to the ion reference potential. Figure 3.3 illustrates the influence of the deflection potential on the baseline and selected peaks in the range of 150 V to -25 V.

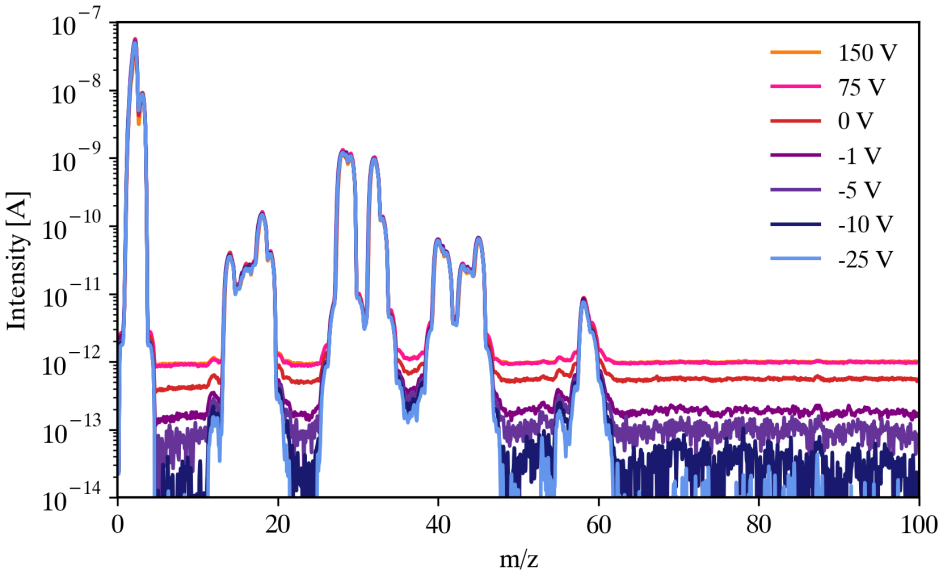

Figure 3.3: Influence of the deflection potential on the mass spectrum using the faraday cup as detector and hydrogen as carrier gas.

It is noteworthy that the applied potentials in the experiment are lower compared to normal usage of the device. However a further decrease of the potential did not indicate any notable difference in the spectrum so the present range of voltages was chosen. It is clearly discernible that the peak height of abundant species is not significantly affected by the applied potential to the deflection plate as in the entire m/z range the peaks are almost indistinguishable from one another. In contrary the baseline is severely affected and declines in

a stepwise manner from 1×10^{-12} A at the highest voltage (+150 V) and almost completely vanishes at -25 V. This different behavior may be caused by the vast differences in magnitudes between the ion peaks and the baseline. A shift from 1×10^{-12} A to 1×10^{-14} A is miniscule compared to the height of the peaks, as they are mostly several orders of magnitude higher. Further evidence of the direct influences on the baseline are needed before a conclusion can be drawn.

However simply judging the baseline it becomes apparent why the deflection plate plays a crucial role in the analysis of the baseline. To get an even better understanding it is necessary to compare these data to a similar experiment conducted with the SEM as seen in figure 3.4 utilizing 1×10^{-5} mbar Argon pressure in the analyzer region with the aforementioned SPM ion source parameters.

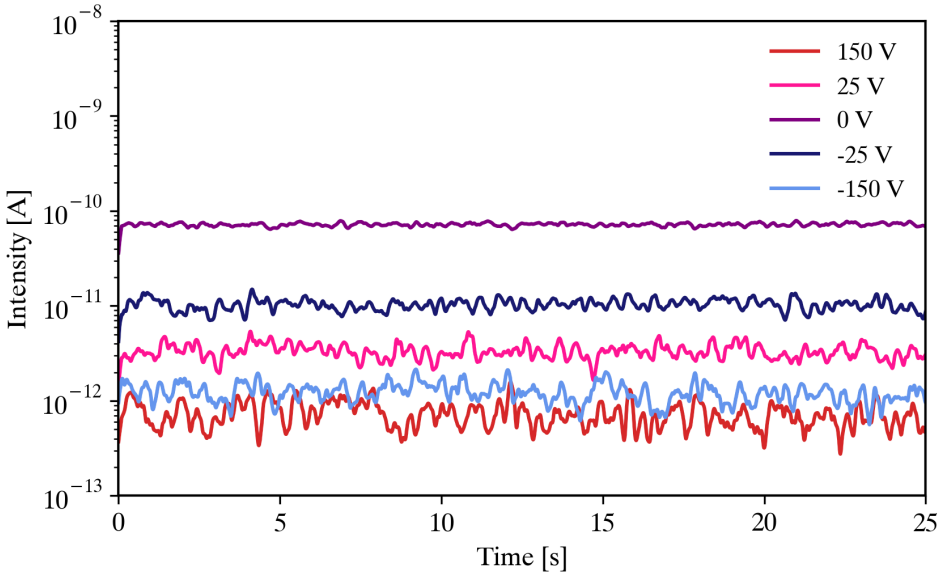

Figure 3.4: Influence of the deflection potential on the baseline using the SEM as detector and Argon as carrier gas.

To reduce stress on the detector a high m/z range was chosen so peaks in the small m/z range are cout ot of the spectrum. In this range no ion species are present and the detector can be operated at high conversion dynode voltages of 2500 V. Contrary to the data taken with the faraday cup, the influence on

the signal the SEM receives does not seem to follow a simple direction. The highest baseline is achieved at the zero potential experiment and from there on the baseline diminishes as the potential increases or decreases. It appears that any potential on the deflection plate impacts the baseline in a negative way, disregarding if it is of positive or negative polarity.

To exhibit the influence in the baseline of the SEM more clearly, the position of the average baseline as a function of the deflection potential is shown in figure 3.5. In this plot it becomes apparent that the applied voltage polarity truly does not play any role as the slope on both sides is alike. These datasets clearly show that the cause for the increased baseline must be of ionic nature in this part of the device, which is a first important piece of information to decipher the nature of the shift of the baseline.

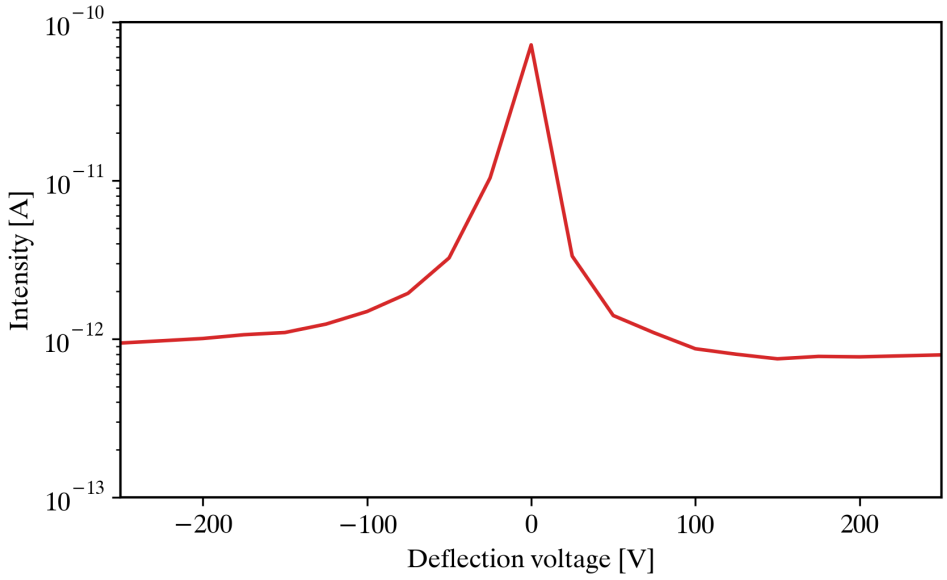

Figure 3.5: The baseline of the SEM as a function of the deflection potential

The significant difference between figure 3.3 and 3.4 indicates that there are different mechanisms operating. While the baseline is at its highest level at the most positive potential for the faraday cup, the SEM exhibits the highest baseline at 0 V. This may be due to the different mechanisms operating at the detector surfaces as discussed in section 1.2.2.

Since the potential of the conversion dynode may have an effect on the ions

in the deflection unit, acting as an attractive force to draw ions away from the faraday detector, experiments were conducted to analyze how notable this effect is. Figure 3.6 depicts the results of these experiments using hydrogen as carrier gas.

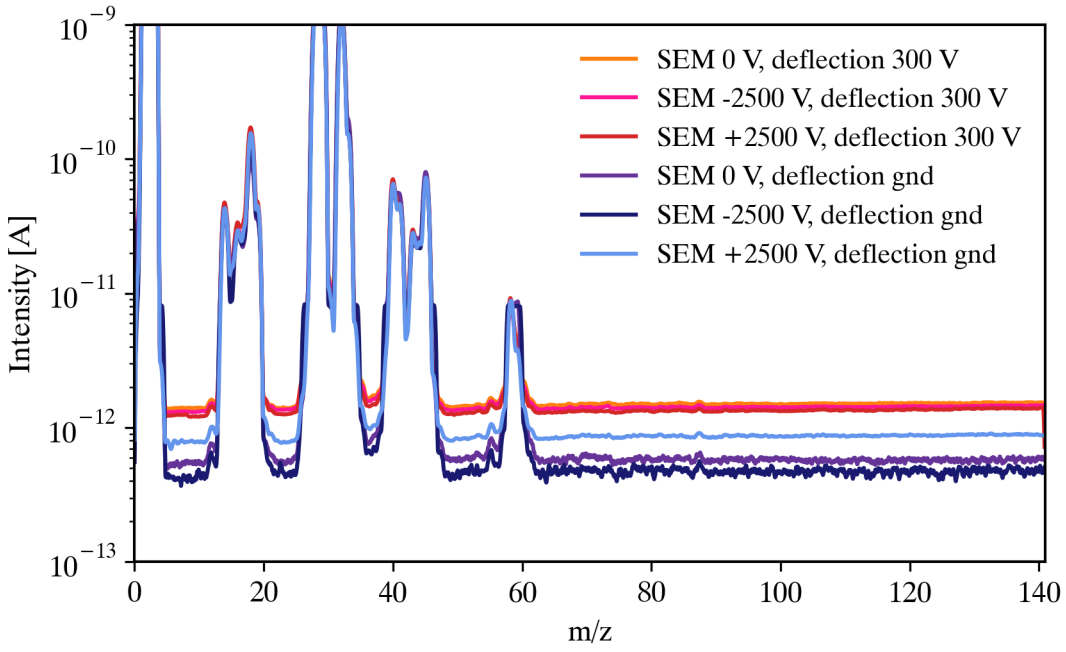

Figure 3.6: The baseline of the faraday at different SEM conversion dynode potentials

The first dataset (red, orange and purple) were done using 300 V deflection voltage because the baseline on the faraday is higher this way and an effect may be easier to note. In contrary to that the second set of data (blue, teal and dark blue) was taken with 0 V deflection voltage in order to see the raw result of the SEM without any auxiliary potential affecting the ions. It is visible that a potential, positive or negative, imposes a greater effect on the baseline of the faraday detector if the deflection voltage is 0, as in this case the conversion dynode is the only attractive force. If the deflection unit is set to 300 V the effect of the SEM is very minscule. In both cases however the baseline does not exhibit a drastic variation. The ion signals are indistinguishable between the experiments, indicating little effect on the ion trajectories as well. This might

be an indicator that the conversion dynode potential does indeed not reach into the deflection unit to a considerable extent or that the ion beam exiting the quadrupole is broad enough that even after being directed towards the SEM it still hits the faraday detector to the same extent.
With the knowledge, that the source for the baseline shift has to be ionic at some point, it is evident that a thorough investigation of applied potentials of the device should be conducted.

3.1.5.2 Focus lens potential

The next parameter investigated is the focus electrode potential. A high positive potential indicates that ions stemming from the ion source experience a repulsive force from this electrode and in turn a positive potential should thus decrease the ion flux into the analyzer region. A negative potential forms the ions exiting the source into a consistent and focused beam. The results for this experiment are shown in figure 3.7.

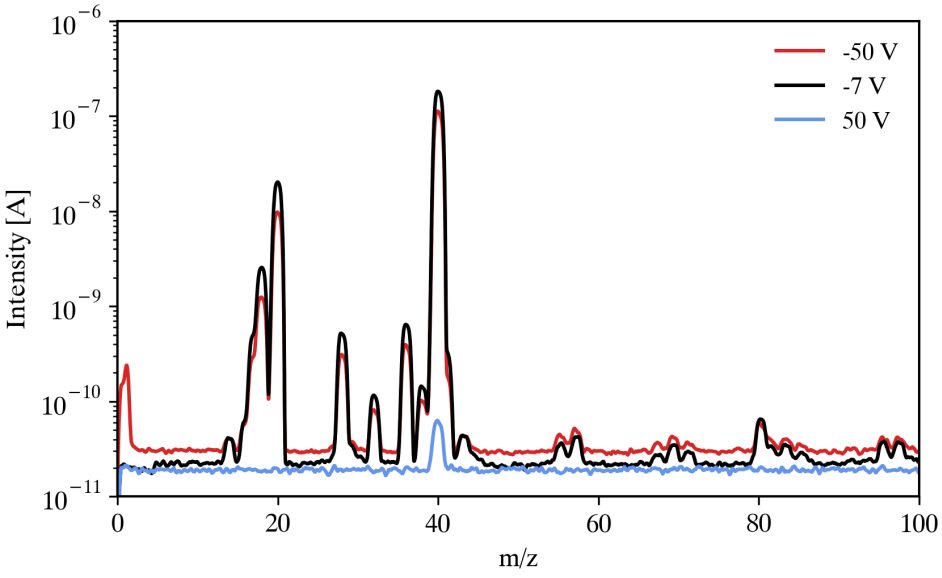

Figure 3.7: The influence of the focus lens potential on the mass spectrum

As expected the difference between -7 V, the standard potential, and -50 V is not exceedingly high. There is a minor influence on ion signals but it is only by a factor of around two. Employing a positive potential of 50 V on the other hand leads to a drastic decrease in the signal intensities of present species. Except for argon, the most intense peak, no other signal is even discernible any more as the remaining sections of the spectrum are flattened to the baseline. The baseline itself only experiences a small decrease and thus exhibits dramatically different behavior compared to ionic species.

3.1.5.3 Field Axis

The field axis potential is the bias of the rod system relative to the ion source region. The potential difference between the ion source and the rod system establishes the kinetic energy of the ions as they traverse the analyzer. Thus if the potential is positive, the ions experience a net positive potential barrier from the rod system and will effectively be hindered from entering.

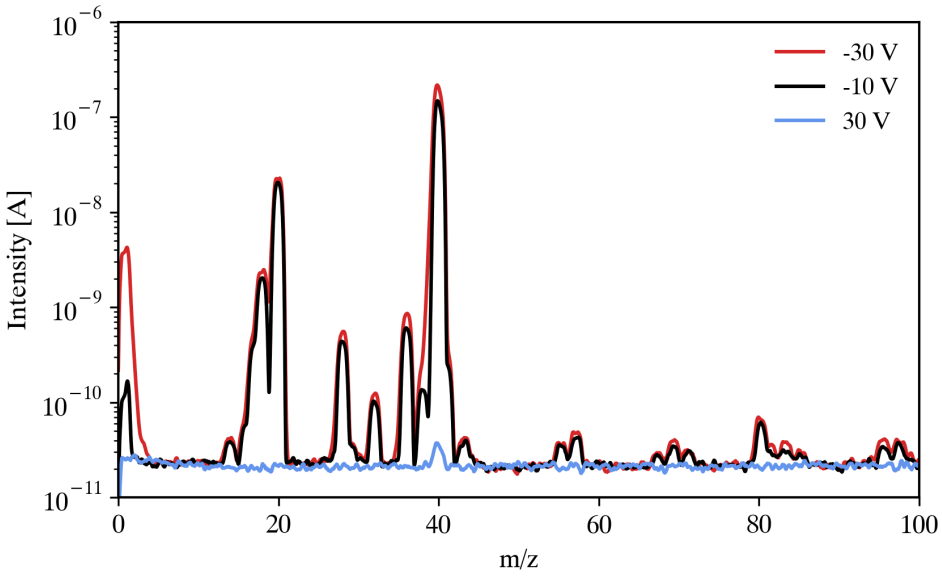

Figure 3.8: The influence of the field axis potential on the mass spectrum

A high negative potential leads to very fast ions in the analyzer, which reduces mass resolution. Figure 3.8 highlights the results of this experiment. At -30 V the peaks are slightly broader as compared to the standard -10 V setting and a

taller peak is visible at the beginning of the spectrum. This might be caused by the mentioned zero blast which is more intense as ions enter the quadrupole at higher velocities. As the potential is set to a positive value, only an insignificant amount of ions reaches the detector at all and only argon is represented in the mass spectrum. Comparable to the focus lens potential variation, the baseline is not affected by the large difference in the field axis potential which suggests a non-ionic source for the baseline shift at this stage of the device.

3.1.5.4 Emission current

The emission current is measured to be the electric current between the filament as the cathode and the ionization volume as the anode. It is directly proportional to the electron influx into the ionization area and thus influences the amount of generated ions.

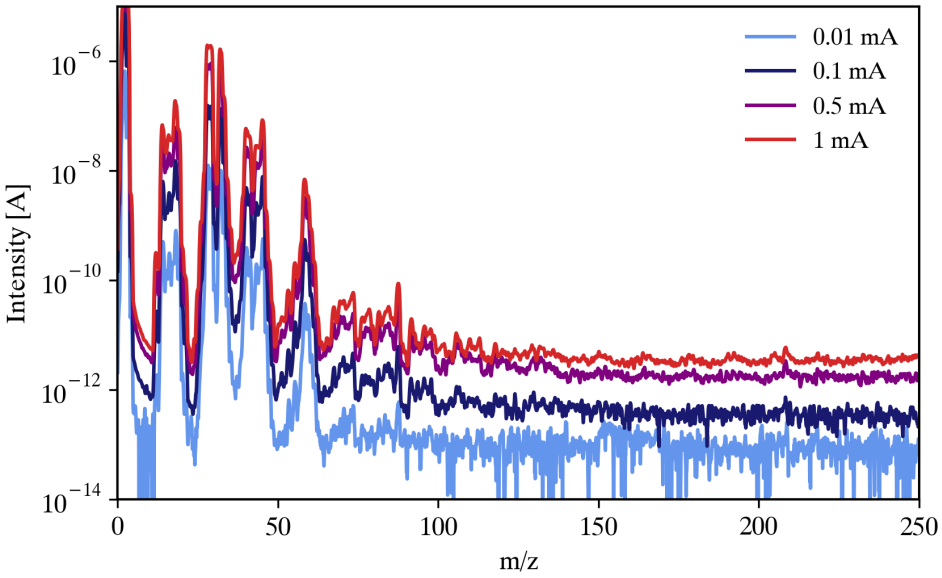

Figure 3.9: The influence of the emission current on the mass spectrum

The results of this experiment are presented in figure 3.9. As apparent from the data, the emission current influences the signals of the present species drastically, as a lower value naturally leads to fewer ions. However contrary to the previous data the baseline is directly impacted by the variation of the emission current. This is a proof that the source for the baseline has to stem from in ion source.

It is possible that the cause for the baseline shift is directly proportional to the amount of electrons in the ion source or the amount of created ions.

3.1.5.5 Pressure

The pressure in the device could not be directly measured at every location. As a consequence only the analyzer pressure reading was available for variation, however since analyzer and ionizer pressure are directly linked to each other, the variation of one translates into a variation of the other.

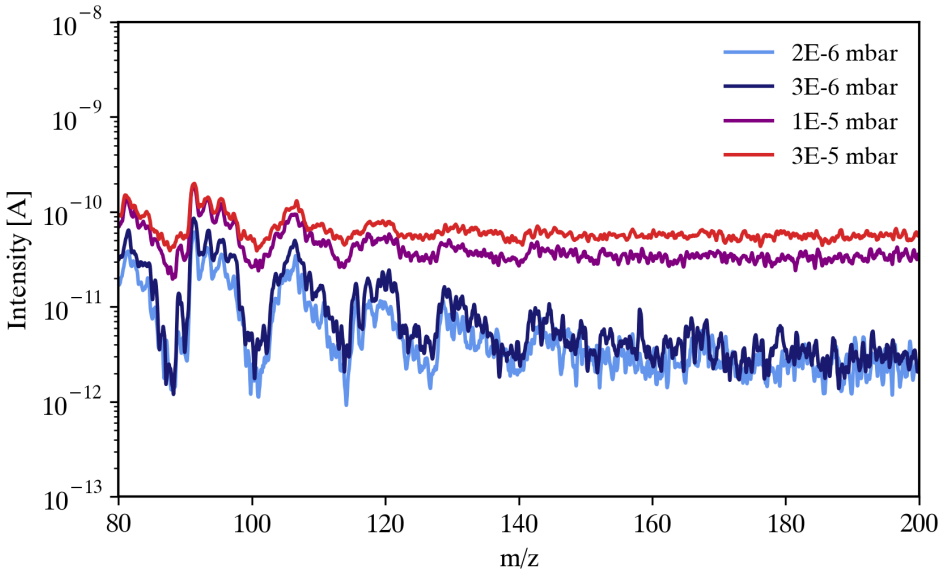

Figure 3.10: The influence of the pressure on the mass spectrum

Additionally the pressure could only be varied in a rather limited range due to restrictions of the pumping system on the lower end and concerns for filament integrity on the higher end. The effect of the variation of the pressure is shown in figure 3.10. Several hydrocarbon signals are discernible in the mass spectrum which become less pronounced as the baseline rises owing to the declining signal to noise ratio. It appears as if the intensity of the hydrocarbon peaks increased but that this owing to the fact that the signals are added onto the baseline and thus rise along with the baseline without gaining intensity themselves. The pressure does show an impact on the baseline so the underlying cause is linked to the amount of present particles at any given location of the device.

3.1.5.6 SEM conversion dynode potential

The potential applied to the conversion dynode of the installed SEM 217 does also affect the potential difference between the discrete stages of the SEM dynode cascade.

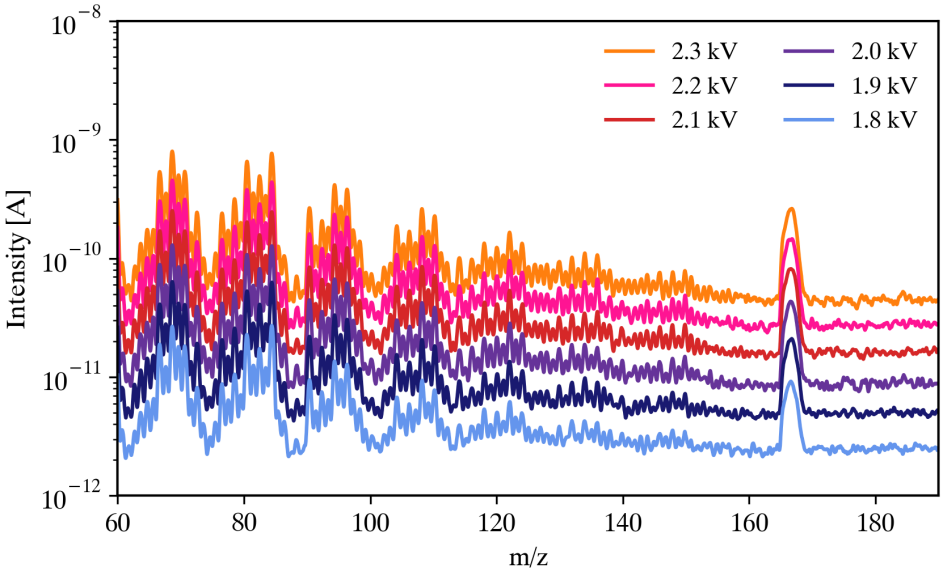

Figure 3.11: The influence of the SEM potential on the mass spectrum

As a result not only the attractive potential for cations onto the SEM is influenced by this variation but also the gain of the SEM, since more and more electrons are emitted on each dynode. The effect of the variation of this voltage is shown in figure 3.11. Apparently every visible signal in the mass spectrum is affected by the potential on the conversion dynode. The hydrocarbon background, including the highest peak stemming from the chemical history of the device, rises linearly in accordance with the baseline. This is expected behavior, given the fact that every signal received on the conversion dynode is amplified by this potential. This indicates however that the mechanism for the baseline is of similar nature as the mechanism for mass filtered ions on the SEM.

3.1.5.7 Extraction voltage

Finally the extraction voltage was varied to evaluate its effect on the baseline. A negative potential on the extraction electrode in reference to the ionization area potential leads to an elevation of both the ion signals and the baseline.

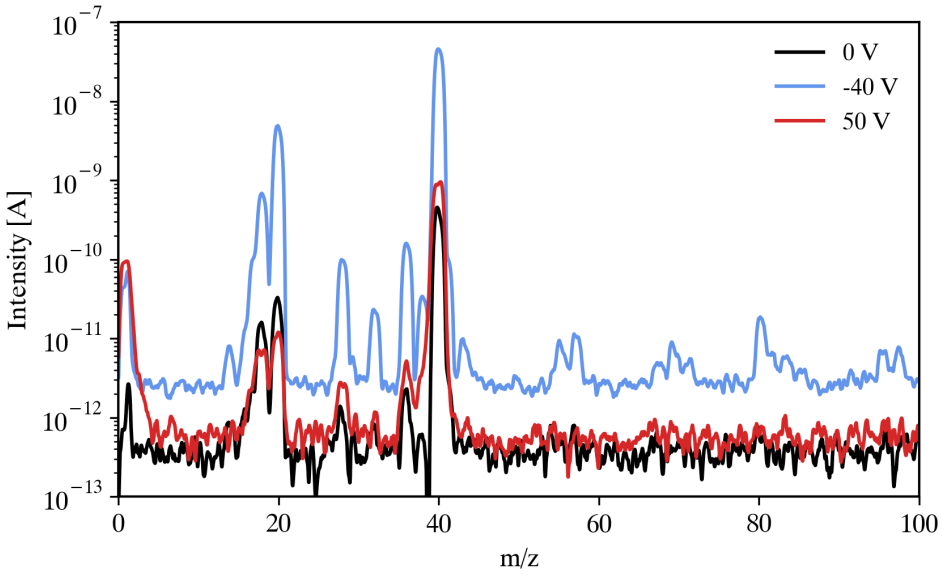

Figure 3.12: The influence of the extraction voltage on the mass spectrum

However it does not matter if the potential is zero or positive as both settings lead to the same result. Comparing figures 3.7, 3.8, 3.9 and 3.12 it becomes apparent that of the EI source parameters only the emission current and the extraction voltage do have an influence on the baseline position. Experiments with other potential variations already show the non-ionic character of the cause of the baseline shift while the emission current variation suggests that the cause is definitely stemming from the ion source. Combining this information with the variation of the extraction potential leads to the conclusion that the extraction potential directly affects the interaction between neutral gas particles and electrons from the filament. In the case of a negative potential the ions are actively extracted from the ion source and the space charge effects in the ionization area are suppressed as the ion population is low. If there is no attractive potential present, the ions are accumulated inside the ionization volume due to its closed geometry. This can affect the trajectories of incoming electrons from the filament

and thus negatively influence the ionization efficiency.

3.1.5.8 Rod system potentials

As the next logical step the potential on the rod system of the QMF was varied. Since the real applied RF and DC potentials are set in the software and cannot freely be changed the plugs to apply those potentials to the rods were removed to run an experiment with no potential on the rods. If the rods are not externally grounded they are floating on the equilibrium potential they achieve as cations react on the steel surface. In this mode the potential on the rods is not controlled and not measured; thus they float.

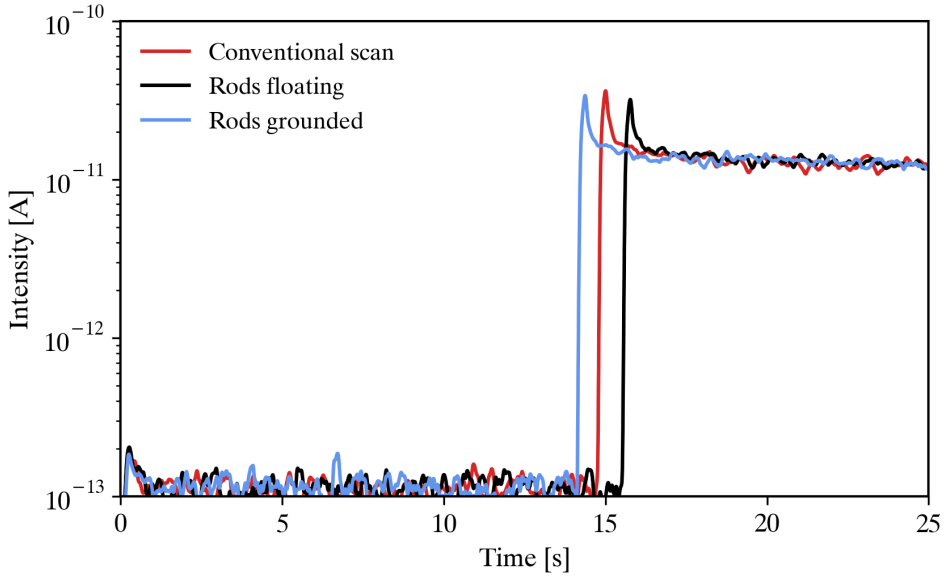

Figure 3.13: The influence of the potentials on the rod system on the baseline

The graphs are separated in 2 sections before and after around 15 seconds. In the first section the filament is turned off in order to detect differences in the electronic noise in different RGA modes. After the filament is turned on, indicated by the steep rise of the signal, the baseline of the experiment is observed.

The conventional scan (red curve), applying the standard RF and DC potentials the software dictates as the scan progresses, shows the electronic noise floor at around 1×10^{-13} A, similar to the observed noise in other

experiments, and a baseline shift of about 2 orders of magnitude when the filament is turned on. In comparison with the conventional scan mode, the experiment using grounded rods (blue curve) and the floating rods (black curve) exhibit the exact same electronic noise floor and the exact same baseline position. The plots are indistinguishable apart of the exact timing of the slope.

This clearly shows that the potential on the rod system has no effect whatsoever on the baseline position and is another strong argument that the source for the baseline signal is not of ionic nature, as it traverses straight through the QMF.

3.1.5.9 Type of gas

Experiments were conducted regarding the extent of the baseline shift for nitrogen, helium, argon and hydrogen under comparable conditions, using -2.5 kV conversion dynode potential and an analyzer pressure of 2×10^{-5} mbar. If the cause for the baseline shift was purely rooted in the electronics of the device a change in gas type should have little to no effect. It is apparent from the data in figure 3.14 that the RGA exhibits a more pronounced baseline shift when hydrogen or argon are the carrier gas as compared to nitrogen, with helium being in between. The noise floor of the system is at around 1×10^{-13} A. This leads to the conclusion that the molecular characteristics of the type of gas has to be taken into consideratation and an electronic root causing for the baseline shift is unlikely. However no gas was found that does not lead to such a shift.

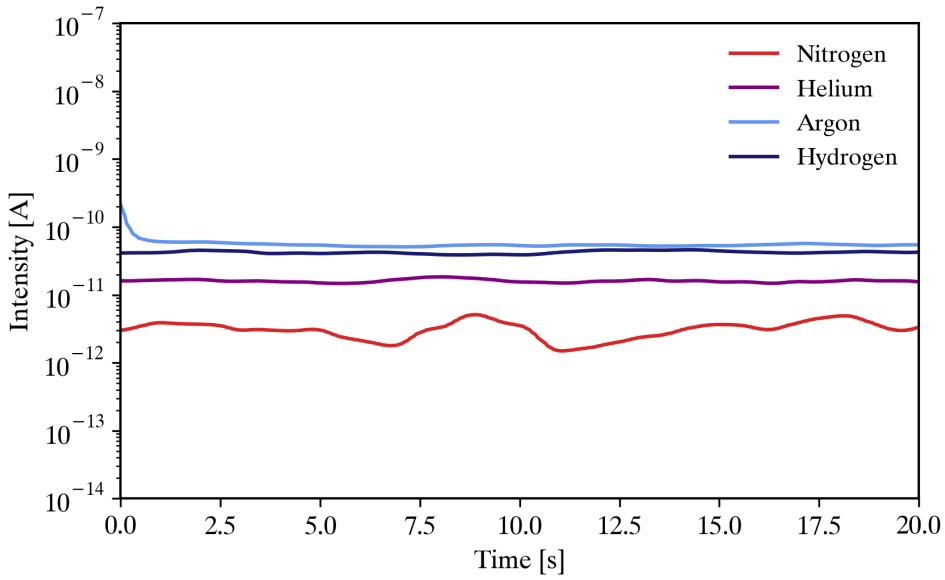

Figure 3.14: Baselineshift for hydrogen, argon, helium and nitrogen using comparable setups

3.1.6 Complementary SIMION simulations

SIMION simulations were performed to support the above results and interpretations. For these simulations the geometry of the ion source and the rod system were extracted from a CAD file of the system and the following simulation parameters were used unless stated otherwise.

Table 3.1: Settings for the SIMION simulations

Ion mass	50 Da
Ion charge	+1
Ion Reference	150 V
Focus	-7 V
Field Axis	-10 V
Entrance Plate	-150 V
RF frequency	2.25 MHz

All voltages are in reference to the ion reference potential. The AC and DC potentials on the rod system were optimized for transmission of m/z50. Figure

3.15 displays the intended settings for the ion source and the rod system and the successful transmission through the quadrupole region of the desired species. Ions are generated in the ionization area and are subsequently extracted by the extraction plate. The ion beam is then focused in the focus lens and enters the QMF via the entrance plate. The experiments did show that the cause for the baseline shift is non-ionic in nature at this stage of the device. Since SIMION only simulates charged particles these results support only the assumptions towards the ion signals and not on the baseline itself.

In figure 3.16 the ion trajectories are depicted for cases where a certain potential is set to a positive value, indicating a higher potential compared to ion reference. It is apparent that the ions are effectively stopped right in front of the positive electrode. This behavior is observed in the figures 3.16b, 3.16c and 3.16d however figure 3.16a indicates that the extraction plate influences the ions in the ionization area and thus supports the speculation that space charge effects might hinder electron-neutral reactions if ions are allowed to accumulate. Since none of the other electrode potentials penetrate the ionization area and the extraction plate is the only one to influence the baseline in the experiments the combination of the experiments and the simulations strongly suggest that the source for the baseline shift is i) stemming from the ionization area of the SPM700 source and ii) is not of ionic nature.

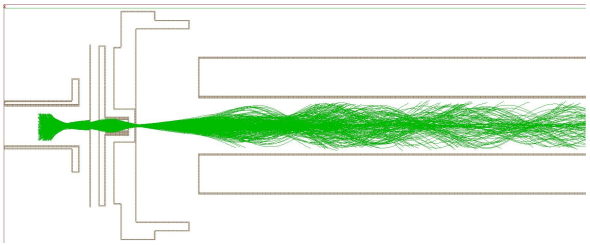

Figure 3.15: Ion trajectories from the SPM 700 EI source at standard settings

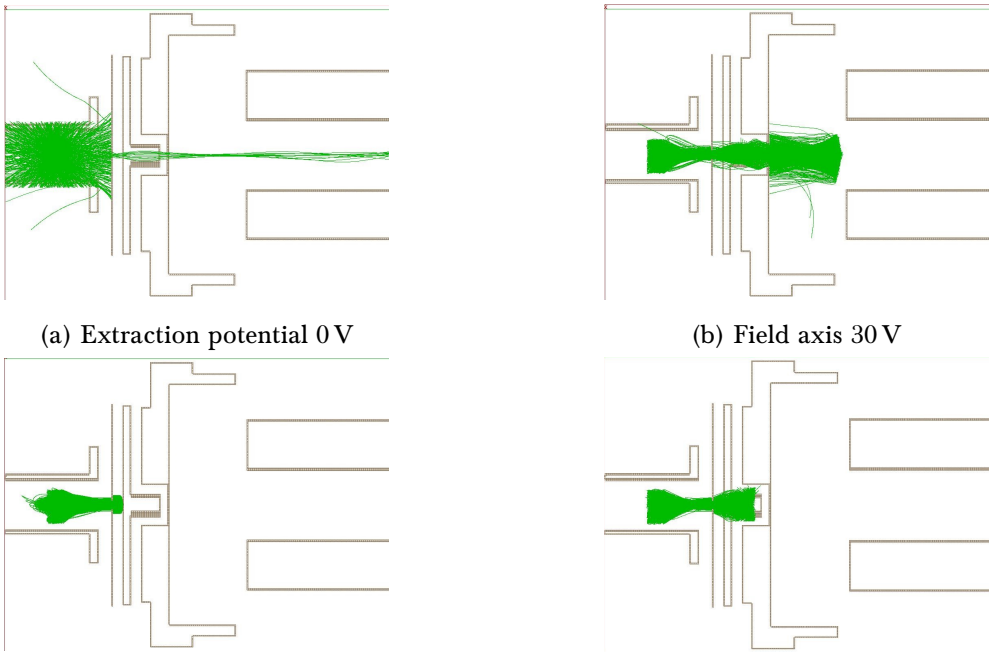

(a) Extraction potential 0 V

(b) Field axis 30 V

(c) Focus potential 50 V

(d) Entrance plate potential 200 V

Figure 3.16: The influence of non-optimal potentials on ion trajectories

Additional simulations were done on the ion trajectories within the rod system to gain a better understanding of interactions in this stage of the device and to get more data to narrow the mentioned hypotheses range down. The simulations were done with the same model as above; hydrogen was used as background gas. In order to simulate space charge effects while keeping particle count low, the SIMION software allows to artificially increase the charge of each ion for simulations of space charge effects. This does not increase the charge for trajectory calculations and is purely applied for space charge effects.

Figure 3.17 shows the trajectories of hydrogen ions with no background pressure and a space charge factor of 1000. The potentials on the quadrupole rods are set to m/z50 and it is visible that virtually all ions are filtered out in the first few cm of the rod system. Almost all ions exit the ion source apertures as intended but are naturally filtered out in the QMF. This simulation suggests that it is impossible for an unstable ion to traverse the rod system unfiltered. This might not be the case for ions very close to the stable m/z but since the baseline is present over the whole course of a mass scan, a low resolution of the quadrupole cannot be

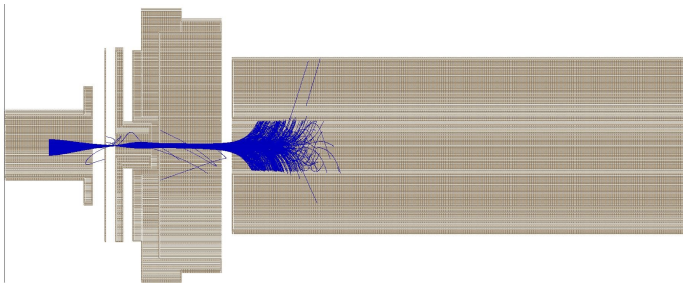

Figure 3.17: Hydrogen ion trajectories entering a QMF with no background pressure

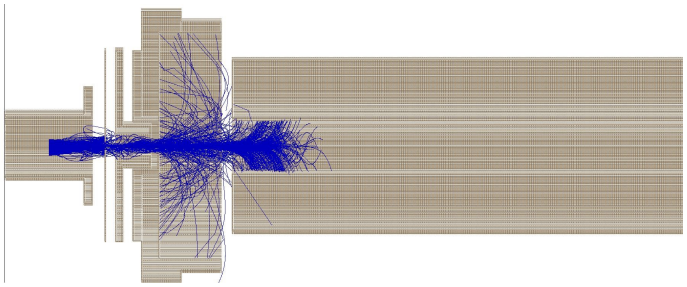

Figure 3.18: Hydrogen ion trajectories entering a QMF with 1 Pa hydrogen background pressure

the cause of the baseline shift.

Figure 3.18 shows the same simulation with 1 Pa background pressure. The amount of ions entering the filter is even lower and thus it is even more unlikely that any unstable ion reaches the detector. This is the consequence of collisions reducing the axial velocity of the hydrogen ions and in turn increasing the influence of repulsive electric fields. As a next step it has to be considered that ions may be formed inside of the QMF via gas phase reactions or photoionization.

Figure 3.19 shows the simulation of a scenario in which the quadrupole potentials are set to transfer m/z50. There are two ion populations created in the ion source. Dark blue trajectories belong to ions of m/z50 while light blue indicates hydrogen ions. Additionally at two different spots in the rod system hydrogen ions are created with 1-4 eV in the z-direction, axially to the rod system. These two ion populations are immediately filtered out as they do not possess enough kinetic energy to withstand the quadrupolar field. In the experiment the baseline is still present at m/z300, when the conditions inside of

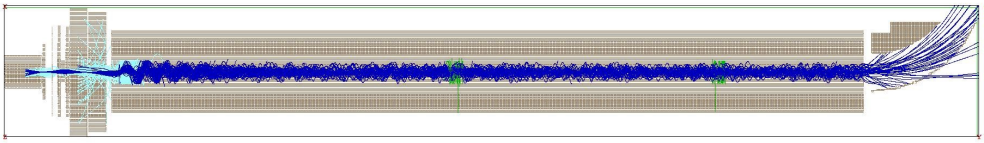

Figure 3.19: Ion trajectories of m/z50 (dark blue), hydrogen from the ion source (light blue) and hydrogen formed inside the QMF (green)

the QMF are even more drastic and the chances for any hydrogen ion traversing the device unfiltered is negligible.

To support the aforementioned experiment regarding the deflection voltage, simulations were performed in which the deflection voltage was varied and the trajectories of ions exiting the quadrupolar field were investigated. Actually implementing the real potential of the conversion dynode proved to be difficult as the conversion dynode is covered by a grid, which is set to the specified SEM potential as well and acts as an attractive electrode before the conversion dynode: The resolution of the simulations was not sufficient to realistically simulate this grid surface. Additionally the exact distance between the SEM and the deflection unit is not documented and difficult to measure due to the tightly enclosed vacuum system design. The effect of the deflection potential however should give an idea on how any potentials in this section of the device affect the ion trajectories.

Figures 3.20 and 3.21 show the simulated trajectories and the respective applied deflection voltage for two different ion mass to charge ratios. The figures show that for a wide range of voltages the ions still hit the surface of the faraday cup and are not directed to the SEM successfully. This explains why the ion signals in figure 3.3 are not significantly affected by the deflection voltage. This effect is even more pronounced for heavier ions as they require more external force to change their trajectory compared to lighter ions. Assuming these simulations are

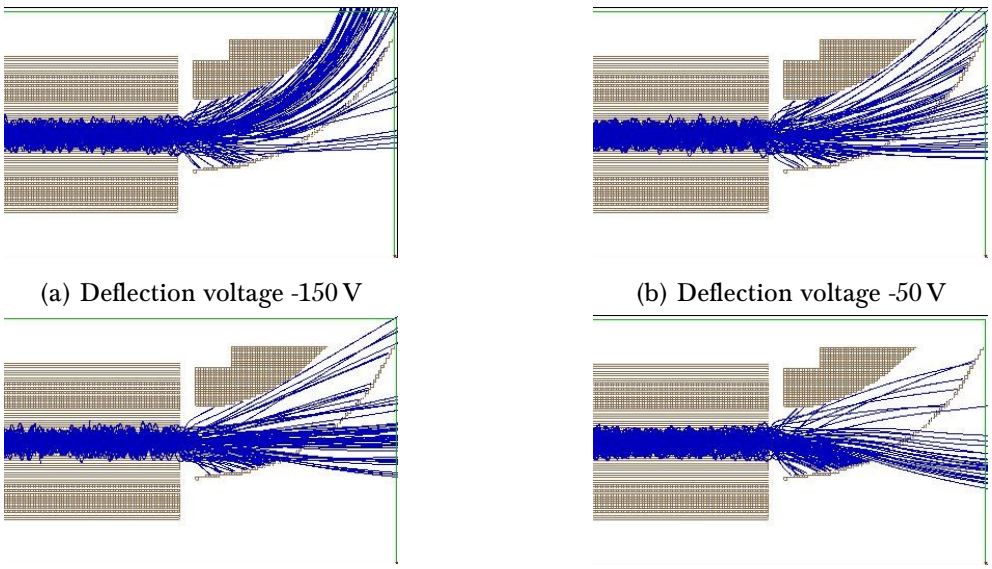

(a) Deflection voltage -150 V

(b) Deflection voltage -50 V

(c) Deflection voltage 0 V

(d) Deflection voltage +50 V

Figure 3.20: Ion trajectories in the deflection unit for m/z150

representative, the assumption that the ion beam downstream of the quadrupole system is broad enough to interact with the faraday cup regardless of a slightly bent shape appears to be reasonable.

3.1.7 Conclusion of the initial set of experiments

To summarize this set of experiments and simulations the following conclusions are drawn:

- Higher emission currents and higher source pressures both elevate the baseline
- Of all the potentials from the ion source only the extraction voltage influences the baseline
- The baseline is higher for larger SEM conversion dynode potentials
- Hydrogen and argon lead to a larger shift compared to helium and nitrogen, however all gases result in a shift
- The RF and DC potentials of the rod system show no influence on the baseline

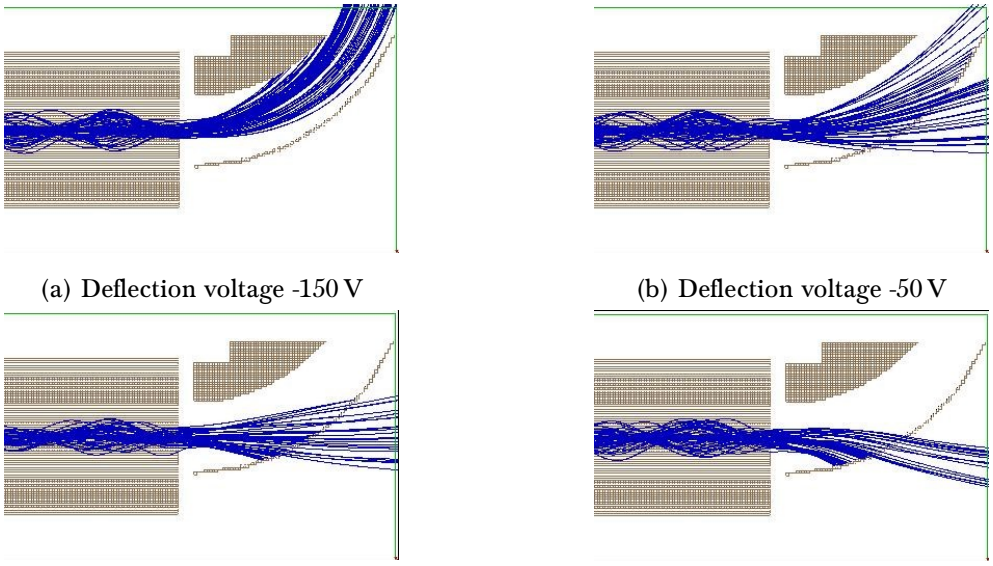

(a) Deflection voltage -150 V

(b) Deflection voltage -50 V

(c) Deflection voltage 0 V

(d) Deflection voltage +50 V

Figure 3.21: Ion trajectories in the deflection unit for m/z2

- The cause for the baseline shift has to stem from the ion source
- The source for the baseline shift has to be of neutral nature in the ion source and the rod system but ionic in the deflection unit
- The maximum baseline shift using the faraday cup as detector is pbserved when the deflection potential is large and positive
- At the SEM the baseline shift is at its maximum at 0 V deflection voltage
- The potential on the SEM conversion dynode does not significantly influence the baseline when using the faraday cup as detector

Returning to the initially proposed hypotheses some of them were falsified and some new were proposed to rationalize the results of the experiments and simulations.

3.1.7.1 Ion Breakthrough

Ions of the background gas are the most abundant species; it may appear possible that some of them reach the detector unfiltered. However, experiments varying the ion source potentials showed that the cause for the baseline shift

is not of ionic nature upstream of the mass analyzer. As additional evidence, the baseline is at a fixed value for the entire mass range without any sign of dependency on the rising quadrupolar potential. Experiments with different potentials on the rods point in the same direction and simulations provide more evidence that ionswith unstable trajectories cannot reach the detector. Thus this hypothesis is ruled out.

3.1.7.2 Photons

As already mentioned there are several sources for photons. Bremsstrahlung can be ruled out as well as well since there is no bremsstrahlung present if there is no potential applied to the rods to create electrons and subsequently accelerate them. Radiative decay downstream of the ion source is possible, however unlikely to be the main cause for the shift as the probability of a trajectory towards the detectot is rather unlikely. The photons originating directly from the filament or from recombination reactions inside the ionization area might still be an issue in addition to photoionization after the rod region. This may cause a baseline shift so photons can still provide a valid explanation.

3.1.7.3 Dynamic range of the pre-amplifier

The present results indicate a steep shift of the baseline as soon as the filament is turned on even though the mass spectrum is devoid of any other signal. This rules out this hypothesis as the increase is immediate and the software does not complete the scan to adjust the baseline afterwards. Even if it acted this way, in the absence of an intense signal that would be located outside of the dynamic range, there was no trigger to electronically adjust the baseline by the acquisition system.

3.1.7.4 Excited states

Given the evidence that the source for the baseline shift is neutral in nature in the ion source and the rod system while being ionized at some point between analyzer exit and detector, long lived excited states of the carrier gas can explain every observation so far. Experiments, simulations and calculations need to be performed to rationalize how the ionization takes place and what kind of states, and transitions and processes are reasonable.

Having ruled out several hypotheses, the main focus of the work addresses photons and their interactions with neutrals and metal surfaces as well as excited species and their interactions with each other, metal surfaces, photons, neutral molecules and atoms.

3.2 Photons and Excited species

3.2.1 Summary and explanation of the narrowed focus

Before focusing on the experiments it is important to illustrate how photons and excited species may lead to an elevation of the baseline.
In general what needs to happen to induce a signal on the detector israther straight forward: An electron has to leave the metal lattice. In the case of the faraday cup this lost negative charge will be replaced by the electronic circuitry and the resulting current is detected while for the SEM the electron leads to an avalanche of electrons which ultimately leads to a signal on the detector plate at the end of the stack. As mentioned in section 1.5, a myriad of possible reactions exist to release an electron from the metal lattice. To present an overview of those reactions, figure 3.22 displays the possible pathways leading to a signal on the detector.

3.2.1.1 Remaining hypotheses regarding photons

Photons generated in the ionization volume interact with metal surfaces according to the mechanisms discussed in section 1.5; an electron is released in the process. In this device the photons may stem from four sources. Heat radiation directly from the filament might find its way towards the detector either via a direct trajectory or after a few reflections on metal surfaces. The same way bremsstrahlung emitted from electron impacts after being accelerated in the electric field of the rod system can induce a signal. As the ion source produces ions and excited atoms and molecules these excited states can undergo radiative transitions and thus lead to photons at any point of the device. Additionally photons can be produced via recombination reactions within the ionization source.

Out of these mechanisms bremsstrahlung has been ruled out experimentally while heat radiation from the filament cannot emit photons of sufficient energy to overcome the work function of most metals. Given the fact that most metals have a work function of around 5 eV [27] and tungsten filaments only give off a spectrum down to 310 nm or 4 eV [97]. However it is possible for an excited atom or molecule to end up in close proximity to the detector

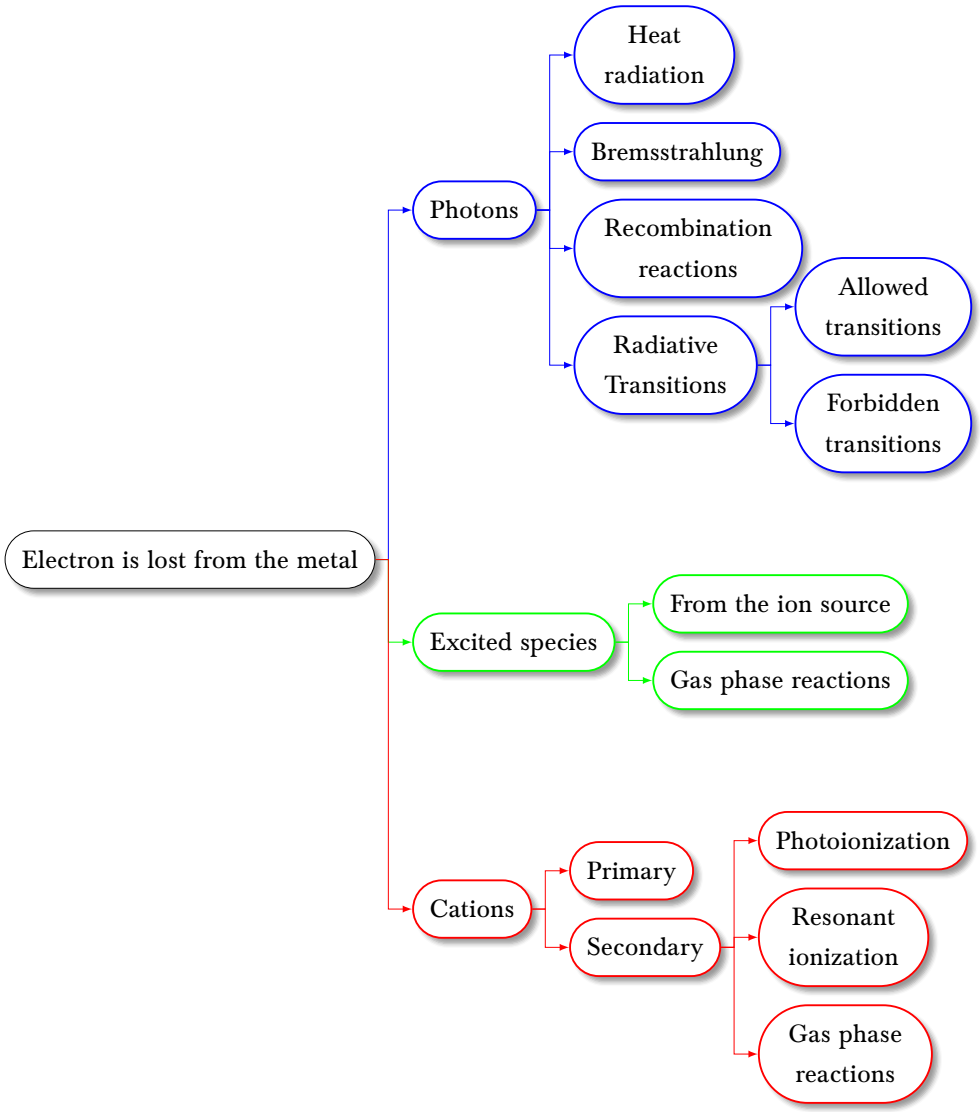

Figure 3.22: Schematic of every mechanism leading to a signal on the detector

during its lifetime and subsequently emit radiation after relaxation to the ground state or a lower state in general. A work function of 5 eV is below the energy level of several electronically excited atomic or molecular states, so this mechanism is realistic and might be an explanation at this point. Assuming a Maxwell-Boltzmann distribution, it is possible to calculate the mean velocity of neutral species exiting the ion source at an assumed temperature of 500 K, given the fact that the ionization source is heated up as a result of the filament

current. A hydrogen atom possesses a mean velocity of around $3200\,\frac{\mathrm{m}}{\mathrm{s}}$ or $3.2\,\frac{\mathrm{mm}}{\mu\mathrm{s}}$ and the employed rod system is 0.2 m or 200 mm long. Combining these two numbers the mean time a hydrogen atom needs to traverse the minimum distance between the ionization source and the deflection unit is $66\,\mu$s. The lifetime of the most common excited states of hydrogen is below $0.1\,\mu$s[48] so more than 60 lifetimes would pass in that timeframe. Other gases might populate excited states with longer lifetimes but they are also heavier compared to hydrogen and thus move significantly slower. Admittedly the calculated velocity is a very rough estimate and only the mean velocity is taken into account while atoms with much higher velocities exist, however they are also a lot fewer in number.

Combining these arguments it appears unlikely that allowed transitions significantly contribute to a baseline shift given the small amount of very fast electronically excited atoms or molecules that can travel far enough before decaying. The probability that the photon is emitted in a trajectory that can reach the detector surface considering lifetimes before relaxation occurs, is extremely low. Forbidden transitions however take place after much longer timeframes. These can be up to several minutes before decaying, depending on the exact state[49, 33] and collision number. As a result the atoms or molecules in question do not have to travel extremely fast in order to reach the needed position in the device before the emitted photon might hit the detector.

However it has been shown that the baseline shift depends heavily on the potential of the deflection unit so photons can not be the main origin for the elevation of the baseline. They may still be the cause for a minor shift, as there are surely several mechanisms at work though.

3.2.1.2 Remaining hypotheses about excited species

Direct interaction of an excited molecule or atom with the detector surface can lead to a signal following the mechanisms discussed in section 1.5.4. Two possible pathways exist for excited species to occur in the present system. Interaction of electrons in the ionization source with neutral gas can excite the neutral into an excited state that can be ionic or non-ionic in nature. This way the ion source always creates both ions and excited neutrals with varying ratios depending on the exact states in question and the electron energy. Using Argon and the $^1S_5$

and $^1S_3$ states as the most likely metastable states as examples the rate between ionization and excitation into those states can be calculated as $\frac{\text{Ions}}{\text{Metastables}} = \frac{28}{1}$ for 70 eV electrons according to equation (1.36) using the respective cross sections[46]. This suggests that a considerable amount of metastable species is produced in the ionization source, which then can traverse the rod system unfiltered and ionize subsequently in a fitting mechanism. These ions can then induce a signal on the detector. So far no experimental or simulation result contradicts this hypothesis..
As seen in reaction R 3.15 the energy of the metastable state can be transferred onto a neutral particle of the same species. This way collisions between metastable atoms or molecules with ground level background gas of the same compound do not intrinsically result in the relaxation of the excited species but rather the propagation of the energy to another particle that then can hit the detector. The background gas is the most abundant species in the mixture so these collisions are the most likely for metastable species. However, experiments varying the deflection voltage provided an irrefutable proof that the source for the baseline shift must be ionic in nature. Direct reactions of metastable species with the faraday or the SEM thus can not be the predominant pathway but remain a possible minor source.

3.2.1.3 Remaining hypotheses about secondary ions

The reaction of a cation with the detector is the desired process in a mass spectrometer and naturally the most realistic one since ions are actively guided towards the detector. However for the baseline shift to occur primary ions, stemming directly from the EI source, were experimentally ruled out. The results of several experiments clearly suggest the ionic nature of the source for the baseline shift, so secondary ions seem to be the most likely origin. However the mechanism to achieve those secondary ions remains unclear. Photoionization caused by photons from the ion source is not impossible but unlikely given the low pressure in the rod region of about 1×10^{-5} mbar and the fact that the energy of those photons is only sufficient to ionize excited species on an energy level of about 4 eV below the ionization threshold. To add to this argument the reactions would need to occur in the deflection unit over the length of about 3 cm but not in the analyzer region. So this pathway cannot

be ruled out completely even though it is rather improbable.
Resonant ionization, the mechanism during which an excited species is ionized at a metal surface, can take place on the faraday cup axially to the ion beam. The trajectory of a neutral metastable particle exiting the ion source and successfully traversing the QMF directly leads towards the faraday cup and a collision with the metal is inevitable. The ion produced this way will then be influenced by the applied potential on the SEM and the deflection plate so this mechanism explains each result in this set of experiments thus far.
The only gas phase reaction to lead to an ion is the one between two excited species. As already mentioned the particle density of excited species in the limited volume of the deflection unit is too low to realistically expect gas phase reactions to occur on the scale needed to explain the baseline shift.

In summary: Photoreactions and direct interaction of metastables with the faraday cup and the SEM can only explain a small fraction of the baseline shift; secondary ions seem to be the main reason why this phenomenon occurs.

In the next set of experiments the main focus is on photons and metastables to find out the mechanism causing the production of secondary ions and to prove that photons do not interact with the detector to any significant extent.

3.2.2 Theoretical calculations and simulations

3.2.2.1 Preliminary calculations

Theoretical calculations can help to exclude certain hypotheses since there has to be a sufficient number of metastable particles present in the device leading to a baseline shift of the observed magnitude. Given the fact that the current on the faraday cup is solely electronically amplified it can be directly translated into the exact amount of charges with equation (3.1).

$$N_e = I \cdot e \tag{3.1}$$

A realistic level of the elevated baseline on the faraday cup is 1×10^{-12} A; this equates to $6 \times 10^6 \frac{\text{charges}}{\text{s}}$. Using equation (1.36) it is possible to calculate the excitation rate into the metastable states in the ion source to be $2 \times 10^{13}\,\text{s}^{-1}$. This number however can be further narrowed down by the calculation of the

neutral gas flow through the entrance plate of the rod system using equation (3.2) for effusion (assuming ideal gas behavior).

$$z = \frac{1}{4} \cdot \frac{N}{V} \cdot \bar{v} \tag{3.2}$$

Utilizing the collision rate for the aperture however does not suffice since it takes all of the particles into consideration. It is necessary to find the probability for a given particle to be in a metastable state which can be estimated if the ionization probability is assumed to be 0.001 in the EI source. This further assumes that every 1000th particle is an ion and thus one in every 28000 particles is a metastable species. Combining the neutral gas flow rate through the aperture it is possible to derive an equation to estimate the rate of metastables exiting the ion source.

$$z_{metastable} = \frac{1}{112000} \cdot \frac{N}{V} \cdot \bar{v} \cdot A_{aperture} \tag{3.3}$$

The argon metastable flow is thus calculated to be $5 \times 10^{11}\,\mathrm{s}^{-1}$ at a pressure of 1 Pa and a temperature of 500 K in the ion source. Comparing the metastable flow rate and the required amount of charges on the faraday cup to raise the baseline as observed, it follows that every 500000th particle, or 0.0002% of all metastables present, leads to a corresponding reaction on the faraday cup to be the main reason of this shift employing the faraday cup. Trajectory simulations are used to determine if this number is reasonable or not.

3.2.2.2 Molflow simulations

The simulations to determine how many neutral particles from the ion source can realistically interact with the faraday cup were conducted with molflow. This allows not only simulations of the total amount of hits on the faraday cup but also narrowing down the area where the particles impinge. This is important data to evaluate the likelihood of neutrals hitting the SEM since there is at least one collision with the faraday cup required to result in a trajectory towards the conversion dynode. Since molflow is a raytracing program there are no collisions implemented into these simulations. it is designed to get a basic understanding of the amount of successfully transmitted neutrals not taking collisions into account. The goal of this simulation is to evaluate the maximum percentage of

neutrals hitting the faraday cup because collisions will reduce this number. Figure 3.23 shows the simulation box of the QMF implemented in molflow. The included metal surfaces are the last electrode of the ion source, the rod system, the housing of the rod system, the deflection plate and the faraday cup. The rest was left out to cut down on complexity and thus computing time.

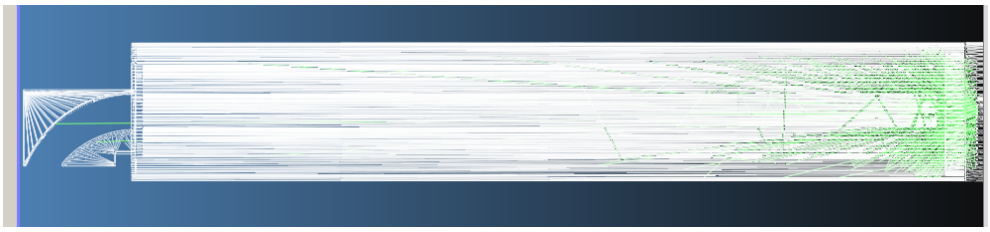

Figure 3.23: Full model of the molflow simulation of the simplified QMF.

The neutrals were created within the last aperture of the ion source with a diameter of 1 mm. The amount of created particles equals the calculated flow of metastables through this aperture. It is visible from the green lines in figure 3.23 that the majority of particles is lost on other metal parts of the system. This is due to the assumed probability that an argon in a metastable state has a chance of about 80% to experience a relaxation when it interacts with a stainless steel surface [80]. This number is dependent on many factors but its magnitude is sufficient for these initial simulations.
Figure 3.24 depicts the results of the impingement rates at each part of the detector grid. It is clearly visible that there are several areas on the faraday cup with significantly different hit rates. The direct trajectory from the ion source towards the surface is the most likely as visible from the color map. The collisions with the surface are seen to be a projection of the view from the ion source onto the faraday cup. The total percentage of particles created that randomly hit the surface of the faraday cup is 0.046 . Comparing the approximate number of electronically excited neutrals leaving the ion source ($5 \times 10^{11}\,\mathrm{s}^{-1}$) results in $2.3 \times 10^{8}\,\mathrm{s}^{-1}$ of these neutrals actually reaching the faraday cup. This is still significantly larger than the minimum needed amount of $6 \times 10^{6}\,\mathrm{s}^{-1}$ for raising the base line as observed. As a first result of the molflow simulations it thus appears realistic that neutral metastables are created in the ion source and reach the faraday cup where they induce the baseline shift via surface reactions. This is also in agreement with every experiment conducted. Going further in depth

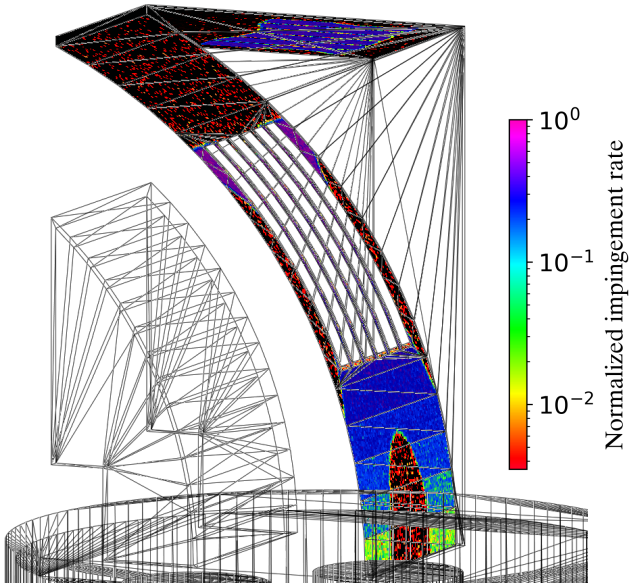

Figure 3.24: Depiction of the impingement rate on the faraday cup.

on the results of the molflow simulations it is possible to identify four distinct areas of the surface of the faraday cup where such reaction my take place. The areas are

- Area 1: The area below the grid, dominantly blue in figure 3.24
- Area 2: The grid itself
- Area 3: The purple area the neutrals hit if they traverse the grid
- Area 4: The area closest to the SEM, almost completely black with red dots in figure 3.24

Molflow allows to calculate the individual impact rates for a graphical representation in addition to calculation of relative numbers representing the hit rate in each area. Table 3.2 lists the percentage for every created particle to hit the respective area of the detector. These numbers are important to evaluate the possible trajectories after the interaction with the surface as a metastable particle hitting the faraday in area 3 is almost certainly not leaving the cup structure before relaxing into the ground state, while particles hitting areas 2 and 4 may travel towards the SEM after surviving the initial impact.

Moving on from the faraday cup to the SEM, the picture changes significantly. The baseline shift on the SEM is unlikely to be caused by direct interaction of neutral excited particles on the conversion dynode because there are no direct trajectories from the ion source to this surface, in contrast to faraday cup impacts. A neutral particle needs to either experience a very unlikely gas phase collision within the deflection unit to change its trajectory towards the SEM or a collision with the faraday surface with the same outcome while not being de-excited in this interaction. The only areas potentially leading to trajectories towards the SEM after a collision with the faraday cup are areas 2 and 4 and the calculated probability for a metastable to hit those areas is 0.0081 %. This alone may still explain the baseline shift since the SEM strongly amplifies any secondary ion signal, so only a few metastables hitting the conversion dynode can contribute to a significant signal. However, 0.0081 % are the total maximum number assuming every particle impacting in these areas is reflected with a trajectory leading to the SEM. This is exceedingly unlikely and the real number of these specific collisions is much lower. To evaluate the expected number of collisions between neutral excited argon and the conversion dynode SPARTA simulations were carried out. In this case, SPARTA has advantage over molflow because it allows to calculate particle-particle collisions and implement gas phase reactions. The aforementioned unlikely collisions changing the trajectory of a particle towards the SEM are also taken into account, as unlikely as they are to occur.

Area	% of total hits
1	0.0105
2	0.008
3	0.027
4	0.0001

Table 3.2: The percentage of electronically excited neutrals leaving the ion source colliding with each defined faraday cup area.

3.2.2.3 SPARTA simulations

The simulation was designed to deliver results for both detector systems and the respective probability that a given particle experiences a collision with the surface before de-excitation. Every time a metastable hits a surface, an 80 % probability for the particle to be deleted from the simulation was assumed. The simulation was initialized such that every particle entering the simulation box is a metastable at first, i.e., no ground state particles were present at anylocation in the simulation domain. This has several advantages: First it is difficult to simulate neutral argon and argon metastables at the same time with realistic distributions, because the respective numbers are so dramatically disparate. Second, higher metastable numbers lead to more robust statistics. Third, deleting such particles after a collision rendered handling the pressure in the system favorable.

However since the simulation was designed to be 2D the geometry of the rod system had to be simplified. It was important to take the amount of particles into account that are lost in the rod system, but the gaps between the rods would have been lost in the simplification. To overcome this issue the rod system was replaced by a segmented geometry with the same solid rod/open space ratio as the authentic device. This allowed to keep computation time low while not losing too much validity of the simulation. In both the simulated and in the real rod system the probability for a neutral to escape through the rods is 54 %. The grid at the deflection unit got similar treatment and was segmented with a 33 % transmission rate. The influx of bulk neutral particles into the ion source was set to achieve a pressure of 1×10^{-2} mbar in the ion source and 1×10^{-5} mbar in the deflection unit. This geometry is shown in figure 3.25. It includes the ion source, the abstracted rod system, the casing of the rod system, the deflection unit, the grid section of the faraday cup, the rest of the faraday cup, the shielding of the SEM and the grid in front of the conversion dynode of the SEM.

The goal of these additional simulations was to confirm the results obtained with molflow while including bulk gas collisions and to achieve more realistic hit rates on the surface of the conversion dynode. As a first result, the pressure of the system at every location gives insights into the particle density of metastable

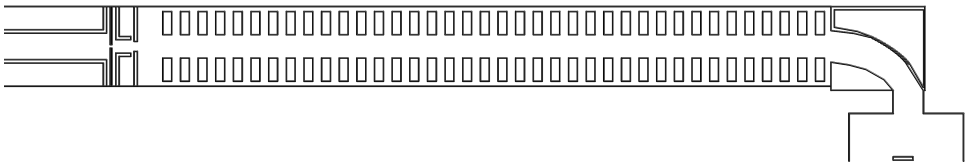

Figure 3.25: Abstracted model of the QMF as implemented in SPARTA.

argon in the deflection unit and close to both detectors.

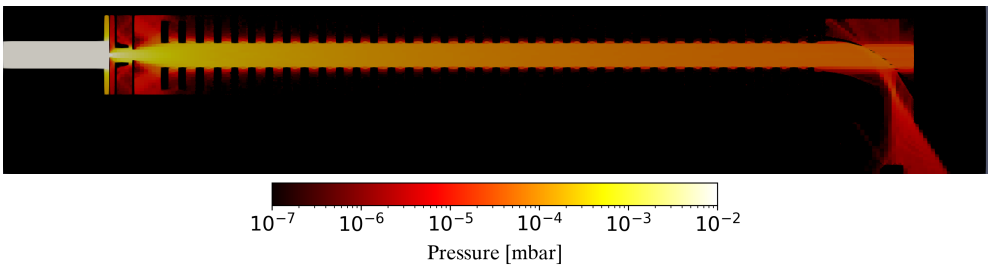

Figure 3.26: Metastable pressure distribution in the QMF device simulated with SPARTA.

Figure 3.26 shows the result of that simulation. The pressure of 1×10^{-2} mbar in the ion source and 1×10^{-5} mbar in the deflection unit are close to the values measured in a typical experiments. The trajectories look similar to the results of molflow simulations, i.e., most particles travel through the grid of the faraday cup and are then trapped inside of the cup structure. It is also visible that even if a particle is deleted with an 80 % chance on every impact and the probability for a metastable to collide exactly at the right collision on the surface of the faraday cup there is still a sizeable amount of electronically excited particles moving towards the SEM.

The number of de-excitation reactions taking place on each respective surface were calculated for the SEM, faraday cup, rod system, electrodes of the ion source, and specifically the grid system of the faraday cup. Note that this is not the total amount of hits but rather the number of de-excitation reactions, which amount to 80 % of all hits.
As expected, the vast majority of metastable argon atoms (97 %) is lost within the ion source. Since the apertures of the SPM700 EI source are the parts with

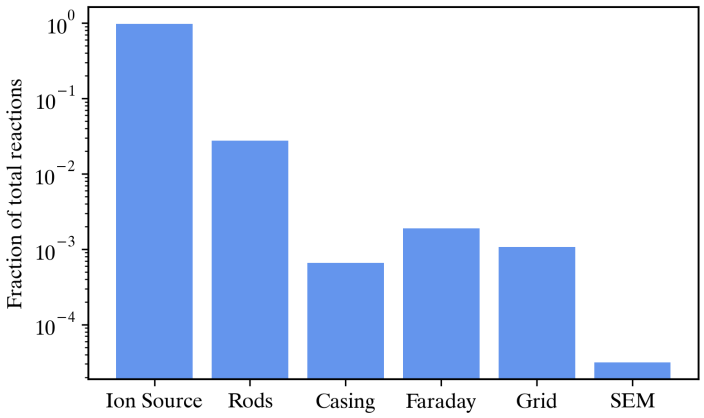

Figure 3.27: Relative amount of relaxation reactions on each surface of the employed MS.

the lowest inner diameter of the device, it is not surprising that the loss rate is that large in this area. Out of those that exit the ion source, the largest part impacts on the rod system and is thus lost for reactions on the detector systems. However the casing, even though it makes up a big fraction of surfaces within the QMF experiences very few reaction events. This results from the trajectories of excited species leaving the ion source having large axial velocity components, while there are several collisions needed to strike the casing of the rod system. As mentioned before the faraday cup is seperated into the grid part and the rest of the detector since collisions with the grid yield a higher probability for trajectories facing to the SEM. The calculated amount of reactions on the faraday cup are comparable with the molflow simulations, i.e., 0.1 % on the grid and 0.2 % on the additional surfaces of the detector. Returning to the rates discussed in section 3.2.2.1 this results in roughly 6×10^{10} total reactions per second on the faraday cup leading to a maximum signal of 9×10^{-9} A. This is still higher compared to the experimentally observed shift; a lower reaction rate than theoretically expected is conceivable as a result of contaminated surfaces and unfavorable angles of incidence.

The SEM experiences 3×10^{-3} % of the total de-excitation steps, so corresponding roughly to a number of 6×10^{8} reactions per second. It is not possible

to deduct an electronic signal from these data due to the amplification of the detector; however assuming every metastable striking the conversion dynode releases an electron translates to 9×10^{11} electrons per second and taking the gain of the SEM (10^6 to 10^8) into account thesse numbers are large enough to generate a baseline at 1×10^{-10} A.

To estimate the variance of the results in accordance to the applied reaction rates on surfaces, a sensitivity test was conducted utilizing 60 % and 70 % de-excitation rates, respectively. The results are shown in figure 3.28.

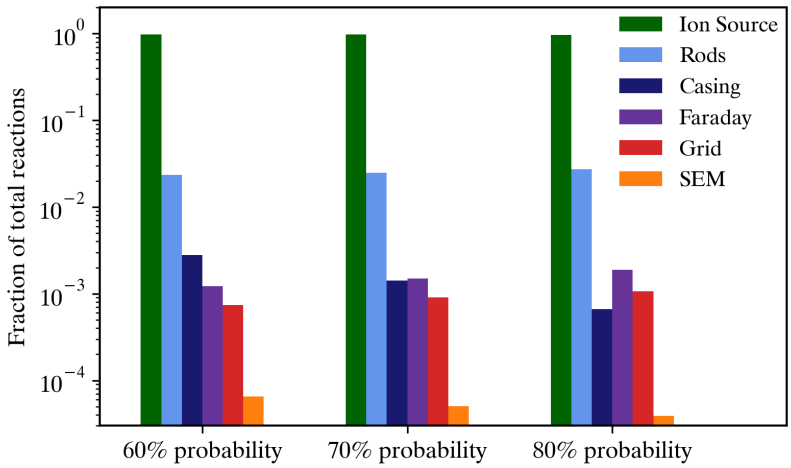

Figure 3.28: Comparison of different relaxation reaction rates on surface collisions in a SPARTA simulation of the entire QMF.

The ratio of lost ions within the ion source exhibits little disparity in the observed setups since it is so close to 100%. The de-excitation reactions taking place on the rod system also experience almost no change, however more argon metastables strike the outer casing of the rod system when the de-excitation probility is lower, which is attributed to the fact that in order to reach the casing at least one collision is needed and the number of metastables surviving a collision naturally changes in these simulations. The only surfaces where an increase of reactions is noticed as the probility increases, are the faraday cup and the grid of the faraday cup. This indicates that most particles impinging on the faraday cup did not interact with any other surface on their way towards the

detector and thus a higher amount of the atoms striking the faraday cup leads to de-excitation, so the total number of reactions on the faraday increases. The SEM on the other hand is exposed to fewer argon particles since they need to collide with the faraday cup and then remain in their metastable state after the interaction to react on the conversion dynode as mentioned earlier. It can be stated that the relaxation rate does not influence the amount of species hitting the faraday cup or the SEM significantly because most of them traverse towards the detector without any prior collisions. There is an observable dependency on this parameter but the variation is only in a factor of 2 and not spanning multiple order of magnitude.

To conclude this section, it is entirely possible that metastables contribute to the baseline shift, based on results these simulations and their interpretation yielded. First of all the number of created metastable particles is theoretically large enough to be the cause for the baseline shift. The amount of metastables reaching the detector surfaces is also sufficient. However figure 3.5 indicates that the majority of the baseline shift is ionic in nature, so the direct interaction between the metastable and the detector can be a contributing factor but not the main cause. The equations and simulation results of this section are necessary to evaluate if secondary ions created by neutral metastables within the deflection unit has a significant influence or not.

3.2.2.4 Photons

As a second possible factor for the baseline shift to occur, photons and their products are to be investigated. First of all it is important to evaluate the frequency of the photons in question and their origin. Bremsstrahlung is ruled out because the effect still occurs if the RF voltage of the device is turned off as seen in figure 3.13 and heat radiation directly from the ion source was discarded because the frequency is not high enough to result in the photoelectric effect on most metals. This leaves radiative transitions as a source for photons that can theoretically cause a baseline shift. It has already been shown in the previous section that the particle density of metastable species downstream of the rod system is high enough so photons emitted from those particles have to be taken into account.

Given the excitation cross sections in an EI source, the most likely metastable states for argon are the $^1S_3$ and $^1S_5$ states. Energetically these states are located 11.72 eV and 11.55 eV above ground level, respectively[46], while the work function for most metals is in the range of 3-5 eV[27]. The high energy of the photons emitted by particles relaxing into the ground state from the described excited states exceeds the work function of every metal material employed in the QMF and thus can lead to the ejection of a photo-electron from the surface of the detector. Given the stability of metastable states the lifetime of the two above refenerced states are 56 s for the $^1S_3$ state and 45 s $^1S_5$ state[33], which is sufficiently long to travel from the ion source into the deflection unit and decay in this area.
Lithium Fluoride quantitatively blocks particles while being transparent for photons with $\lambda > 104$ nm (E < 11.92 eV). As a result the effect of the radiation emitted by the mentioned argon metastables as they relax to the ground state can be transmitted through an LiF window while particles are blocked. This allows for experiments where particles and photons and their effects on the baseline can be observed separately.

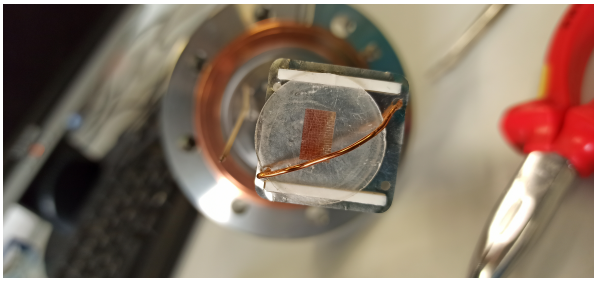

Figure 3.29: Photo of the LiF window in front of the SEM conversion dynode.

Figure 3.30 shows the results of such an experiment with an LiF window placed right in front of the conversion dynode of the SEM. Since there are no signals at all and the baseline is at the level of the electronic noise floor, it is concluded that particles were quantitatively blocked from reaching the conversion dynode. More importantly, it indicates that photons >104 nm are not contributing as a cause for the baseline shift. If the baseline was even slightly elevated it could be argued that since the optical cutoff of the LiF material is not very sharp and the photons emitted by argon metastables do not pass the window with

100 % efficiency. But since there is no sign of a baseline shift at all it is securely assumed that photons are no contributing factor for the elevated baseline when using the SEM as detector. It has to be noted however that photons can still play a role in the production of secondary ions within the deflection unit and further investigation is needed.

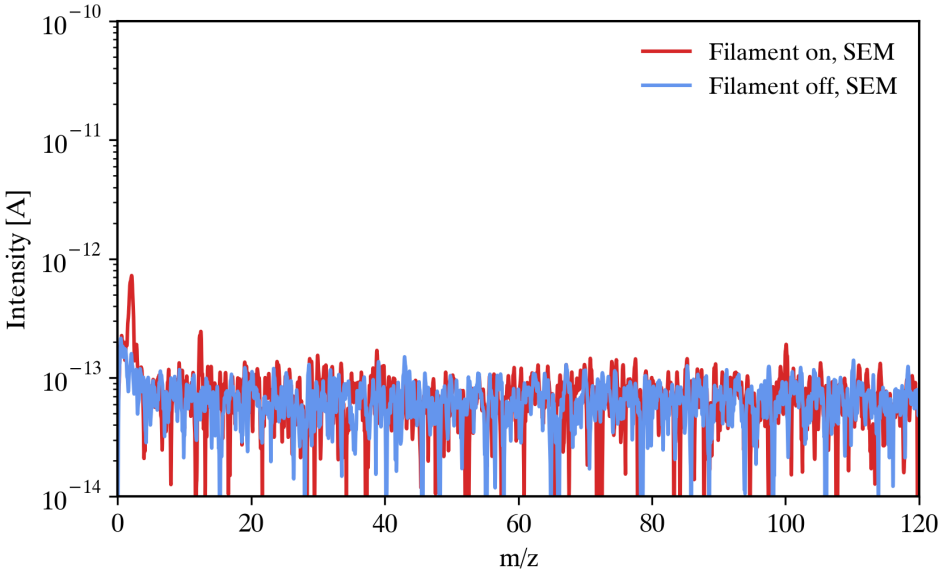

Figure 3.30: Mass spectrum while the SEM conversion dynode is shielded with an LiF window.

To determine if the same arguments hold up for the baseline elevation when using the faraday cup, the experiment was also conducted with the LiF window placed downstream of the entrance plate of the ion source. This way no particles can exit the ion source while high energy photons can interact with the faraday cup surfaces. However, it is clearly demonstrated that the baselines of both detector systems show no shift at all and thus photons as a direct source for the elevation of the baseline are ruled out.

Returning to the schematic shown in figure 3.22 and utilizing the acquired data it becomes apparent that the only mechanism to rationalize all experimental and modeling results to this point are secondary ions are being produced in the deflection unit. This was already shown in figure 3.5, since only cations respond to the exposure to electric fields and are detected by the SEM. The

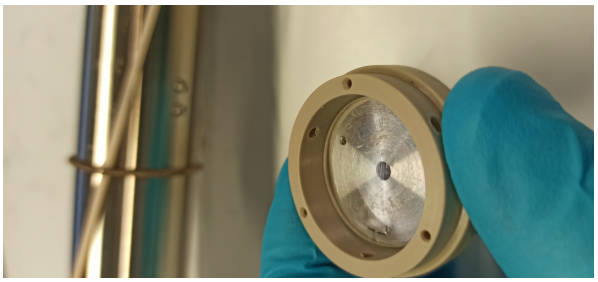

Figure 3.31: Photo of the entrance plate covered by an LiF window.

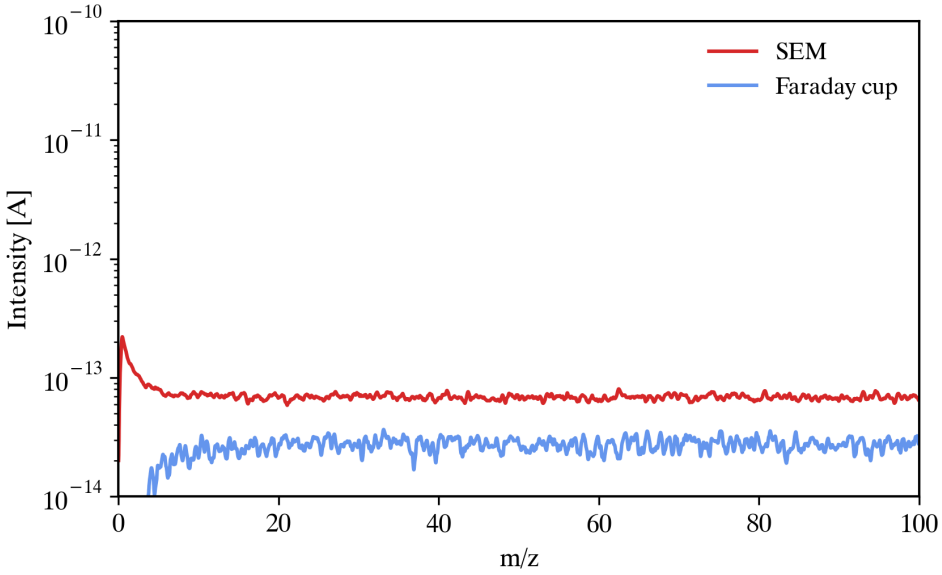

Figure 3.32: Mass spectrum while the entrance plate is covered by an LiF window.

mechanism for the conversion of neutrals into ions however is still unclear and will be investigated in the following section. It has to be noted however that such secondary ions do not quantitatively account for the entire baseline shift, since the baseline is still elevated by one order of magnitude even when ions are quantitatively filtered out so there are at least two superimposed mechanisms.

3.3 The mechanism behind secondary ionization

There are three distinct mechanisms that can realistically lead to secondary ion production in the deflection unit: Photoionization, resonant ionization and gas phase reactions of electronically excited species.

3.3.1 Photoionization

The tungsten filament emits photons with a maximum energy of 3.99 eV[97], thus these photons cannot ionize ground state argon atoms. The energy gap between the two lowest metastable states of argon and the ionization threshold is 4.04 eV or 4.21 eV[46], thus even the ionization from these states is impossible for photons generated by the filament of the EI source.
Photons generated as a byproduct from recombination reactions within the ion source could provide enough energy to ionize background gas [98]. However the likelihood for these photons to reach the deflection unit is sufficiently low, given the small dimensions of the apertures in the direction of travel and the long travel distance. If a photon is emitted within the ionization volume of the SPM 700 EI source it would need to reach the deflection unit and undergo a gas phase reaction. The deflection unit is located at a distance of 220 mm downstream of the ion source and the interrod radius of the rod system is 3.5 mm. Assuming the photon will not reflect from the metal rods, i.e., the trajectory from the ion source has to end directly in the deflection unit, the probability of such trajectories can be simulated with a corresponding molflow model using a similar geometry as compared to 3.23 including the ion source.

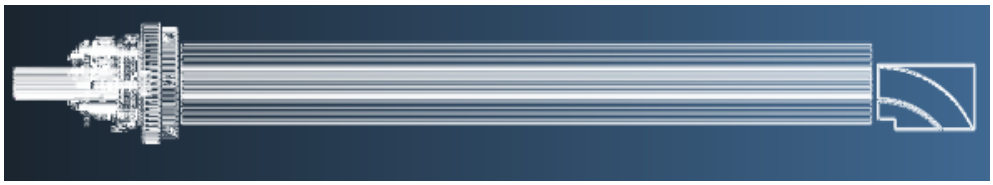

Figure 3.33: Molflow geometry to simulate the ratio of photons that originate in the ion source and reach the deflection unit.

The simulation yields a ratio of photons reaching the deflection unit to total photons of 4.5×10^{-6}. This is assuming photons are "deleted" after a surface collision while in reality there is a chance that a photon is reflected by the stain-

less steel surface so the real ratio may be slightly higher. Taking the mean free path of argon under the circumstances in the ion source (1 Pa, estimated 400 K) into consideration, the probability of a recombination reaction to occur is calculated. The mean free path is in the range of one cm while the diameter of the ionization area is 8.2 mm. As a result, every ion statistically experiences about one collision within the EI source. Assuming the ratio of recombination reactions inside the SPM source is sufficiently largeand considering the very low chance for photons emitted in a recombination reaction, there is only a very low probability that a photon travels all the way through the device and ionizes a neutral particle in the area of the deflection unit at a pressure of 1×10^{-4} mbar. Nevertheless, an experiment was conducted to evaluate the impact of this effect on the baseline. The pressure within the EI source was held constant while the pressure in the deflection unit was increased. If photoionization of neutrals within the deflection unit was a contributing factor in the elevation of the baseline, the position of the baseline should respond when the pressure is increased. This does not change the fact that the probability for a photon to reach the deflection unit in the first place is miniscule but assuming a sufficiently high amount of photons does end up in the deflection unit the increase in pressure will lead to higher ionization rates and thus an elevated baseline. The results of the experiment are illustrated in figure 3.34.
The pressure within the deflection unit could not be measured directly and is thus represented by the pressure in the analyzer region of the device. The pressure in these two regions is not exactly the same but they are directly linked so the pressure in the analyzer region can be used as an indicator of the pressure in the deflection unit.

Three different cases are compared in the following: i+ii) When the pressure within the ion source is held at a constant value and the pressure within the deflection unit is increased by an order of magnitude (the blue and black traces) the baseline is not influenced. If gas phase reactions with neutral background gas in this area played a role in the baseline shift, it should rise more as the pressure increases. In contrary to the pressure in the deflection unit, the pressure in the ion source is of utmost importance for the extent of the baseline shift. iii) Comparing the red and blue traces the pressure within the deflection unit is the same however the electron ionization source is operated

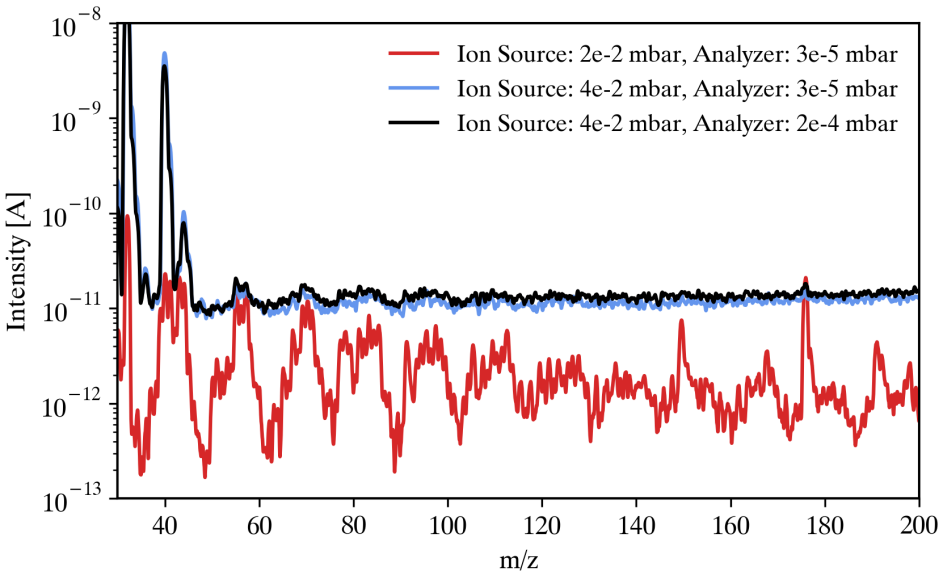

Figure 3.34: Influence of the pressure inside of the EI source and inside of the deflection unit on the baseline

at a lower pressure in the red dataset. It is thus concluded that the baseline is only affected by the pressure inside of the ionization source while any pressure region downstream has no effect.

3.3.2 Gas phase reactions

Gas phase reactions leading to energetic photon emission, as mentioned earlier, are improbable but not impossible. The mean free path of argon at a pressure of 1×10^{-5} mbar and 300 K (conditions assumed in the deflection unit), is in the 40 to 50 meter range and the entire distance between the ionization source and the detector is about 30 cm. This renders the interaction of a photon and a given particle and even more so the interaction between two excited particles rather implausible. However it is stressed again that the observed level of the baseline shift is not of a large magnitude either so such reaction cannot be disregarded without experimental investigations. To achieve a rough estimation of the probability of a collision between two metastable species to occur it is assumed that every particle present in the deflection unit is stemming from the gas inlet upstream of the ion source. As estimated in section 3.2.2.1 one particle

out of 28000 exiting the ion source is in a metastable state and thus eligible for ionization via gas phase reactions. Calculating the amount of collisions per second for a given particle at a pressure of 1×10^{-5} mbar and 300 K using equation (3.4) based upon the kinetic gas theory[67], corrected by the assumed ratio of neutral particles to metastable species in the deflection unit gives insight into the likelihood of those reactions. These equations use the most probable velocity ($\widetilde{v}$), the diameter of the particle (d=1.4 Å[99]), the particle density ($\frac{N}{V}$), the temperature (T=300 K), the ideal gas constant (R), the Boltzmann constant (k), the pressure (1×10^{-5} mbar) and the molar mass of the particle (M=0.04 kg) as input parameters. In most cases the velocity in equation (3.4) is the mean velocity $\bar{v}$ but in this case the mean velocity, and thus the mean collision rate, are not as relevant as the most probable parameters so the variables were adjusted accordingly.

$$z = \sqrt{2} \cdot \widetilde{v} \cdot \pi d^2 \cdot \frac{p}{kT} \tag{3.4}$$

$$\widetilde{v} = \sqrt{\frac{2RT}{M}} \tag{3.5}$$

As a result for the most probable velocity a value of $353 \frac{m}{s}$ was obtained and the collision rate was calculated as $1.5 \times 10^{-3}\,\mathrm{s}^{-1}$. This collision rate depicts the amount of collisions between two metastable species per second so to achieve the number of collisions inside of the deflection unit, which is about 2 cm wide, this number has to be multiplied with the time it takes for a neutral particle to traverse the unit. This time is calculated to be 5.6×10^{-5} s via simple division of the speed by the distance so the most probable amount of collisions a metastable particle experiences with another metastable species within the deflection unit is 8.5×10^{-8}.

The above is just a rough estimate so the real number may differ significantly but it will remain miniscule in comparison to the needed collisions on the detector to impact the position of the baseline. this is particularly the case, if it is taken into account that any collision between two metastable species only produces one ion, which additionally reduces the probability for this mechanism to be the main cause for the baseline shift. If the calculations for the metastable flow from the ion source in section 3.2.2.1 are taken into account

as well, it becomes apparent that the flow of metastables combined with the very low probability for an ionizing collision to occur renders this hypothesis impossible.

3.3.3 Resonant Ionization

The mechanism of resonant ionization is most appealing for the baseline behaviour in the present QMS system since it interconnects excited species and ions via a reaction on a present surface. The deflection unit (as seen in figure 2.3) provides the required surface, i.e., the grid region, the solid regions above and below the grid and the plate downstream of the grid (labeled areas 1-4 in section 3.2.2.2).

To deduce if a surface reaction could be the main cause for the baseline shift, experiments were done with the entire deflection unit removed. Hence neutral particles travel straight past the SEM and hit the wall of the device roughly 10 cm behind the SEM. Naturally these experiments could only be conducted using the SEM as detector, since the faraday cup is removed. However since the shift is more pronounced with the SEM as detector in the first place it can still give important insight into the involved mechanisms. The deflection unit, including the faraday cup, was thus replaced by a stainless steel plate placed orthogonally to the ion beam. This was done to discern if any surface close to the SEM and exposed to a stream of excited species will lead to a detectable baseline shift or if there are a specific features present on the deflection unit (adsorbates etc.) giving rise to this behavior. This experiment was conducted using argon as carrier gas, -2500 V conversion dynode potential, 1×10^{-2} mbar ion source pressure and SPM settings as depicted in 2.1. The result is shown in figure 3.35.

It is apparent that there is a remarkable difference for these setups regarding the baseline. The electronic noise floor at 1×10^{-13} A (as seen in figures 3.1, 3.13, 3.30 and 3.32) so even if there is no surface present for orthogonal impacts and subsequent resonant ionization the baseline is elevated slightly. This can be explained by reactions on the borders of the casing of the device or at the very end of the rod region or by applying a different mechanism altogether, namely photoionization or ionization via gas phase reactions.

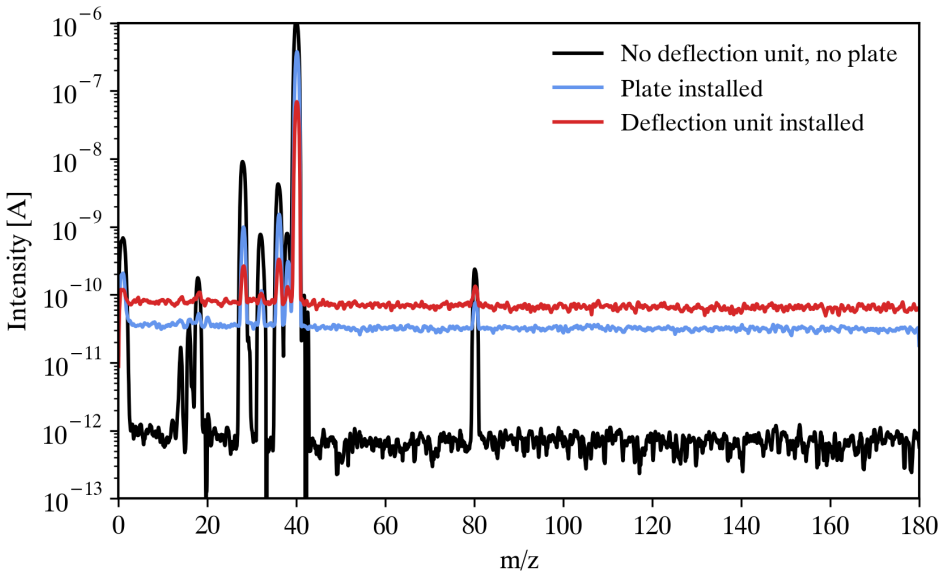

Figure 3.35: Comparison between the conventional deflection unit, a stainless steel plate or no surface present orthogonally of the quadrupole axis

The results of the molflow simulations (see section 3.2.2.2) indicate where neutrals impinge on the faraday structure and naturally these are the locations for surface reactions as well. However even low impact rates might still be sufficient to induce SEM signals, provided the ions are directed towards the SEM after impact. SIMION simulations were carried out to gain knowledge about the trajectories within the deflection unit and the probability for each ion to reach the conversion dynode. The relative amount of ions generated in each area is linked to the impact rates obtained from the molflow simulations. Since the deflection voltage has a major influence on the flight path of the ions, the potential on the electrode was changed stepwise, while the SEM conversion dynode was set to a fixed potential of -2500 V. The potential on the deflection unit was stepwise changed in the range between -200 V and 200 V. The ions were created with thermal velocity, since the neutral particles producing these ions likely possess velocities of a similar value. The rod system is still present in the simulation geometry due to its effect on the ion

trajectories. The lack of a quadrupole post filter leads to a significant influence of the fringe fields generated by the quadrupole rods on the electric field within the deflection unit, since the DC bias of the rod system is as high as 140 V.

Figure 3.36 displays the equipotential lines within the deflection unit for selected representative deflection plate potentials. The grid region is not visible in the pictures due to the 2D projection but it is present in the simulations. At 0 V the negative potential of the SEM barely reaches into the volume of the deflection unit and only affects ions that are created at the top of the faraday cup. At 10 V deflection voltage the picture does not change drastically but the influence of the SEM is further decreased while the positive potential of the rod system completely immerses the deflection plate. At -170 V the -5 V equipotential line completely covers the free region between the grid of the faraday cup and the deflection plate so that every ion produced in this region is going to be directed towards either the deflection plate or the SEM, depending on initial conditions, such as velocity and exact position. At +170 V an entirely positive electric field surrounds the deflection unit, which means it is very unlikely that ions reach the SEM at all.

To gather a more complete picture of the behavior of charged particles within the deflection unit including free electrons (generated by the photoelectric effect or in Auger reactions on the metal surface), as they will influence the baseline of the faraday cup, 9000 Ar^+ ions and 9000 electrons were created in the simulation. The simulation was setup to record impacts on the conversion dynode of the SEM, the deflection plate, the rod system and the faraday cup to comprehend the interaction between the charged particles and the different surfaces areas. Figure 3.37 displays the results of the simulations. In figure 3.38, exemplary trajectories are shown for 0 V, ±10 V and ±170 V deflection plate potentials.

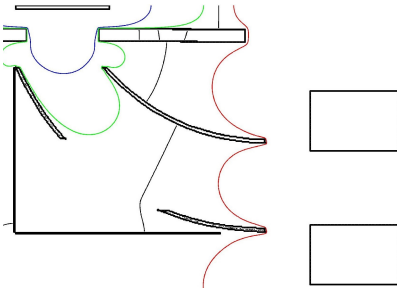

(a) Deflection voltage 0 V

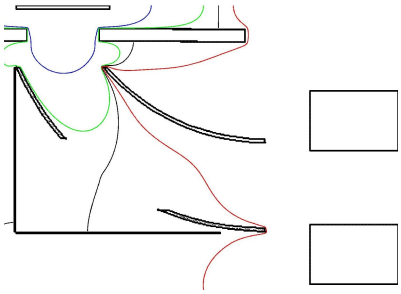

(b) Deflection voltage 10 V

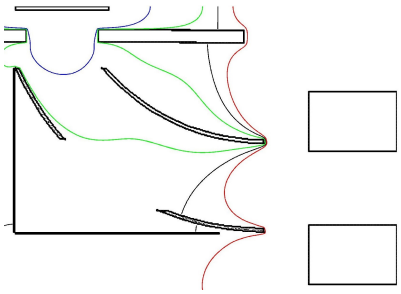

(c) Deflection voltage -10 V

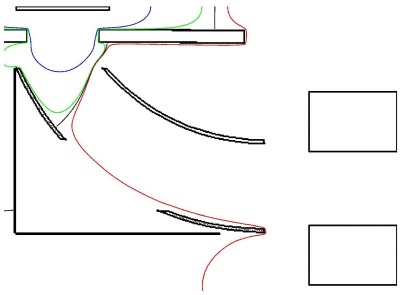

(d) Deflection voltage +170 V

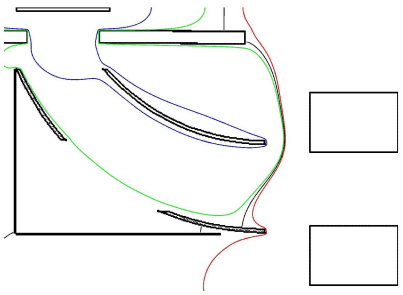

(e) Deflection voltage -170 V

Figure 3.36: Equipotential lines within the deflection unit. Blue = -150 V, green = -5 V, black = 0 V, red = 10 V.

Figure 3.37b demonstrates that at high negative deflection potentials the faraday cup is almost exclusively struck by electrons. This begins to change at around -50 V and breaks even with Ar^* ions at about 30 V to 40 V. After a steep rise 100 % of the ions are detected by the faraday cup and only about 10 % of the emitted electrons. This change is also visible in the trajectories shown in figure 3.38. At -170 V deflection voltage almost every ion is collected by either the deflection plate or the SEM. However already at -10 V deflection plate potential the red ions, those that were generated in area 1 (directly below the grid), are affected by the positive bias of the rod system and are subsequently collected by the faraday cup. Revisiting figure 3.3, a positive deflection potential translates to the highest baseline using the faraday cup as the detector. It stays at the highest level for the 150 V and 75 V experiments without declining and only the 0 V setup leads to a decline of the baseline. This behavior is further illustrated by also inspecting figure 3.37b. It is discernible that at positive potentials every ion that was potentially produced by the resonant ionization mechanism interacts with the faraday cup while it is not exposed to a high amount of electrons. Electrons would in turn induce a current of the opposite polarity, effectively reducing the baseline. The decline of the ion impact rate starts at about 50 V and is rather steep from there on and is accompanied by a similarly steep increase in electrons reaching the electrode, which corresponds with the decrease in the level of the baseline observed in the experiment. This implies that the hypothesis of resonant ionization can explain the experimental results utilizing the simulated data. Additionally this mechanism is more favorable than the other investigated mechanisms in prior sections are, since it only involves the interaction between a surface and an excited species instead of a gas phase reaction.

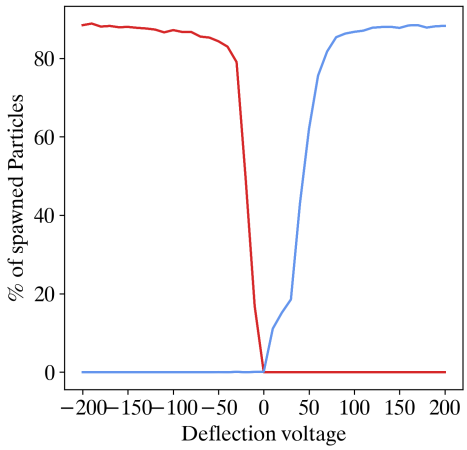

(a) Impingement on the deflection plate

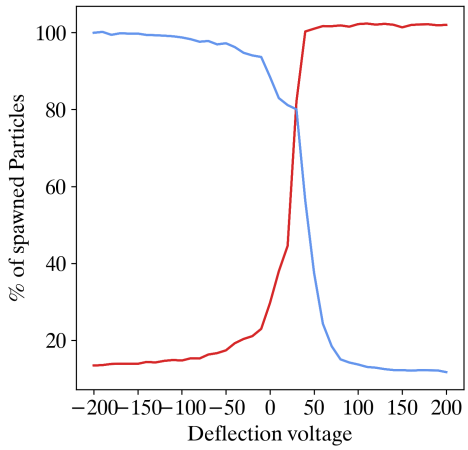

(b) Impingement on the faraday cup

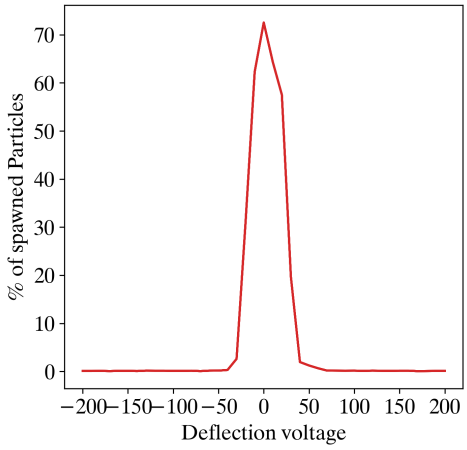

(c) Impingement on the conversion dynode

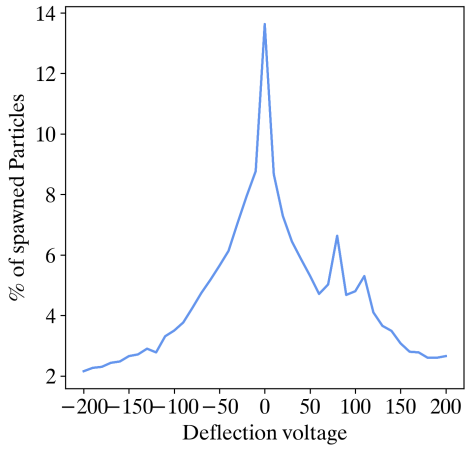

(d) Impingement on the rod system

Figure 3.37: Visualization of the amount of particles reaching the indicated surface. Red = Ar^+ ions, blue = electrons.

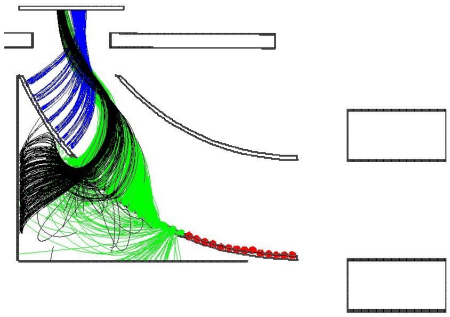

(a) Deflection voltage 0 V

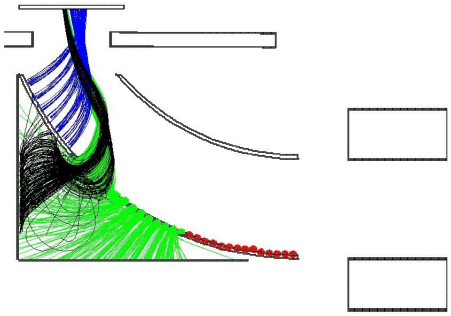

(b) Deflection voltage 10 V

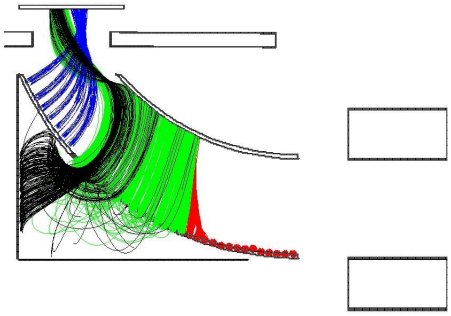

(c) Deflection voltage -10 V

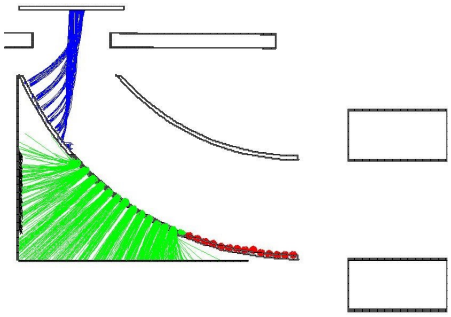

(d) Deflection voltage +170 V

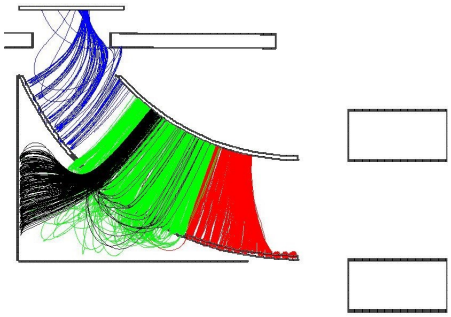

(e) Deflection voltage -170 V

Figure 3.38: Trajectories of Ar^+ ions within the deflection unit at different deflection plate potentials. Colors indicate the ion origin areas. Red = below the grid (area 1), green = at the grid (area 2), black = through the grid inside of the cup structure (area 3), blue = above the grid (area 4).

The plot for the deflection plate (figure 3.37c) is almost the inverse of the one for the faraday cup. At high negative applied potentials about 90 % of the ions are directed towards the deflection plate, since it is in close proximity to the majority of ions. A steep decline starting at about -50 V ends in 0 ions hitting the electrode at 0 V which is accompanied by a steep increase of electrons impacting on the plate. In all cases except 0 V, the majority of ions and electrons either end up on the deflection plate or the faraday cup.

Since the rod system is positively biased only electrons can interact with the rods. The overall impact rate on the metal rods is low and exhibits a maximum at 0 V. This can be explained by the proximity of the deflection plate to the ions and its elevated effect on their trajectory. There are visible spikes present at approximately 80 V and 110 V, which may be statistical outliers since the exact number of impact events is very low.

The impact rate on the conversion dynode (figure 3.37c) exhibits a pronounced maximum at 0 V applied to the deflection plate. Beginning at the maximum the curve declines in both the positive and the negative direction. Figure 3.38 shows that ions depicted in blue (area 4, above the grid) impact on the SEM under all circumstances since the conversion dynode is so close to these ions and the potential on the SEM is considerably higher compared to the deflection plate. Naturally, electrons never reach the conversion dynode. Ions from within the faraday cup structure (black trajectories) only find their way to the SEM conversion dynode if the potential on the deflection plate is low, which also counts for ions originating from the grid (green trajectories). The simulations clearly demonstrate that only ions from area 1 (red trajectories) do not reach the SEM in the 0 V case, due to the influence of the bias of the rod system. The pattern of plot 3.37c is very reminiscent of the experimental data shown in figure 3.5. Figure 3.39 compares the two normalized datasets. They do not match exactly but the general shape is in good agreement. The experimental data display a steeper slope and only decline to a value of 1.7×10^{-2} while the simulated data decrease to values between 1×10^{-3} and 2×10^{-3}, which translates to the electronic noise floor of the device, given the fact that the baseline shift is about 3 orders of magnitude high. The difference between the simulated dataset and the experimental results can be explained

by assumptions made for the SIMION and molflow simulations: The molflow simulations discard gas phase collisions entirely, since it is merely a raytracing program. The ion generation areas in the SIMION simulations were taken directly from the results of molflow without taking into account that the slope of the surface could influence the rate at which resonant ionization takes place. Additionally the initial velocity of the ions was assumed to be 400 $\frac{m}{s}$, the mean velocity of argon at 300 K, maybe this assumption was wrong and neutral particles reach the deflection unit at higher velocities due to expansion into the rod region or the ions are accelerated during the ionization reaction. The two datasets are too similar however to be a mere coincidence. The fact that the experimental data results in a higher baseline at the edges of the curve compared to the simulations can be explained if another mechanism is active in addition to resonant ionization. As mentioned earlier the direct interaction of metastable species with the surface of the conversion dynode may induce a shift in the baseline as well; this however is not incorporated in the simulations.

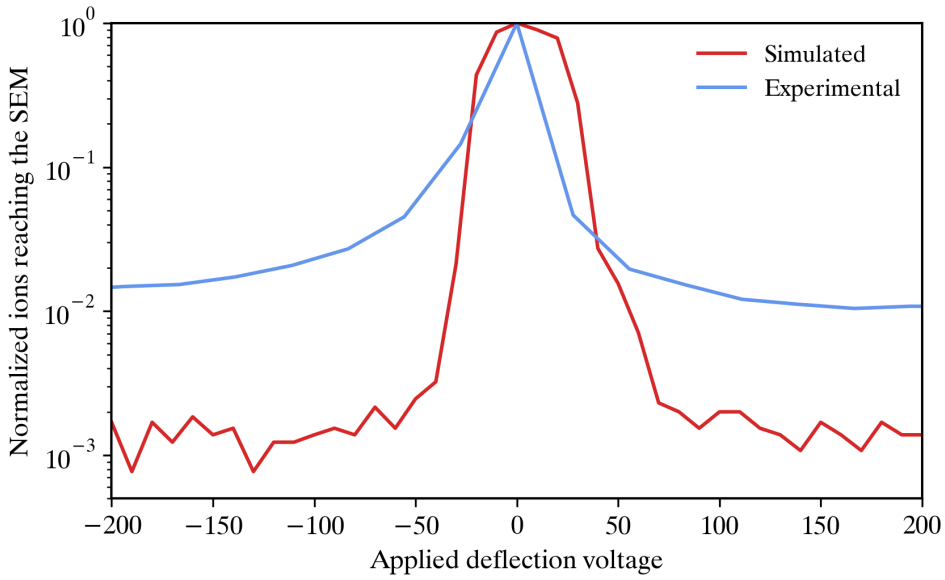

Figure 3.39: Comparison between the experimental signal on the SEM and the simulated hits on the conversion dynode.

In summary, photoionization within the deflection unit was unlikely to begin with and experiments with elevated pressures within the deflection unit did not influence the baseline. This shows that only the pressure within the ionization source is of relevance in this regard while the probability for a collision between photons and neutral gas phase particles should exhibit a dependency on the pressure. Ionization via photons is thus highly improbable.
Gas phase reactions between excited species within the deflection unit are theoretically implausible. A favorable number of collisions a metastable argon atom experiences with another metastable species is at 8.5×10^{-8} while the number of metastable argon leaving the ion source is comparably low, as has been shown. The experimental datasets for resonant ionization, both for the faraday cup and the SEM, were supported by the SIMION simulations, which in turn used data achieved in molflow simulations. The plateau of the baseline using the faraday cup at higher deflection potentials as well as the sharp signal decrease at voltages below $50\,\mathrm{V}$ are visible in the experiment and the simulation. The number of ions striking the conversion dynode of the SEM in the experiments and the simulation are in reasonable agreement. Additionally, the experimental results presented in figure 3.35 suggest the need for a surface in close proximity to the SEM, which can be explained by the proposal of resonant ionization paythways but not with photoionization or gas phase reactions. Every other hypothesis was disproven by experiments, simulations and/or calculations except for resonant ionization. The good agreement between all these datasets strongly supports the hypothesis that resonant ionization is the main cause for the observed baseline shift.

3.4 A novel design for the deflection unit

As figure 3.35 illustrates, the absence of a surface in the direct vicinity to the SEM lowers the baseline significantly. The design for an improved geometry to guide ions from the rod region to the detector region has to work either without such a surface at all or it has to be moved so far downstream so that the conversion dynode potential does not affect the trajectories of ions produced on this surface. The novel geometry has to fulfill several requirements:

- Bridge the rod region to the detectors and the electronics
- Allow the off-axis SEM to detect mass resolved ions from the QMF
- Contain a faraday detector of any sort
- Provide structural integrity for the outer case of the entire assembly
- Allow the installation of a deflection plate
- Suppress the influence of resonant ionization on the mass spectrum

At both terminal ends of the new steering device, i.e., the mounting on the flange where the feedthroughsfor the electronics are located and the downstream end of the rod region, allow no change since otherwise the casing of the rod system and the electronics need to change as well. An opening for the SEM, including screws for the shielding, of the same dimensions as in the original part are inevitable as well. This leaves only the deflection unit including the deflection plate and the faraday cup for modifications. As a first draft to match the listed requirements (except a functional faraday cup and the deflection plate), deflection unit v.2 as shown in figure 3.40 was designed.

At the end of this new stage a 45° slate located which acts as a reflective surface for neutral particles leaving the rod region. The slate geometry leads to trajectories towards the turbomolecular pump after a collision with the surface for neutral particles and ions alike. As a result, the probability for an excited particle to interact with the surface and subsequently be detected by the SEM as an ion is miniscule which further decreases the baseline.
SIMION calculations with 10000 ions were run ahead of manufacturing of the

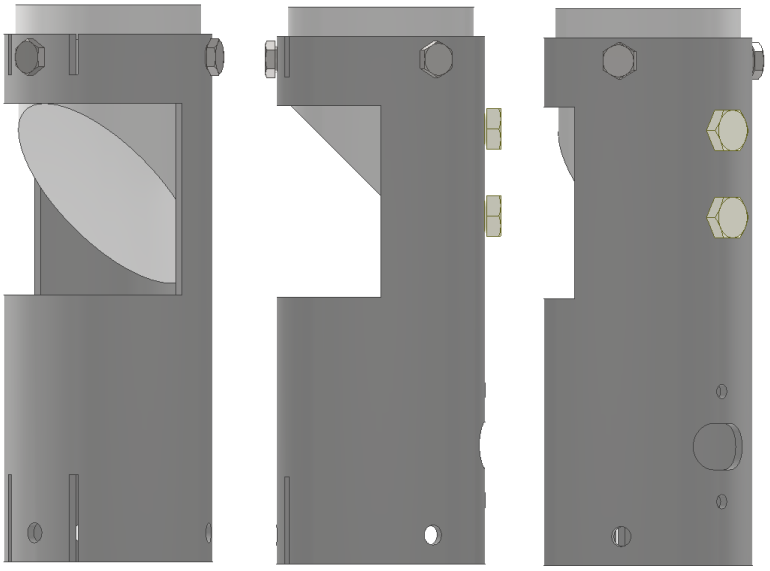

Figure 3.40: CAD model of the novel deflection unit. Ions enter the unit from the bottom and leave towards the SEM via the cutout in front of the conversion dynode. The described slate is located at the top of the unit.

device in order to analyze the ion trajectories pointing towards the SEM. Argon was used for the simulations along with a potential of -2500 V on the conversion dynode. The rod system was set to a bias of 140 V since the influence of the electric field emitted by the QMF has to be considered and the kinetic energy of ions traveling within the quadrupole was set to 7 eV.
It is apparent that the vast majority of ions are too fast to experience a major influence by the applied conversion dynode potential and thus they traverse the deflection unit almost unaffected. About 6 % of the ions are detected by the SEM which is sufficient to achieve a mass spectrum however the signals most likely suffer from the missing deflection potential from the original unit. The main goal of this deflection unit is not to acquire improved mass spectra but to reduce the baseline shift and thus act as another piece of evidence that the proposed mechanism is indeed reasonable.

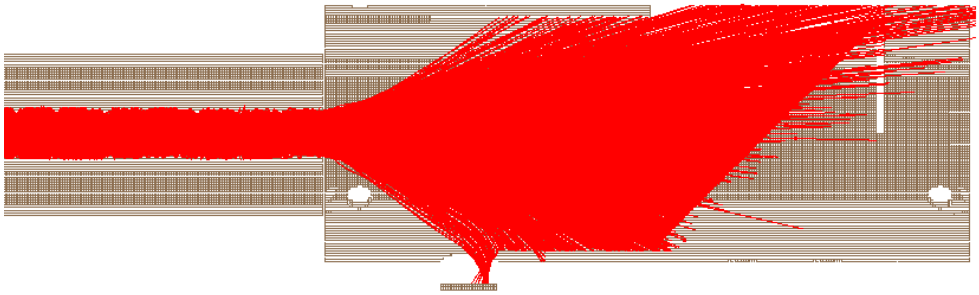

Figure 3.41: SIMION simulations of the new deflection unit.

In order to ascertain that no uncharged particles stemming from the ion source can strike the conversion dynode, SPARTA simulations were conducted to yield the amount of relaxation reactions on each surface of the device including the new unit (similar to simulations discussed in 3.2.2.3).
The results are shown in figure 3.42. As in similar simulations the vast majority of metastables are lost within the ion source and on the rods of the quadrupole and the sum of metastable species striking the grid and the faraday cup of the original unit now impact on the slate of the new device. This implies that the slate can be remodeled into a faraday detector in upcoming iterations of this part of the device. The graph does not show any data for the SEM to emphasize that no particle traverses from the ion source towards the SEM in these simulations. As a direct consequence of the SIMION and SPARTA simulations the new deflection unit should produce a mass spectrum without any noticeable baseline shift and a mass spectrum containing low-intensity ions, which were always absent when using the old unit.

Figure 3.43 compares two mass spectra taken with the old deflection unit and two taken with the new unit using argon as carrier gas and a potential on the conversion dynode of -2500 V. The deflection voltage was not applied in the experiment with the old unit to show the difference between the two setups under comparable conditions.

The mass spectrum taken with the original deflection unit (red mass spectrum) displays the baseline shift while after removing the deflection plate and the faraday cup (purple mass spectrum) no shift at all occurs. With the new deflection unit including the slate (dark blue mass spectrum) a mass spectrum almost identical to the one without the Faraday cup present is recorded. The

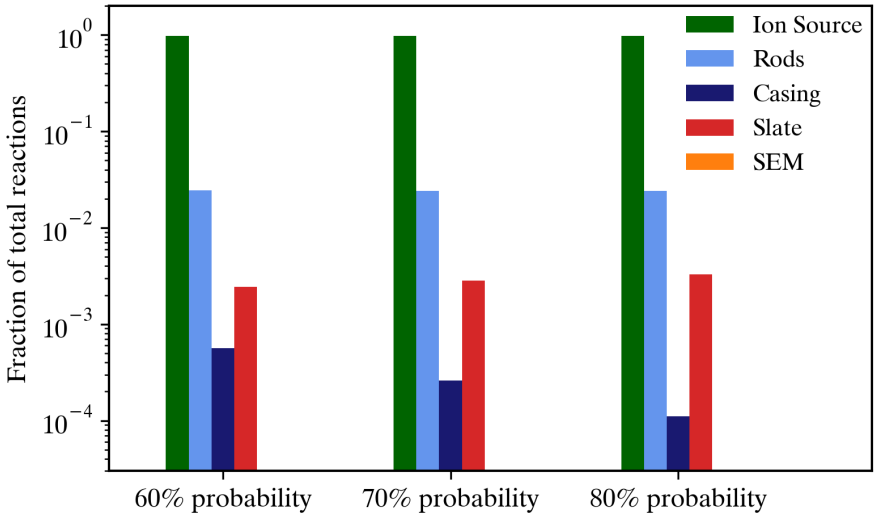

Figure 3.42: Comparison of different relaxation reaction rates on surface collisions in a SPARTA simulation of the entire QMF.

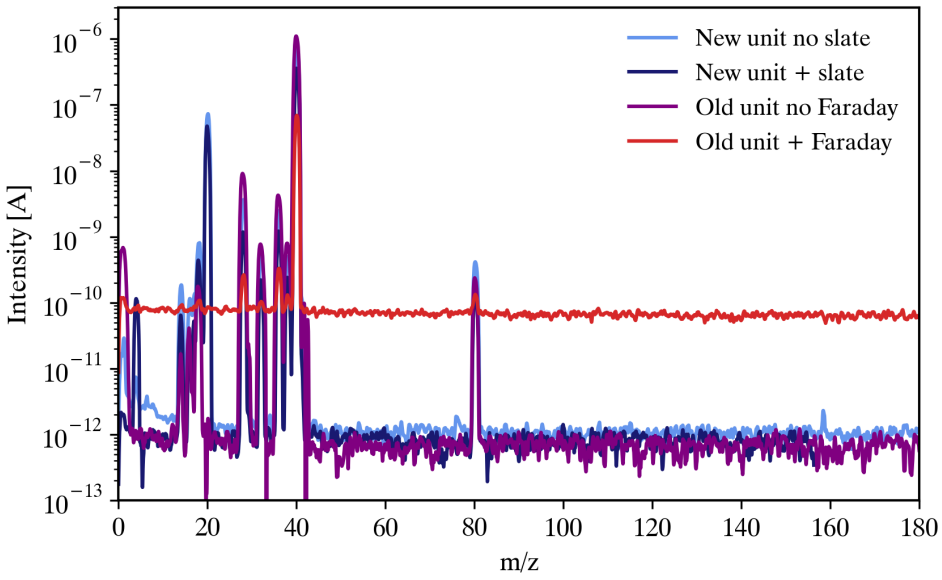

Figure 3.43: Comparison of mass spectra recorded with the original deflection unit and the new deflection unit.

baseline stays at a level of 1×10^{-12} A and even the smaller mass signals are of a comparable intensity. There is no significant difference between the mass spectra recorded with and without the slate (light blue and dark blue mass spectra) so the probability of a metastable reaching the limit of the case, then undergoing ionization on the surface and returning back to the region penetrated by the attractive SEM potential is unrealistic. This experiment demonstrates that the new deflection unit leads to mass spectra as if the old unit was installed without the faraday cup, which supports the claim that this metal surface plays a major role in the shift of the baseline. The new unit remains useful however, despite the similarities in the mass spectra, due to the ease with which the part can be customized in the future. The old unit is very sturdy while the new one provides space for a potential deflection plate and the slate can be remodeled into a faraday cup without influencing the baseline at all.

To compare the maximum signal intensity achievable with both units the new unit needs to be compared to the original unit while the deflection voltage is applied, as shown in figure 3.44. With the original unit the most prominent signal (m/z40) is cut off at the peak due to detector saturation and in general many hydrocarbon signals are visible, which cover up the peak for Ar_2^+. The difference in peak heights for the argon signals is almost two orders of magnitude. The peak height is not the only parameter to compare however, as it is apparent that the mass spectrum achieved with the new unit is much less congested and the mass peaks are narrower. Taking these data into account, the quality of the mass spectrum was not reduced by the new unit other than peak height, which can possibly be alleviated by incorporating a deflection plate into the new design.
Considering all simulation and experimental results the proposed mechanism of resonant ionization remains the most probable reason for the baseline shift. The fact that the new unit behaves exactly as predicted, further supports this mechanism.

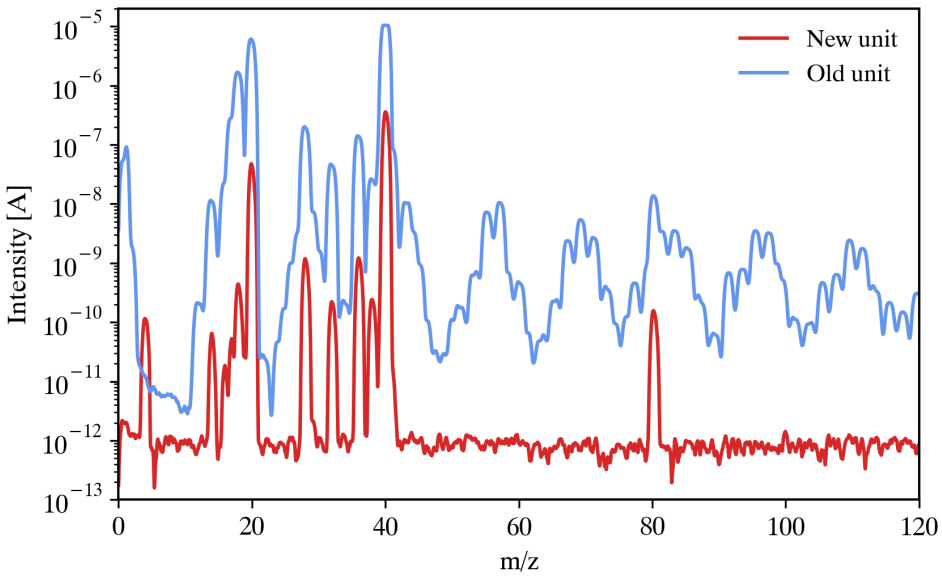

Figure 3.44: Comparison of the original deflection unit to the new deflection unit when the deflection voltage is applied in the old unit.

4 Summary, Conclusion and Outlook

The aim of this work was to solve a rampant problem of single stage quadrupole instruments operated with a high-pressure EI source regarding the baseline and in turn limit of detection and sensitivity. As the inlet pressure of the EI source is increased to values in the range of a few Pa, the baseline displays a steep rise of several orders of magnitude. This phenomenon occurs, to varying degrees, for several gases (helium, hydrogen, nitrogen, argon) regardless of most parameter settings of the mass spectrometer. As the level of the baseline rises and the level of signals stays the same, the signal to noise ratio is severely reduced. Additionally, small signals can be completely covered up by the baseline and the entire information of this peak is lost.

In the first part several hypotheses were proposed to explain the elevation of the baseline. These hypotheses included ion breakthrough, photons reaching the detector and a limited dynamic range of the pre-amplifier. Ion breakthrough involves ions traversing the QMF unfiltered due to space charge effects, which take over as the ion current in the rod system is increased to high values. This would lead to a constant baseline since ions reach the detector at every m/z value unfiltered. This proposal was disregarded, since the baseline remains on a constant level throughout the entire mass scan and does not show any decline as the applied quadrupolar potentials increase over the course of a scan. At higher potentials unstable m/z should be filtered out more effectively and subsequently the baseline should decline. More evidence against this hypothesis was achieved by blocking ions within the ion source by increasing the potential on the electrodes downstream of the ionization area but upstream the quadrupole. This did not cause any influence on the baseline and thus ion breakthrough was ruled out as a possible cause for the shift.
Photons can induce a current on the detector via the photoelectric effect and they are not affected by applied potentials. There are several possible

sources for photons of varying energy within the device but all of them could be experimentally or theoretically ruled out as cause for the baseline shift. Photons stemming from the filament do not have sufficient energy to overcome the work function of the detector material. Recombination reactions within the ion source can produce photons of sufficient energy but the number of photons generated via this route is way too small to realistically cause a current of the level of the baseline, as was the result of molflow simulations, mostly due to unfavorable trajectories from the ionization source to the deflection unit. Bremsstrahlung can be produced inside of the QMF as a byproduct of a filtered out ions. The energy of these photons is naturally high enough to overcome the work function and thus potentially cause a baseline shift. However when the rod system was set to ground potential during the scan (instead of the specified RF and DC potentials it is normally operated with), the baseline exhibited the same increased level as under normal conditions. In this setup no ions are filtered out in the mass analyzer so no bremsstrahlung is present and thus such photons cannot be the main reason of the issue. Additional experiments were done with an LiF window in front of the SEM conversion dynode and in downstream of the ion source. In these experiments the baseline remains at the level of the electronic noise floor even when photons of >104nm are able to traverse the material.
It is technically possible that the pre-amplifier is designed to actively keep both the highest peak and the baseline within its dynamic range. This can be achieved by adapting the baseline to accommodate for high peaks close to detector saturation. However the intensity of the highest peak is unknown at the beginning of a scan but the baseline is already at the elevated level from the very start of the scan. Additionally, the device does not change the level of the baseline on a scan to scan basis as the intensity of the highest peak decreases or increases and even in an empty mass spectrum the baseline is elevated and thus the pre-amplifier does not play a role in the mechanism behind the increase of the baseline.

As hypotheses were ruled out new ones had to be proposed. For the next part of the work the main focus points were excited species and secondary ions. Excited neutral species are produced in the ion source as a byproduct of the ionization mechanism in large quantities, depending on the operating

conditions. They naturally traverse the rod system unfiltered but they can undergo surface reactions on the detector surfaces, induce a signal and thus appear in the mass spectrum on every m/z value. Secondary ions formed downstream of the rod system by either gas phase reactions, photoionization or surface reactions will be detected as a regular primary ion coming from the EI source.

Excited species are theoretically abundant enough to be the main cause for the baseline shift, as calculated by the excitation cross section and its relation to the ionization cross section. The corresponding states have to be metastable in nature, however, due to the extended distance between the ionization source and the exit of the rod system. Experimental results exhibited a significant variance of the baseline depending on the potential applied to the deflection electrode, using both, the faraday cup and the SEM as detectors. At higher potentials, regardless of polarity, the baseline decreases by two orders of magnitude but it never reaches the level of the electronic noise floor. This demonstrates that the main cause is ionic in nature but there is a secondary underlying mechanism which must come from neutrals. As a result the mechanism of surface reactions occuring directly on the surface of the detector can also not be the main cause but it could very well be a secondary mechanism. This experiment also puts secondary ions into the spotlight since no other mechanism can explain the ionic nature of the particles leading to the baseline shift.

The mechanism of the formation of secondary ions was the main focus of the next part of this work. As already discussed there are three possible mechanisms: Photoionization, gas phase reactions and surface reactions.
Bremsstrahlung was already proven to play no role in the mechanism, which only leaves thermal photons from the filament and photons produced in recombination reactions to ionize a particle downstream of the rod system, inside of the deflection unit. Photons generated via black body radiation by the filament cannot ionize a neutral particle due to the high ionization threshold so such photons have to interact with excited species to possibly lead to the formation of ions. This interaction is highly improbable since the particle density of metastable species within the deflection unit is very low and the

probability for a photon to travel all the way into the deflection unit is miniscule as well. Sufficiently energetic photons created in recombination reactions can carry abundant energy to ionize even a neutral particle. However the amount of photons that stem from the ionization source and reach the deflection unit is still diminutive.
Gas phase reactions can only lead to an ion if the participating particles are both in an excited state. The argument of low particle density within the deflection unit applies even more so, especially considering the density of excited particles, which is orders of magnitude lower as compared to neutral background particles. Calculations showed that the most probable amount of collisions experienced by a metastable argon atom within the deflection unit is 8.5×10^{-8} so this mechanism is, again, highly improbable.
Surface reactions can produce an ion if the impacting particle is in an excited state close to the ionization threshold. An electron is transmitted from the excited state to the metal lattice, leaving behind a cation. This mechanism can occur on any surface within the deflection unit but every metastable present in this compartment is bound to collide with a surface eventually. This mechanism competes with Auger neutralization and Auger de-excitation. The latter mechanisms lead to the ejection of an electron from the metal lattice and produce a neutral particle. The ejected electron ultimately leads to an electric current amplified by the electronics of the faraday cup detector unit and subsequently to a peak in a mass spectrum. Experiments demonstrated that the presence of a surface within the deflection unit is mandatory for the baseline shift to occur. A metal plate replacing the faraday cup leads to a baseline shift of the same magnitude, while the absence of a surface perpendicular to the axis of the quadrupole reduces the baseline to almost the electronic noise floor.

The baseline shift when using the faraday cup can be explained at least partially by the ejection of electrons from the surface, however the mechanism for the effect of the deflection voltage on the baseline shift remains unclear. SIMION simulations of the deflection unit were performed to investigate the effect of ions and electrons in this area. The simulations showed that a significant amount of ions reach the faraday cup at deflection voltages >50 V while electrons take over at lower potentials. The experimental results showed the same behavior of the baseline shift, a plateau at potentials of >75 V and a

steep decline at lower values. Experiments and simulations are thus in very good agreement.
The situation when using the SEM as detector is different since the influence of the deflection voltage is of contrary nature. The simulations give the same picture compared to the experiments, it thus can be stated that the baseline shift is likely caused by ions created within the deflection unit. The simulation shows that the influence of the attractive field of the conversion dynode on the ions becomes significant only at low deflection plate potentials. As the deflection voltage is increased the ions are either pushed towards the faraday cup or drawn to the deflection plate since the conversion dynode of the SEM is much further away from the location of the ionization. Simulation and experiment are in good agreement in this case as well. The mechanism of resonant ionization thus seems to be the main cause for the baseline shift for the SEM as detector.

In future works the proposed secondary cause for the baseline shift, which was shown to be of non-ionic nature but still stems from the ion source, should be investigated. Possible causes disregarded in this work, photons and gas-phase reactions, for being too unlikely may still be the origin for a fraction of this shift since its amplitude is so low. More thorough investigations with materials being transparent at certain wavelengths might give further insight into the source for the photons and their interactions with the detector. Altering pressure ranges in the device (and thus likelihoods for reactions to occur), downstream of the ion source could clarify the role of gas-phase reactions to contribute to the baseline shift.

The new deflection unit still lacks two essential parts: A deflection plate and a faraday cup. Incorporating both should be possible without too much effort. The slate basically functions as a faraday detector already, defined by its positioning axially to the QMF, in addition to the needed electronic parts to pick-up the signal. It may be needed to give the slate a shape that resembles a cup but despite that the slate can functionally be a faraday detector. A deflection plate should be placed perpendicularly to the ion beam to ensure that no resonant ionization can take place on this surface. A favorable position for this electrode would be on the opposite side of the SEM. A positive potential on this surface would act as an auxiliary potential to guide ions towards the

SEM, in addition to the electric field established by the conversion dynode itself. It might be possible to find a different positon, e.g., below the cavity for the SEM, but the space is very limited and the opposite side seems to be the most promising place for a deflection plate.
If the general design of the deflection unit is to be changed, the inner radius of the cylinder could be reduced in order to increase the effect of the electric field of the SEM. The faraday detector would need to be moved closer to the end of the rod system, to reduce loss of ions on the outer encasing in the field free zone between the rods and the detector. The cavity for the SEM could potentially be bigger to direct more ions onto a trajectory towards the conversion dynode.

In order to further examine the mechanism of resonant ionization a surface oriented perpendicularly to the neutral beam could be manufactured from different materials with a wide range of work functions. This way it could be evaluated if there is a sharp cut-off at some point when the mechanismis energetically prohibited.

Bibliography

[1] W. Paul and H. Steinwedel. "Ein neues Massenspektrometer ohne Magnetfeld". In: *Zeitschrift für Naturforsch.* 8a (1953), pp. 448–450.

[2] E. D. Courant, M. S. Livingston, and H. S. Snyder. "The Strong-Focusing Synchroton-A New High Energy Accelerator". In: *Phys. Rev.* 88.5 (1952), pp. 1190–1196. DOI: 10.1103/PhysRev.88.1190.

[3] K. A. Nier, A. L. Yergey, and J. P. Gale. "Historical Perspectives Part A: The Development of Mass Spectrometry". In: *Encycl. Mass Spectrom.* 9th ed. 2016. ISBN: 978-0-08-043848-1.

[4] P. H. Dawson. *Quadrupole Mass Spectrometry and its applications.* Amsterdam: Elsevier Scientific Publishing Company, 1976. ISBN: 0444413456.

[5] W. M. Brubaker. *Auxiliary Electrodes for Quadrupole Mass Filters.* 1964.

[6] V. D. Berkout and V. M. Doroshenko. "Improving the quality of the ion beam exiting a quadrupole ion guide". In: *J. Am. Soc. Mass Spectrom.* 17.3 (2006), pp. 335–340. DOI: 10.1016/j.jasms.2005.12.002.

[7] W. L. Fite. "Spatial separation of fringe fields in quadrupole mass filters". In: *Rev. Sci. Instrum.* 47.3 (1976), pp. 326–330. DOI: 10.1063/1.1134616.

[8] W. Paul, H. P. Reinhard, and U. von Zahn. "Das elektrische Massenfilter als Massenspektrometer und Isotopentrenner". In: *Zeitschrift für Phys.* 152.2 (1958), pp. 143–182. DOI: 10.1007/BF01327353.

[9] R. E. Reinsfelder and M. B. Denton. "Theory and characterization of a separator analyzer mass spectrometer". In: *Int. J. Mass Spectrom. Ion Phys.* 37.2 (1981), pp. 241–250. DOI: 10.1016/0020-7381(81)80012-5.

[10] M. L. Vestal and J. H. Futrell. "Photodissociation of CH3Cl+ and CH3Br+ in a tandem mass spectrometer". In: *Chem. Phys. Lett.* 28.4 (1974), pp. 1974–1976.

[11] R. A. Yost and C. G. Enke. "Selected Ion Fragmentation with a Tandem Quadrupole Mass Spectrometer". In: *J. Am. Chem. Soc.* 100.7 (1978), pp. 2274–2275. DOI: 0002-7863/78/1500-2274S01.00/0.

[12] R. A. Yost et al. "High efficiency collision-induced dissociation in an RF-only quadrupole". In: *Int. J. Mass Spectrom. Ion Phys.* 30.2 (1979), pp. 127–136. DOI: 10.1016/0020-7381(79)80090-X.

[13] P. H. Dawson and J. E. Fulford. “The effective containment of parent ions and daughter ions in triple quadrupoles used for collisional dissociation”. In: *Int. J. Mass Spectrom. Ion Phys.* 42.3 (1982), pp. 195–211. DOI: 10.1016/0020-7381(82)80065-X.

[14] J. H. Beynon et al. “Design of a mass and ion kinetic energy spectrometer for organic chemical work”. In: *Org. Mass Spectrom.* 17.2 (1982), pp. 55–66. ISSN: 10969888. DOI: 10.1002/oms.1210170202.

[15] U. P. Schlunegger, M. Stoeckli, and R. M. Caprioli. “Frequency scan for the analysis of high mass ions generated by matrix-assisted laser desorption/ionization in a Paul trap”. In: *Rapid Commun. Mass Spectrom.* 13.18 (1999), pp. 1792–1796. ISSN: 09514198. DOI: 10.1002/(SICI)1097-0231(19990930)13:18<1792::AID-RCM715>3.0.CO;2-S.

[16] B. Landais et al. “Varying the radio frequency: A new scanning mode for quadrupole analyzers”. In: *Rapid Commun. Mass Spectrom.* 12.6 (1998), pp. 302–306. ISSN: 09514198. DOI: 10.1002/(SICI)1097-0231(19980331)12:6<302::AID-RCM154>3.0.CO;2-U.

[17] E. T. Whittaker. “On the general solution of mathieu’s equation”. In: *Proc. Edinburgh Math. Soc.* 32 (1913), pp. 75–80. ISSN: 14643839. DOI: 10.1017/S0013091500035069.

[18] F. G. Major, V. N. Gheorghe, and G. Werth. *Charged particle traps: Physics and techniques of charged particle field confinement.* Berlin, 2005. DOI: 10.1007/978-1-0716-0480-9_5.

[19] K. Cheung, L. F. Velásquez-García, and A. I. Akinwande. “Fully batch-fabricated linear quadrupole mass filters”. In: *Tech. Dig. - Solid-State Sensors, Actuators, Microsystems Work.* (2008), pp. 316–319. DOI: 10.31438/trf.hh2008.82.

[20] S. U. Syed et al. “Quadrupole mass filter: Design and performance for operation in stability zone 3”. In: *J. Am. Soc. Mass Spectrom.* 24.10 (2013), pp. 1493–1500. ISSN: 10440305. DOI: 10.1007/s13361-013-0704-z.

[21] S. U. Syed et al. “Factors influencing the QMF resolution for operation in stability zones 1 and 3”. In: *J. Am. Soc. Mass Spectrom.* 23.5 (2012), pp. 988–995. ISSN: 10440305. DOI: 10.1007/s13361-012-0348-4.

[22] L. F. Velásquez-García, K. Cheung, and A. I. Akinwande. “An application of 3-D MEMS packaging: Out-of-plane quadrupole mass filters”. In: *J. Microelectromechanical Syst.* 17.6 (2008), pp. 1430–1438. ISSN: 10577157. DOI: 10.1109/JMEMS.2008.2006769.

[23] Z. Du, D. J. Douglas, and N. V. Konenkov. "Elemental analysis with quadrupole mass filters operated in higher stability regions". In: *J. Anal. At. Spectrom.* 14.8 (1999), pp. 1111–1119. ISSN: 02679477. DOI: 10.1039/a804022b.

[24] D. J. Douglas. "Linear Quadrupoles In Mass Spectrometry". In: *Mass Spectrom. Rev.* 28.6 (2009), pp. 937–960. ISSN: 00195189. DOI: 10.1002/mas. arXiv: NIHMS150003.

[25] M. Sudakov et al. "Possibility of operating quadrupole mass filter at high resolution". In: *Int. J. Mass Spectrom.* 408 (2016), pp. 9–19. ISSN: 13873806. DOI: 10.1016/j.ijms.2016.09.003.

[26] S. Medhe. "Mass Spectrometry: Detectors Review". In: *Chem. Biomol. Eng.* 3.4 (2018), p. 51. ISSN: 2578-8884. DOI: 10.11648/j.cbe.20180304.11.

[27] J. Hölzl and F. K. Schulte. *Work function of metals*. 1979, pp. 1–150. DOI: 10.1007/bfb0048919.

[28] J. H. Gross. *Massenspektrometrie - Ein Lehrbuch*. Springer Spektrum, 2011. ISBN: 9788490225370.

[29] L. A. Dietz. "Basic properties of electron multiplier ion detection and pulse counting methods in mass spectrometry". In: *Rev. Sci. Instrum.* 36.12 (1965), pp. 1763–1770. ISSN: 00346748. DOI: 10.1063/1.1719460.

[30] M. van Gorkom and R. Glick. "Electron Multiplier Response under Positive Ion Impact I) Secondary Electron Coefficients". In: *Int. J. Mass Spectrom. Ion Phys.* 4 (1970), pp. 203–218. DOI: 10.1016/0020-7381(70)85038-0.

[31] J. Griffiths. "A brief history of mass spectrometry". In: *Anal. Chem.* 80 (2008), pp. 5678–5683. DOI: 10.1002/9781119377368.ch2.

[32] F. Gelebart, R. J. Tweed, and J. Peresse. "Autoionization by electron impact: Experiment with He". In: *J. Phys. B At. Mol. Phys.* 9.10 (1976), pp. 1739–1748. ISSN: 00223700. DOI: 10.1088/0022-3700/9/10/018.

[33] N. E. Small-Warren and L. Y. C. Chiu. "Lifetime of the metastable 3P2 and 3P0 states of rare-gas atoms". In: *Phys. Rev. A* 11.6 (1975), pp. 1777–1783. ISSN: 10502947. DOI: 10.1103/PhysRevA.11.1777.

[34] T. Tate, John and P. T. Smith. "Ehe Efficiencies of Ionization and Ionization Potentials of Various Gases under Electron Impact". In: *Phys. Rev.* 39 (1932), pp. 270–277.

[35] R. Buchdahl. "Negative Ion Formation in Iodine Vapor by Electron Impacts". In: *J. Chem. Phys.* 9.2 (1941), pp. 146–152. ISSN: 00219606. DOI: 10.1063/1.1750866.

[36] W. T. Hwang, Y.-K. Kim, and M. E. Rudd. "New model for electron-impact ionization cross sections of molecules". In: *J. Chem. Phys.* 104.8 (1996), pp. 2956–2966. ISSN: 00219606. DOI: 10.1063/1.471116.

[37] H. Tawara and T. Kato. "Total and partial ionization Cross Sections of Atoms and Ions by Electron Impact". In: *At. Data Nucl. Data Tables* 36 (1987), pp. 167–353.

[38] Y.-K. Kim et al. *Electron-Impact Cross Sections for Ionization and Excitation Database.* DOI: https://dx.doi.org/10.18434/T4KK5C. URL: https://physics.nist.gov/PhysRefData/Ionization/molTable.html.

[39] C. J. Davisson. "The Discovery of Electron Waves". In: *Bell Syst. Tech. J.* 17.3 (1938), pp. 475–482. ISSN: 15387305. DOI: 10.1002/j.1538-7305.1938.tb00792.x.

[40] F. H. Allen et al. "Tables of bond lengths determined by x-ray and neutron diffraction. Part 1. Bond lengths in organic compounds". In: *J. Chem. Soc. Perkin Trans. 2* 12 (1987), pp. 1–19. ISSN: 1472779X. DOI: 10.1039/P298700000S1.

[41] H. Bhutadia, A. Chaudhari, and M. Vinodkumar. "Electron impact ionisation cross sections for atomic and molecular allotropes of phosphorous and arsenic". In: *Mol. Phys.* 113.23 (2015), pp. 3654–3662. ISSN: 13623028. DOI: 10.1080/00268976.2015.1050472.

[42] J. B. Mann. *Atomic Structure Calculations II. Hartree-Fock Wavefunctions and Radial Expectation Values: Hydrogen to Lawrencium.* Tech. rep. 1968.

[43] B. F. W. Lampe and J. L. Franklin. "Cross Sections for Ionization by Electrons". In: 2 (1957), pp. 3–6.

[44] H. Nishimura and H. Tawara. "Total electron impact ionization cross sections for simple hydrocarbon molecules". In: *J. Phys. B At. Mol. Opt. Phys.* 27.10 (1994), pp. 2063–2074. ISSN: 13616455. DOI: 10.1088/0953-4075/27/10/016.

[45] R. S. Schappe et al. "Measurements of cross sections for electron-impact excitation into the metastable levels of argon and number densities of metastable argon atoms". In: *Phys. Rev. A* 50.1 (1994), pp. 444–461. ISSN: 10502947. DOI: 10.1103/PhysRevA.50.444.

[46] M Hayashi. *Bibliography of Electron and photon Cross Sections with Atoms and Molecules.* Tech. rep. 2003.

[47] F. M. Kannenstine. "Formation and Life of Metastable Helium". In: *Astrophys. J.* 55 (1922), p. 345. ISSN: 0004-637X. DOI: 10.1086/142672.

[48] V. A. Ankudinov, S. V. Bobashev, and E. P. Andreev. "Measurement of lifetimes of excited states of the hydrogen atom". In: *J. Exp. Theor. Phys.* 21.1 (1965), pp. 26–32.

[49] S Heron, R. W. P. Mcwhirter, and E. H. Rhoderick. "Measurements of lifetimes of excited states of helium atoms". In: *Proc. R. Soc. London. Ser. A. Math. Phys. Sci.* 234.1199 (1956), pp. 565–583. ISSN: 0080-4630. DOI: 10.1098/rspa.1956.0058.

[50] M. B. Das and S. Karmakar. “Radiative lifetimes of some excited states of neutral xenon”. In: *Eur. Phys. J. D* 32.3 (2005), pp. 285–288. ISSN: 14346060. DOI: 10.1140/epjd/e2005-00002-4.

[51] K. V. Wood, A. H. Grange, and J. W. Taylor. “Mass Discrimination Effects in a Quadrupole Mass Spectrometer”. In: *Anal. Chem.* 50.12 (1978), pp. 1652–1654. ISSN: 15206882. DOI: 10.1021/ac50034a021.

[52] R. Edward. “The Development of New Quadrupolar Mass-Spectrometric Techniques and their Application to Cchemical Analysis”. PhD thesis. 2016.

[53] O. J. Orient, A. Chutjian, and V. Garkanian. “Miniature, high-resolution, quadrupole mass-spectrometer array”. In: *Rev. Sci. Instrum.* 68.3 (1997), pp. 1393–1397. ISSN: 00346748. DOI: 10.1063/1.1147947.

[54] F. Nakao and T. Yamamoto. “Off-Axially Arranged, Low Noise, High Collection Efficiency Ion Collector for Quadrupole Mass Spectrometer”. In: *Rev. Sci. Instruments* 23.3 (1975).

[55] K. Feser and W. Kögler. “The quadrupole mass filter for GC/MS applications”. In: *J. Chromatogr. Sci.* 17.2 (1979), pp. 57–63. ISSN: 1945239X. DOI: 10.1093/chromsci/17.2.57.

[56] R. C. Lao, R. Sander, and R. F. Pottie. “Discrimination in electron multipliers for atomic ions 1. Multiplier yields for 24 mass-analyzed ions”. In: *Int. J. Mass Spectrom. Ion Phys.* 10 (1972).

[57] R. F. Pottie, D. L. Cocke, and K. A. Gingerich. “Discrimination in electron multipliers for atomic ions 2. Comparison of yields for 61 atoms”. In: *Int. J. Mass Spectrom. Ion Phys.* 11 (1973), pp. 41–48.

[58] C. Weissmantel et al. *Kleine Enzyklopädie: Struktur der Materie.* 1st ed. Leipzig, 1982.

[59] W. R. MacGillivray and M. C. Standage. “Stepwise electron and laser excitation of atoms”. In: *Phys. Rep.* 168.1 (1988), pp. 1–54. ISSN: 03701573. DOI: 10.1016/0370-1573(88)90113-5.

[60] O. Tommasi et al. “A High-density Collimated Metastable He Beam With Population Inversion”. In: *J. Phys. D. Appl. Phys.* 25.10 (1992), pp. 1408–1417. ISSN: 13616463. DOI: 10.1088/0022-3727/25/10/005.

[61] B. Donnally et al. “Metastable Hydrogen Atoms Produced in Charge Exchange”. In: *Phys. Rev. Lett.* 12.18 (1964), pp. 502–503.

[62] W. E. Lamb and R. C. Retherford. “Fine structure of the hydrogen atom. Part I”. In: *Phys. Rev.* 79.4 (1950), pp. 549–572. ISSN: 0031899X. DOI: 10.1103/PhysRev.79.549.

[63] M. Bartsch, G. F. Hanne, and J. Kessler. “Asymmetric scattering of polarized electrons from atoms with closed and open shells”. In: *J. Phys. B At. Mol. Opt. Phys.* 25.7 (1992), pp. 1511–1526. ISSN: 13616455. DOI: 10.1088/0953-4075/25/7/021.

[64] H. Hotop and A. Niehaus. “Reactions of excited atoms and molecules with atoms and molecules”. In: *Zeitschrift für Phys.* 215.4 (1968), pp. 395–407. ISSN: 1434-6001. DOI: 10.1007/bf01380020.

[65] V. G. Anicich. *An index of the literature for bimolecular gas phase cation-molecule reaction kinetics*. Tech. rep. November. 2003, p. 1194. URL: http://hdl.handle.net/2014/7981.

[66] R. F. Stebbings and P. R. S. L. A. “Gaseous and surface reactions involving helium metastable atoms and resonance photons”. In: *Proc. R. Soc. London. Ser. A. Math. Phys. Sci.* 241.1225 (1957), pp. 270–282. ISSN: 0080-4630. DOI: 10.1098/rspa.1957.0127.

[67] P. W. Atkins and J. de Paula. *Physikalische Chemie*. 4th ed. 2006.

[68] P. W. Atkins. *Physical Chemistry*. 1986.

[69] J. Shapiro and G. Breit. “Metastability of 2s states of hydrogenic atoms”. In: *Phys. Rev.* 113.1 (1959), pp. 179–181. ISSN: 0031899X. DOI: 10.1103/PhysRev.113.179.

[70] M. Bixon and J. Jortner. “Intramolecular Radiationless Transitions”. In: *J. Chem. Phys.* 48.2 (1968), p. 715. ISSN: 00219606. DOI: 10.1063/1.1668703.

[71] A. V. Phelps and J. P. Molnar. “Lifetimes of metastable states of noble gases”. In: *Phys. Rev.* 89.6 (1953), pp. 1202–1208. ISSN: 0031899X. DOI: 10.1103/PhysRev.89.1202.

[72] A. Einstein. “Über einen die Erzeugung und Verwandlung des Lichtes betreffenden heuristischen Gesichtspunkt”. In: *Ann. Phys.* 322.6 (1905), pp. 132–148. ISSN: 15213889. DOI: 10.1002/andp.19053220607. URL: http://doi.wiley.com/10.1002/andp.19053220607.

[73] K. T. Compton and O. Richardson. “XLV. The photoelectric effect II”. In: *London, Edinburgh, Dublin Philos. Mag. J. Sci.* 26.154 (1913), pp. 549–567. ISSN: 1941-5982. DOI: 10.1080/14786441308635002.

[74] P. Agostini and G. Petite. “Photoelectric effect under strong irradiation”. In: *Contemp. Phys.* 29.1 (1988), pp. 57–77. ISSN: 0010-7514. DOI: 10.1080/00107518808213751.

[75] R. A. Powell. “Photoelectric effect: Back to basics”. In: *Am. J. Phys.* 46.10 (1978), pp. 1046–1051. ISSN: 0002-9505. DOI: 10.1119/1.11493.

[76] R. E. Simon and B. F. Williams. “Secondary-electron emission”. In: *IEEE Trans. Nucl. Sci.* 15.3 (1968), pp. 167–170. ISSN: 15581578. DOI: 10.1109/TNS.1968.4324934.

[77] H. Bruining. “The depth at which secondary electrons are liberated”. In: *Physica* 3.9 (1936), pp. 1046–1052. ISSN: 00318914. DOI: 10.1016/s0031-8914(36)80330-9.

[78] H. Winter. “What ions experience on their way into a metal surface”. In: *Zeitschrift für Phys. D Atoms, Mol. Clust.* 21.1 Supplement (1991), pp. 129–133. ISSN: 01787683. DOI: 10.1007/BF01426264.

[79] D. Hasselkamp et al. “Ion Induced Electron Emission from Metal Surfaces”. In: *Nucl. Instruments Methods* 180 (1981), pp. 349–356.

[80] Z. B. Wang et al. “Determination of the de-excitation probability of argon metastable (1s5 and 1s3) atoms on aluminum, stainless steel, silicon, quartz and Pyrex surfaces”. In: *J. Phys. D. Appl. Phys.* 48.10 (2015), p. 105203. ISSN: 13616463. DOI: 10.1088/0022-3727/48/10/105203. URL: http://dx.doi.org/10.1088/0022-3727/48/10/105203.

[81] H Conrad et al. “Deexcitation Mechanisms in Metastable He-Surface Collisions”. In: *Surf. Sci.* 100 (1980), pp. 461–466.

[82] W. Sesselmann et al. “Interaction of metastable noble-gas atoms with transition-metal surfaces: Resonance ionization and Auger neutralization”. In: *Phys. Rev. B* 35.4 (1987), pp. 1547–1559. ISSN: 01631829. DOI: 10.1103/PhysRevB.35.1547.

[83] Y. Harada, S. Masuda, and H. Ozaki. “Electron Spectroscopy Using Metastable Atoms as Probes for Solid Surfaces”. In: *Chem. Rev.* 2665.94 (1997), pp. 1897–1952.

[84] H. D. Hagstrum. “Reflection of noble gas ions at solid surfaces”. In: *Phys. Rev.* 123.3 (1961), pp. 758–765. ISSN: 0031899X. DOI: 10.1103/PhysRev.123.758.

[85] D. Manura and D. Dahl. *SIMION Version 8.0 User Manual.* 4th revise. 2008.

[86] R. Ierusalimschy. *Programming in Lua.* 4th ed. Rio de Janeiro, 2016. URL: Lua.org.

[87] *SPARTA Direct Simulation Monte Carlo (DSMC) Simulator.* URL: https://sparta.github.io/.

[88] M. A. Gallis et al. “Direct simulation Monte Carlo: The quest for speed”. In: *Proc. 29th Rarefied Gas Dyn. Symp.* 2014. ISBN: 9780735412651. DOI: 10.1063/1.4902571.

[89] G. A. Bird. “Approach to translational equilibrium in a rigid sphere gas”. In: *Phys. Fluids* 6.10 (1963), pp. 1518–1519. ISSN: 10706631. DOI: 10.1063/1.1710976.

[90] G. A. Bird. “Definition of mean free path for real gases”. In: *Phys. Fluids* 26.11 (1983), pp. 3222–3223. ISSN: 10706631. DOI: 10.1063/1.864095.

[91] K. Koura and H. Matsumoto. “Variable soft sphere molecular model for inverse-power-law or Lennard-Jones potential”. In: *Phys. Fluids A* 3.10 (1991), pp. 2459–2465. ISSN: 08998213. DOI: 10.1063/1.858184.

[92] M. Ady and R. Kersevan. “Recent developments of Monte-Carlo codes MolFlow+ and SynRad+”. In: *10th Int. Part. Accel. Conf., Melbourne, Aust.* 2019.

[93] D. R. Bates, A. E. Kingston, and R. W. P. Mcwhirter. “Recombination between electrons and atomic ions, I. Optically thin plasmas”. In: *Proc. R. Soc. London. Ser. A. Math. Phys. Sci.* 267.1330 (1962), pp. 297–312. ISSN: 0080-4630. DOI: 10.1098/rspa.1962.0101.

[94] L. Minnhagen. “Spectrum and the energy levels of neutral argon”. In: *J. Opt. Soc. Am.* 63.10 (1973).

[95] G. Herzberg. “On the Electronic Structure of the Nitrogen Molecule”. In: *Phys. Rev.* 69.7 (1946), pp. 362–365.

[96] Boris M. Smirnov. “The Hydrogen Atom”. In: *Phys. Atoms Ions.* 2003, pp. 30–61. DOI: https://doi.org/10.1007/0-387-21730-4_2.

[97] R. D. Larrabee. “Spectral Emissivity of Tungsten”. In: *J. Opt. Soc. Am.* 49.6 (1958), pp. 619–625.

[98] Y. Hahn. “Electron-ion recombination processes-an overview”. In: *Reports Prog. Phys.* 60 (1997), pp. 691–759.

[99] J. E. Huheey. *Textbook Errors, 85 The Correct Sizes of the Noble Gas Atoms.* Tech. rep. 1968. URL: https://pubs.acs.org/sharingguidelines.